NAVAL POSTGRADUATE SCHOOL
Monterey, California

THESIS

TARGET DETECTION AND SCENE CLASSIFICATION WITH VNIR/SWIR SPECTRAL IMAGERY

by

David Robert Perry

September 2000

Thesis Advisor:	Richard C. Olsen
Second Reader:	Alan A. Ross

Approved for public release; distribution is unlimited.

DTIC QUALITY INSPECTED 4
20001211 115

REPORT DOCUMENTATION PAGE		Form Approved OMB No. 0704-0188

Public reporting burden for this collection of information is estimated to average 1 hour per response, including the time for reviewing instruction, searching existing data sources, gathering and maintaining the data needed, and completing and reviewing the collection of information. Send comments regarding this burden estimate or any other aspect of this collection of information, including suggestions for reducing this burden, to Washington headquarters Services, Directorate for Information Operations and Reports, 1215 Jefferson Davis Highway, Suite 1204, Arlington, VA 22202-4302, and to the Office of Management and Budget, Paperwork Reduction Project (0704-0188) Washington DC 20503.

1. AGENCY USE ONLY *(Leave blank)*	2. REPORT DATE September 2000	3. REPORT TYPE AND DATES COVERED Master's Thesis
TITLE AND SUBTITLE: Target Detection and Scene Classification with VNIR/SWIR Spectral Imagery		5. FUNDING NUMBERS
6. AUTHOR(S) David R. Perry		
7. PERFORMING ORGANIZATION NAME(S) AND ADDRESS(ES) Naval Postgraduate School Monterey, CA 93943-5000		8. PERFORMING ORGANIZATION REPORT NUMBER
9. SPONSORING / MONITORING AGENCY NAME(S) AND ADDRESS(ES) N/A		10. SPONSORING / MONITORING AGENCY REPORT NUMBER

11. SUPPLEMENTARY NOTES The views expressed in this thesis are those of the author and do not reflect the official policy or position of the Department of Defense or the U.S. Government.

12a. DISTRIBUTION / AVAILABILITY STATEMENT	12b. DISTRIBUTION CODE
Approved for public release; distribution is unlimited.	

ABSTRACT *(maximum 200 words)*

Spectral imagery provides a new resource in remote sensing, which can be used for defeating camouflage, concealment and detection, as well as terrain categorization. A new sensor, the Night Vision Imaging Spectrometer (NVIS), provides VNIR/SWIR (0.4-2.5 m) spectra, which are used to here to study such applications. NVIS has a nominal GSD of 0.5-1.5 meters in operational modes utilized for this work, which make the data well suited for studying mapping and classification algorithms. Data taken at Ft. A.P. Hill on April 29, 2000 are studied here.

A Principal Components Transformation was performed on the NVIS data. From this new data set, target spectra were collected for use in classification algorithms. The NVIS data was converted from radiance to reflectance in two different ways: Empirical Line Method and Internal Average Relative Reflectance. Using this data, various standard algorithms were performed. It was found that while none of the algorithms correctly classified all of the selected targets, the Mahalanobis Distance and Mixture Tuned Matched Filter™ algorithms were the most successful.

14. SUBJECT TERMS Hyperspectral, NVIS, Remote Sensing, Imagery, Electro-Optical Sensing			15. NUMBER OF PAGES 216
			16. PRICE CODE
17. SECURITY CLASSIFICATION OF REPORT Unclassified	18. SECURITY CLASSIFICATION OF THIS PAGE Unclassified	19. SECURITY CLASSIFICATION OF ABSTRACT Unclassified	20. LIMITATION OF ABSTRACT UL

NSN 7540-01-280-5500

Standard Form 298 (Rev. 2-89)
Prescribed by ANSI

Std. 239-18

THIS PAGE INTENTIONALLY LEFT BLANK

Approved for public release; distribution is unlimited.

TARGET DETECTION AND SCENE CLASSIFICATION WITH VNIR/SWIR SPECTRAL IMAGERY

David R. Perry
Lieutenant, United States Navy
B.S., Texas A&M University, 1993

Submitted in partial fulfillment of the
requirements for the degree of

MASTER OF SCIENCE IN SPACE SYSTEMS OPERATIONS

from the

NAVAL POSTGRADUATE SCHOOL
September 2000

Author: _____
David R. Perry

Approved by: _____
R. C. Olsen, Thesis Advisor

_____
Alan A. Ross, Second Reader

_____
Dr. Rudy Panholzer, Chairman
Space Systems Academic Group

THIS PAGE INTENTIONALLY LEFT BLANK

ABSTRACT

Spectral imagery provides a new resource in remote sensing, which can be used for defeating camouflage, concealment and detection, as well as terrain categorization. A new sensor, the Night Vision Imaging Spectrometer (NVIS), provides VNIR/SWIR (0.4-2.5 m) spectra, which are used to here to study such applications. NVIS has a nominal GSD of 0.5-1.5 meters in operational modes utilized for this work, which make the data well suited for studying mapping and classification algorithms. Data taken at Ft. A.P. Hill on April 29, 2000 are studied here.

A Principal Components Transformation was performed on the NVIS data. From this new data set, target spectra were collected for use in classification algorithms. The NVIS data was converted from radiance to reflectance in two different ways: Empirical Line Method and Internal Average Relative Reflectance. Using this data, various standard algorithms were performed. It was found that while none of the algorithms correctly classified all of the selected targets, the Mahalanobis Distance and Mixture Tuned Matched Filter™ algorithms were the most successful.

THIS PAGE INTENTIONALLY LEFT BLANK

TABLE OF CONTENTS

I. INTRODUCTION 1
II. HYPERSPECTRAL IMAGING THEORY 3
A. REMOTE SENSING 3
1. Background 3
2. Electromagnetic Spectrum 4
3. Generation and Emission of Electromagnetic Radiation 6
4. Interaction of Electromagnetic Waves With Matter 9
5. Detection of Electromagnetic Radiation 9
B. SOLID SURFACE SENSING IN THE VISIBLE AND NEAR INFRARED 10
1. Spectral Characteristics of the Source 11
2. Atmospheric Effects 12
3. Wave-Surface Interactions 17
4. Signature of Solid Surface Materials 18
C. SPECTRAL DETECTORS 20
1. Spectral Characteristics 20
2. Other Characteristics 21
III. NIGHT VISION IMAGING SPECTROMETER 25
A. SYSTEM DESIGN 26
B. OPTICAL/MECHANICAL DESIGN 27
C. FOCAL PLANE ARRAYS 28
D. CHARACTERIZATION MEASUREMENTS 29
1. Modulation Transfer Function (MTF) 30
2. Crosstrack Spectral Error 31
3. Spatial Co-Registration of Spectral Channels 33
4. Spectral Calibration and Spectral Purity 34
E. NVIS DATA CALIBRATION 36
IV. HYPERSPECTRAL DATA TOOLS 37
A. RADIANCE TO REFLECTANCE CONVERSION 37
1. Empirical Line Calibration 37
2. Empirical In-Scene Calibration Method 38
B. PRINCIPAL COMPONENT ANALYSIS 39
C. SUPERVISED CLASSIFICATION TECHNIQUES 44
1. Parallelepiped Classification 45
2. Maximum Likelihood Classification 47
3. Minimum Distance Classification 50
4. Mahalanobis Distance 51
5. Spectral Angle Mapper 51

6. Binary Encoding 53
7. Linear Spectral Unmixing 55
8. Matched Filtering and Mixture Tuned Matched Filtering™ 56
9. Spectral Feature Fitting™ 57
D. UNSUPERVISED CLASSIFICATION TECHNIQUES 57
1. K-means 57
2. ISODATA 58
V. SPECTRAL ANALYSIS 61
A. RADIANCE TO REFLECTANCE CONVERSION 61
B. SPECTRAL AND SPATIAL SUBSETTING 65
C. DATA SET TRAINING 66
D. SUPERVISED CLASSIFICATION ALGORITHMS 70
1. Spectral Angle Mapper 70
a. Empirical Line Method 70
b. Empirical In-Scene Calibration 71
2. Parallelepiped 72
3. Binary Encoding 73
4. Minimum Distance 74
5. Mahalanobis Distance 75
6. Maximum Likelihood 76
7. Linear Spectral Unmixing 76
8. Matched Filter 78
9. MTMF™ 78
10. Spectral Feature Fitting 79
E. UNSUPERVISED MAPPING ALGORITHMS 80
1. K-Means 81
2. ISODATA 81
F. SUMMARY 83
VI. CONCLUSION 85
APPENDIX A. NVIS LINE DRAWINGS 89
APPENDIX B. CLASSIFICATION IMAGES 91
LIST OF REFERENCES 157
INITIAL DISTRIBUTION LIST 161

ACKNOWLEDGEMENTS

The author would like to thank Chris Simi of the Army Night Vision Laboratory for his assistance in gathering the information about the NVIS sensor. Without his help this thesis would not have been possible. Also, much thanks go to Roberta Dixon, also of the Night Vision Laboratory without who's help the software calibration of the data wouldn't have been possible. Finally, the author would like to thank and give acknowledgement to his wife Donna for her patience and support.

THIS PAGE INTENTIONALLY LEFT BLANK

LIST OF FIGURES

Fig. 2.1 Electromagnetic Spectrum (From Sabins, 1978) 4
Fig. 2.2 Characteristics of Spectral Regions. (From Multispectral Users Guide, 1995) 5
Fig. 2.3 (a), (b) Spectral Emittance of Black Bodies of Various Temperatures (From Elachi, 1987) 7
Fig. 2.4 Illustration of the Mechanics of Remote Sensing (From Elachi, 1987) 10
Fig. 2.5 Sun Illumination Spectral Irradiance at the Earth's Surface (From Elachi, 1987) 11
Fig. 2.6 Atmospheric Effects Influencing the Measurement of Reflected Solar Energy (From Lillesand, 1994) 12
Fig. 2.7 Atmospheric Transmission for the Standard U.S. 1962 atmosphere computed by Lowtran code (Kneizys, 1983) for Sun at Zenith. Attenuation due to: (a) water bands, (b) water continuum, (c) CO_2, O_2, and other minor absorbers, (d) molecular scattering, (e) ozone absorption, and (f) total transmission (From Asrar, 1989) 15
Fig. 2.8 Spectral Signature Diagram of a Variety of Geologic Materials (From Elachi, 1987) . 19
Fig. 2.9 Classifications of Spectral Imagers (From Multispectral User's Guide, 1995) 21
Fig. 2.10 A Pushbroom Scanner (From Campbell, 1996) 22
Fig. 3.1 NVIS (From Simi, 2000) 25
Fig. 3.2 Aircraft Velocity and Altitude as a Function of Frame Rate and Ground Sample Distance (From Folkman, DeLong, 1996) 27
Fig. 3.3 NVIS MTF Characterization (From Simi, 2000) 31
Fig. 3.4 Spectral Shift Due to Smile on SWIR FPA (From Simi, 2000) 33
Fig. 3.5 Monochromatic Source Images Showing Spectral Band Purity. Each Pixel is 5.25 nm in Bandwidth (From Folkman, Gleichauf, 1996) 35
Fig. 4.1 Histogram Illustrating EISC Method 38
Fig. 4.2 Two-Band Histogram of Hyperspectral Data 39
Fig. 4.3 Illustration of a modified co-ordinate system in which the pixel vectors have uncorrelated components (From Richards, 1999) 40
Fig. 4.4 (a) Band One of sample PC Rotation 42
Fig. 4.4 (b) Band Three of sample PC Rotation 43
Fig. 4.4 (c) Band Six of sample PC Rotation 43
Fig. 4.4 (d) Band Nine of sample PC Rotation 44
Fig. 4.5 Parallelepiped Classifier in Two Dimensions. Points Bounded by Parallelepipeds are Classified as Belonging to the Respective Classes, Points *i*, *j* are Unclassified. (From Mather, 1999) 46
Fig. 4.6 Parallelepiped Classification of Correlated Data Showing Regions of Inseparability (From Richards, 1999) 47
Fig. 4.7 a. Illustration of Poor Classification for Patterns Lying Near the Tails of the Distribution Functions of all Spectral Classes; b Use of a threshold to Remove Poor Classification (From Richards, 1999) 50

Fig. 4.8 Illustration of Spectral Angle Between Reference and Test Spectra (From Kruse, 1993) 52
Fig. 5.1 Panel Ground Truth Reflectance 62
Fig 5.2 Panel Spectra from ROI's 63
Fig. 5.3 Empirical Line Method Coefficients 64
Fig. 5.4 Empirical In-Scene Calibration Coefficients 65
Fig. 5.5 Illustration of Using N-Dimensional Visualizer to Separate Spectral Classes 68
Fig. A.1 Layout of the SWIR Spectrometer (After Folkman, DeLong, 1996) 89
Fig. A.2 Layout of the VNIR Spectrometer (After Folkman, DeLong, 1996) 90
Fig. B.1 False Color Image of the Scene, Illustrating Targets of Interest 91
Fig. B.2 ELM SAM Mapping Output for 0.1 and 0.2 Radians 92
Fig. B.3 ELM SAM Mapping Output for 0.3 and 0.5 Radians 93
Fig. B.4 ELM SAM Rule Image for Red Panel 94
Fig. B.5 ELM SAM Rule Image for Target #1 95
Fig. B.6 ELM SAM Rule Image for Target #2 96
Fig. B.7 ELM SAM Rule Image for Target #3 97
Fig. B.8 ELM SAM Rule Image for Target #4 98
Fig. B.9 EISC SAM Mapping Output for 0.1 and 0.2 Radians 99
Fig. B.10 EISC SAM Mapping Output for 0.3 and 0.5 Radians 100
Fig. B.11 EISC SAM Rule Image for Target #1 101
Fig. B.12 ELM SAM Rule Image for Target #2 102
Fig. B.13 EISC SAM Rule Image for Target #3 103
Fig. B.14 EISC SAM Rule Image for Target #4 104
Fig. B.15 Parallelepiped Mapping Output for 1.5 and 2.0 Std Dev. 105
Fig. B.16 Parallelepiped Mapping Output for 3.0 and 4.0 Std Dev. 106
Fig. B.17 Parallelepiped Rule Image for Target #1 107
Fig. B.18 Parallelepiped Rule Image for Target #2 108
Fig. B.19 Parallelepiped Rule Image for Target #3 109
Fig. B.20 Parallelepiped Rule Image for Target #4 110
Fig. B.21 Binary Encoding Mapping Output for 50% and 90% Certainty 111
Fig. B.22 Binary Encoding Mapping Output for 95% and 99% Certainty 112
Fig. B.23 Binary Encoding Rule Image for Target #1 113
Fig. B.24 Binary Encoding Rule Image for Target #2 114
Fig. B.25 Binary Encoding Rule Image for Target #3 115
Fig. B.26 Binary Encoding Rule Image for Target #4 116
Fig. B.27 Minimum Distance Mapping Output for 0.2 and 0.5 DN 117
Fig. B.28 Minimum Distance Mapping Output for 1 DN and Full Scene Mapping 118
Fig. B.29 Minimum Distance Rule Image for Target #1 119
Fig. B.30 Minimum Distance Rule Image for Target #2 120
Fig. B.31 Minimum Distance Rule Image for Target #3 121
Fig. B.32 Minimum Distance Rule Image for Target #4 122
Fig. B.33 Mahalanobis Distance Mapping Output for 10 and 20 DN 123

Fig. B.34 Mahalanobis Distance Mapping Output for 25 and 50 DN 124
Fig. B.35 Mahalanobis Distance Rule Image for Target #1 125
Fig. B.36 Mahalanobis Distance Rule Image for Target #2 126
Fig. B.37 Mahalanobis Distance Rule Image for Target #3 127
Fig. B.38 Mahalanobis Distance Rule Image for Target #4 128
Fig. B.39 Maximum Likelihood Mapping Output for Full Image and 90% Certainty 129
Fig. B.40 Maximum Likelihood Mapping Output for 99% and 99.99% Certainty 130
Fig. B.41 Maximum Likelihood Rule Image for Target #1 131
Fig. B.42 Maximum Likelihood Rule Image for Target #2 132
Fig. B.43 Maximum Likelihood Rule Image for Target #3 133
Fig. B.44 Maximum Likelihood Rule Image for Target #4 134
Fig. B.45 Linear Spectral Unmixing Error Output 135
Fig. B.46 Linear Spectral Unmixing Rule Image for Target #1 136
Fig. B.47 Linear Spectral Unmixing Rule Image for Target #2 137
Fig. B.48 Linear Spectral Unmixing Rule Image for Target #3 138
Fig. B.49 Linear Spectral Unmixing Rule Image for Target #4 139
Fig. B.50 Matched Filter Rule Image for Target #1 140
Fig. B.51 Matched Filter Rule Image for Target #2 141
Fig. B.52 Matched Filter Rule Image for Target #3 142
Fig. B.53 Matched Filter Rule Image for Target #4 143
Fig. B.54 MTMF™ Rule Image for Target #1 144
Fig. B.55 MTMF™ Rule Image for Target #2 145
Fig. B.56 MTMF™ Rule Image for Target #3 146
Fig. B.57 MTMF™ Rule Image for Target #4 147
Fig. B.58 Spectral Feature Fitting Rule Image for Target #1 148
Fig. B.59 Spectral Feature Fitting Rule Image for Target #2 149
Fig. B.60 Spectral Feature Fitting Rule Image for Target #3 150
Fig. B.61 Spectral Feature Fitting Rule Image for Target #4 151
Fig. B.62 K Means Mapping Image for Five Endmembers 152
Fig. B.63 K Means Mapping Image for Ten Endmembers 152
Fig. B.64 K Means Mapping Image for Sixteen Endmembers 153
Fig. B.65 ISODATA Mapping Image for Five Endmembers 154
Fig. B.66 ISODATA Mapping Image for Ten Endmembers 154
Fig. B.67 ISODATA Mapping Image for Sixteen Endmembers 155

THIS PAGE INTENTIONALLY LEFT BLANK

LIST OF TABLES

Table 3.1. NVIS Sensor Specifications (From Simi, 2000) 29
Table 5.1 List of Training Classes 69
Table 5.2 Summary of Algorithm Results 83

THIS PAGE INTENTIONALLY LEFT BLANK

I. INTRODUCTION

Spectral imagery is a tool in remote sensing which offers new support for military operations. Potential applications include Terrain Categorization (TERCAT), finding threat vehicles, and defeating enemy camouflage, concealment and detection (CCD).

Traditional approaches to TERCAT use the multi-spectral (MSI) systems such as the LANDSAT systems, dating back to 1972 (Lillesand, 1994). Over the last decade, new hyper-spectral (HSI) systems have emerged which offer the promise of greater ability to distinguish surface materials, including soil types. In particular, HSI systems offer great promise in areas such as littoral warfare, addressing issues such as trafficability.

Spectral imagery can be used to distinguish manmade and natural materials. As camouflage sophistication increases, the need for more discriminatory detectors increases. HSI offers great promise in defeating CCD because it can exploit spectral differences between naturally occurring materials and manmade.

Because of the obvious advantages of HSI over other methods of remote sensing, there is much interest in developing HSI detectors for use by the Defense Department. This interest spurred the creation of the Night Vision Imaging Spectrometer (NVIS). This airborne, Very Near Infrared/Short Wave Infrared (VNIR/SWIR) system is operated by the US Army Night Vision Lab in order to study the exploitation of spectral imagery. This thesis will present an assessment of NVIS and its capability to provide support to military operations (SMO). This thesis intends to use data from the airborne NVIS sensor to determine its capability to:

- Find Threat Vehicles and defeat Camouflage, Concealment, and Deception (CCD) efforts
- Categorize Terrain Features (MHS:Interim Progress Report, 1995).

A variety of standard algorithms will be used to study these topics. The tool used here is the Environment for Visualizing Information (ENVI), a commercial product from Research Systems Incorporated (RSI).

Chapter II of this thesis will provide a description of remote sensing, HSI, and the theoretical basis for HSI. Chapter III will describe NVIS itself, providing background on its development and its construction and operation. The tools and algorithms for the classification of the data acquired by NVIS will be discussed in Chapter IV. Spectral analysis of the NVIS data will be performed in Chapter V. Summary of results and conclusions will be presented in Chapter VI.

II. HYPERSPECTRAL IMAGING THEORY

A. REMOTE SENSING

1. Background

Remote sensing is the science of obtaining information about something, be it an object or a scene, through analyzing data obtained by a device that is not in contact with the subject under investigation. (Lillesand, 1994) The information that the sensor collects from the subject is in the form of electromagnetic radiation. This radiation can be visible light emitted by the Sun and reflected to the sensor, thermal radiation emitted by the subject, or radiation emitted from the detector platform itself to illuminate and reflect back from the subject. Depending on the subject and the environment through which the detector is sensing, any region of the electromagnetic spectrum can be sensed to gather information.

Some information can be gathered about a subject by collecting information at a single wavelength, or integrated over a portion of the spectrum. An example would be scene brightness as measured in simple black and white photography. However, from the inception of color photography in the 1930s (Elachi, 1987), it was noted that more information could be derived about a subject if data are acquired at more than one wavelength simultaneously. Most early sensors worked in the VNIR portion of the spectrum, exploiting silicon technology, in particular the early LANDSAT sensors. Parallel efforts in the thermal IR emerged later, as with TIMS.

2. Electromagnetic Spectrum

The electromagnetic spectrum (figure 2.1) is divided into a number of spectral regions. The different regions can be used to varying degrees in the field of remote sensing, in that from the different regions one can deduce different things about what is being sensed. Of particular note are those regions that offer penetration through the Earth's atmosphere and do not require an artificial source of illumination.

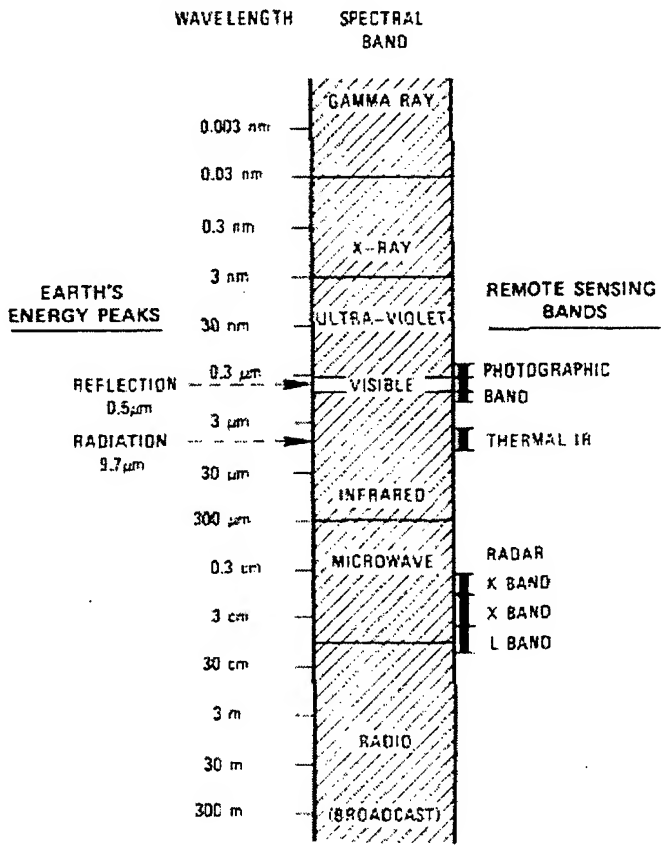

Fig. 2.1 Electromagnetic Spectrum (From Sabins, 1978)

The portion of the electromagnetic spectrum most used in spectral remote sensing ranges from 0.4 μm to 14.0 μm. This region is graphically depicted in figure 2.2.

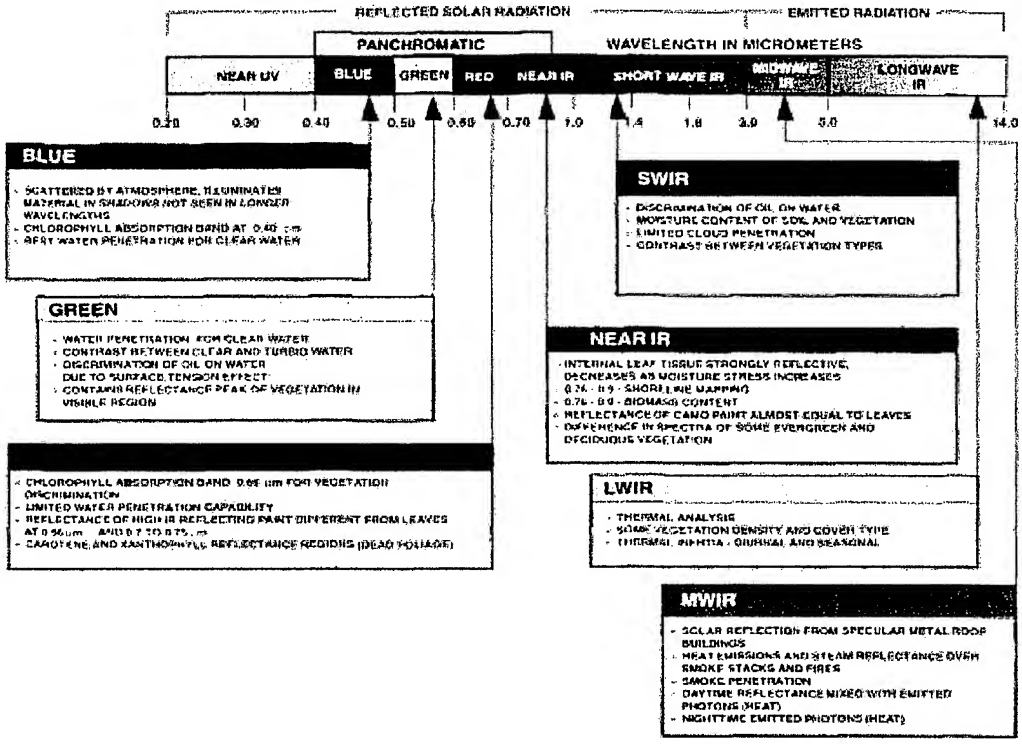

Fig. 2.2 Characteristics of Spectral Regions. (From Multispectral Users Guide, 1995)

Sensors that operate from 0.4 μm to 3.0 μm take advantage of the Sun's illumination, for this region is where solar radiation is dominant. From 3.0 μm to 8.0 μm, both solar illumination and thermal self-emission contribute and must be accounted for. From 8.0 μm to 14.0 μm, the self-emission of thermal energy by the subject is the most dominant feature. For the purposes of this thesis, the region referred to as the *reflective spectrum*, from 0.38 to 3.0

μm (Campbell, 1996) will be discussed in some depth. The lower bound is chosen because below 0.38 μm (ultra-violet), ozone absorbs solar emission.

3. Generation and Emission of Electromagnetic Radiation

Electromagnetic radiation is generated by the conversion of energy from other forms, such as kinetic, chemical, or nuclear. (Elachi, 1987) The energy of the radiation being generated depends on the efficiency of the conversion process.

Higher frequency waves in the infrared and visible regions of the electromagnetic spectrum are generated by molecular excitation (vibrational or orbital) followed by decay from the excited state. Because energy is conserved, the energy released is equal to the energy difference between the two states.

Any object that is not in thermal equilibrium with its surroundings will undergo a transfer of energy between the object and its environment. This energy will be emitted by means of conduction, convection, and/or radiation. For the Sun radiation is the mechanism that is important.

An ideal source, also known as a black body, emits the maximum amount of heat energy in the form of radiation into its environment. The spectral emittance of a black body is described by Planck's Formula as:

$$S(\lambda) = \frac{2\pi hc^2}{\lambda^5} \frac{1}{e^{hc/\lambda kT} - 1} \quad (2\text{-}1)$$

where k is the Boltzman constant, h is Planck's constant, c is the speed of light, λ is the wavelength, and T is the absolute temperature in Kelvin. Figure 2.3 illustrates the behavior of black bodies at various temperatures. Note the change in scale between figures 2.3 (a) and (b). What must be recognized is that in the region of the electromagnetic spectrum that NVIS operates, the sun's radiation is the primary contributor. The sun may be modeled as a black body with a temperature of 6000° K. (Elachi, 1987)

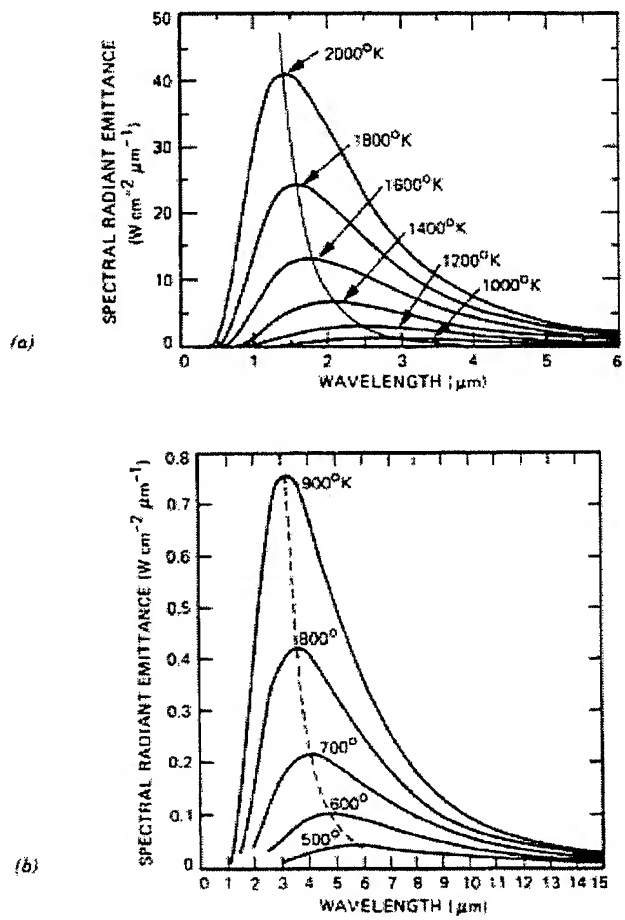

Fig. 2.3 (a), (b) Spectral Emittance of Black Bodies of Various Temperatures (From Elachi, 1987)

The maximum spectral emittance is at the wavelength:

$$\lambda_m = \frac{a}{T} \quad (2\text{-}2)$$

where a = 2898 μm°K. Summing $S(\lambda)$ over the entire spectrum gives a total emitted energy as described by the Stefan-Boltzman law:

$$S = \sigma T^4 \quad (2\text{-}3)$$

where σ = 5.669x10^{-8} Wm^{-2}K^{-4}. These terms are important in that they define measurable characteristics of a black body and can be used to model the Sun. It is important to note the wavelength of maximum spectral emittance because this defines the point of maximum energy radiated from the source. The total emitted energy is important in that for instrument calibration purposes, the source lamp can be approximated as a black body of a certain temperature.

Real bodies cannot exhibit the thermal energy conversion properties of a black body. To compare real or gray bodies, the concept of emissivity is used. By definition, emissivity (ε) is the ratio between the emittance of a given object (M) and that of a black body of the same temperature (M_b):

$$\varepsilon = \frac{M}{M_b} \quad (2\text{-}4)$$

The emissivity of a black body would therefore be 1, and that of a perfect reflector would be 0. (Campbell, 1996)

4. Interaction of Electromagnetic Waves With Matter

Electromagnetic waves interact with matter through influencing the basic constituents of the matter. The waves act on the electrons, molecules, and/or nuclei of the incident material, putting them in motion (rotation, vibration, or displacement).

In the visible and near infrared, vibrational and electronic energy transitions play the key role. In the case of solids the close proximity of the atoms in the crystalline structure leads to a wide variety of energy transfer phenomena with broad interaction bands. (Elachi, 1987) Each material has its own individual spectral signature, and this signature is used to identify materials in a scene.

5. Detection of Electromagnetic Radiation

The radiation reflected, scattered, or emitted from an object generates a radiant flux density surrounding the object which contains information about the object's properties. A collector and detector are used to capture and measure this radiation.

In the Ultraviolet, Visible and Infrared regions, the collector is generally a lens or reflecting surface that concentrates the intercepted energy onto the detector. By converting the incoming energy into another form of energy such as heat or electric current, the radiation can be detected.

B. SOLID SURFACE SENSING IN THE VISIBLE AND NEAR INFRARED

The visible and near infrared spectral regions are the most commonly used in remote sensing of the Earth. This is because the Sun is used as the major source of illumination and because sensors for these regions are the most widely available. The sensor detects the radiation reflected off the surface and this is read as at-sensor radiance. By comparing this radiance with the original incident radiation at the surface (which may be obtained by hand-held spectrometers; this process is known as ground-truthing), the reflectivity can be determined. This reflectivity is used to determine information about the materials in the detected surface and is independent of the incident radiation. This is illustrated in figure 2.4. (Elachi, 1987)

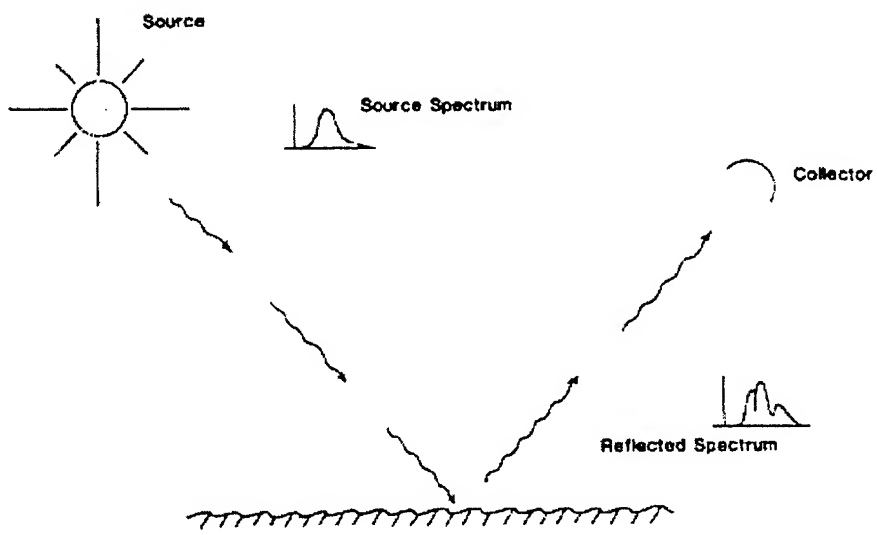

Fig. 2.4 Illustration of the Mechanics of Remote Sensing (From Elachi, 1987)

1. Spectral Characteristics of the Source

The Sun is the most obvious choice to be the source of illumination for viewing in the visual and near infrared regions of the electromagnetic spectrum. As a rough approximation, the Sun can be treated as a black body at a temperature of 6000° K. The solar illumination spectral irradiance at the Earth's surface is shown in figure 2.5. The total irradiance is measured at about 1370 W/m^2 above the Earth's atmosphere.

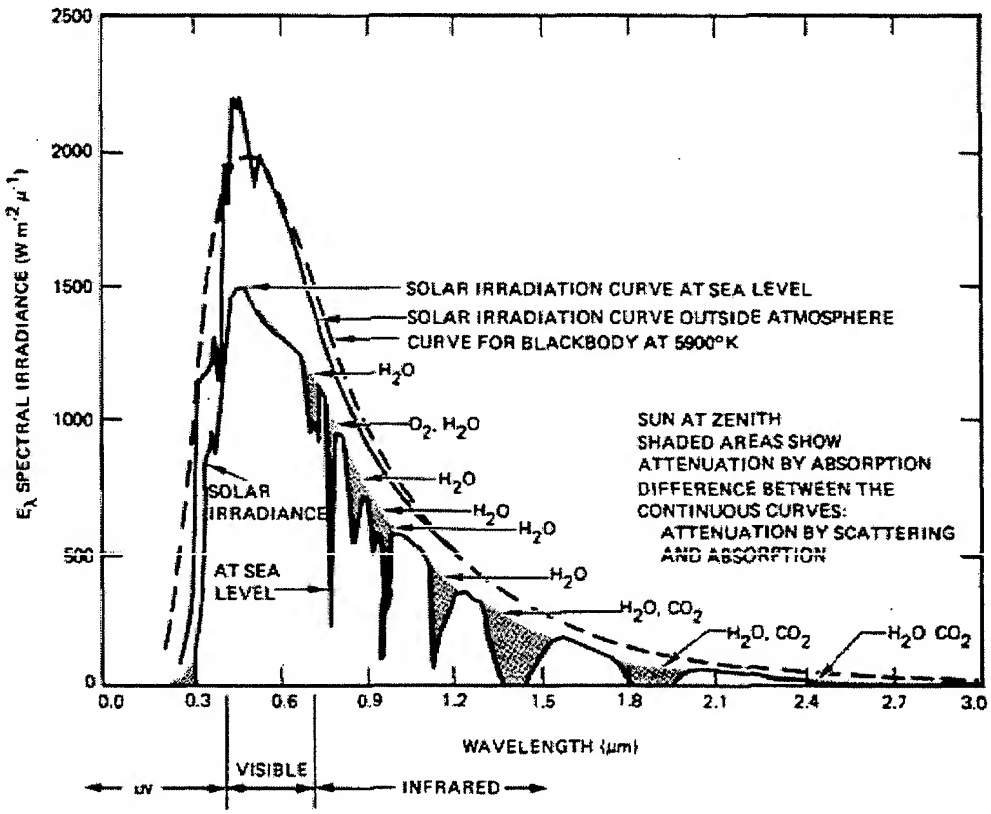

Fig. 2.5 Sun Illumination Spectral Irradiance at the Earth's Surface (From Elachi, 1987)

2. Atmospheric Effects

The atmosphere severely complicates accurate collection of remote sensing data. Because of this, the effect of the atmosphere must be accounted for when collecting information.

The path of solar radiation from entry into the atmosphere, reflection off the target and thence into the collector is made complicated by atmospheric scattering. The atmosphere serves to simultaneously attenuate the energy illuminating an object (and the energy reflecting off of it), while it also serves to reflect energy from other, non-targeted sources to the reflector. This is illustrated in figure 2.6.

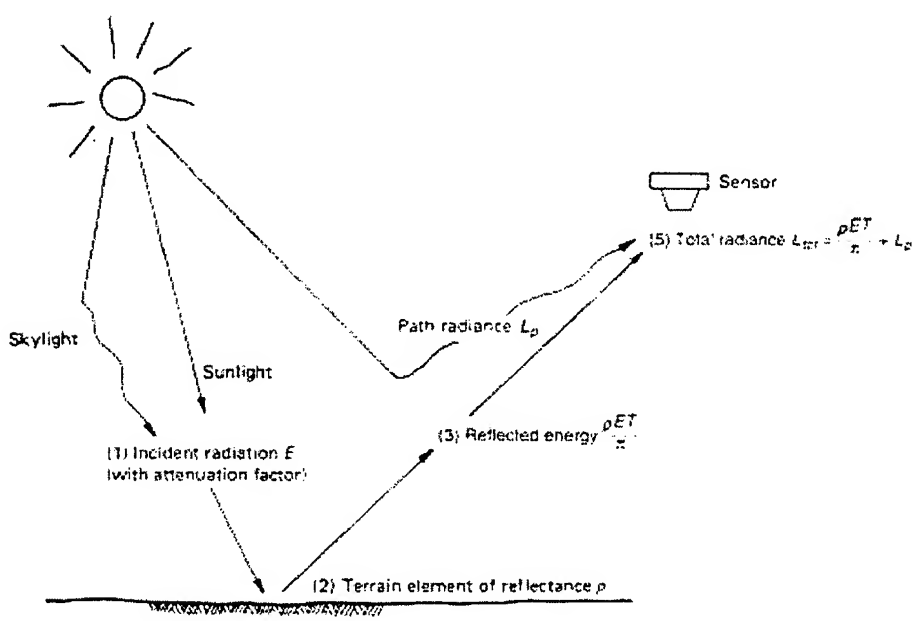

Fig. 2.6 Atmospheric Effects Influencing the Measurement of Reflected Solar Energy (From Lillesand, 1994)

When both effects are expressed mathematically, the total energy observed by the detector may be expressed in terms of the reflectance of the target and the incident solar illumination. This follows as:

$$L_{TOT} = \frac{\rho ET}{\pi} + L_p \quad (2\text{-}5)$$

where L_{TOT} is the total spectral radiance measured by the sensor, ρ is the reflectivity of the object, E the irradiance on the object, T the transmission of the atmosphere, and L_p the path radiance (reflected energy from the atmosphere.) It must be recognized that each of these factors changes with wavelength.

Because the regions of note are the visual and near-infrared, certain complications that are present in the thermal regions of the infrared may be ignored. If a sensor is used that is sensitive to thermal infrared, the emittance of the target itself must also be considered. Since the Earth's surface generally exists at temperatures around 300°K it emits virtually no radiation in the visible and near-infrared portions of the spectrum, so self-emission may be ignored.

The atmosphere of the planet preferentially absorbs portions of the emitted spectrum. The most prevalent constituents of the atmosphere that contribute to absorbing solar radiation are water vapor, carbon dioxide, and ozone. (Lillesand, 1994) Because these gasses absorb in very specific regions of the electromagnetic spectrum, it drives the observer to look in other, non-absorbed regions. The regions of the spectrum that have little absorption of solar radiation are generally referred to as *atmospheric windows.*

Scattering of solar radiation is caused by molecular density fluctuation, and all atmospheric constituents contribute to the effect. The combined effect is computed as a function of atmospheric density and pressure. The effect of gasses on the transmission of solar radiation is shown in figures. 2.7 a-f.

In the visible spectrum, transmission is mainly affected by ozone and molecular scattering (figure 2.7, c, d). Molecular scattering was first described by Rayleigh in 1871 and is known as Rayleigh scattering. Its contribution to the vertical path transmittance (T_r) to space is expressed by optical thickness (τ_r):

$$T_r = e^{-\tau_r} \quad (2\text{-}6)$$

The Rayleigh optical thickness τ_r decreases as a function of wavelength (λ) as about λ^{-4}. Since air density is proportional to pressure P, the vertical optical thickness between the top of the atmosphere and a certain level with pressure P can be given by:

$$\tau_r(P) = \tau_r(P_0) \, {}^{P}\!/_{P_0} \quad (2\text{-}7)$$

In the near IR region, a strong oxygen band can be seen at 0.76 μm (figure 2.7 c). Also, a few water vapor and carbon dioxide bands restrict the regions available for absorption free remote sensing. Because of these bands, data taken in these specific ranges may not be useful in describing the area being sensed.

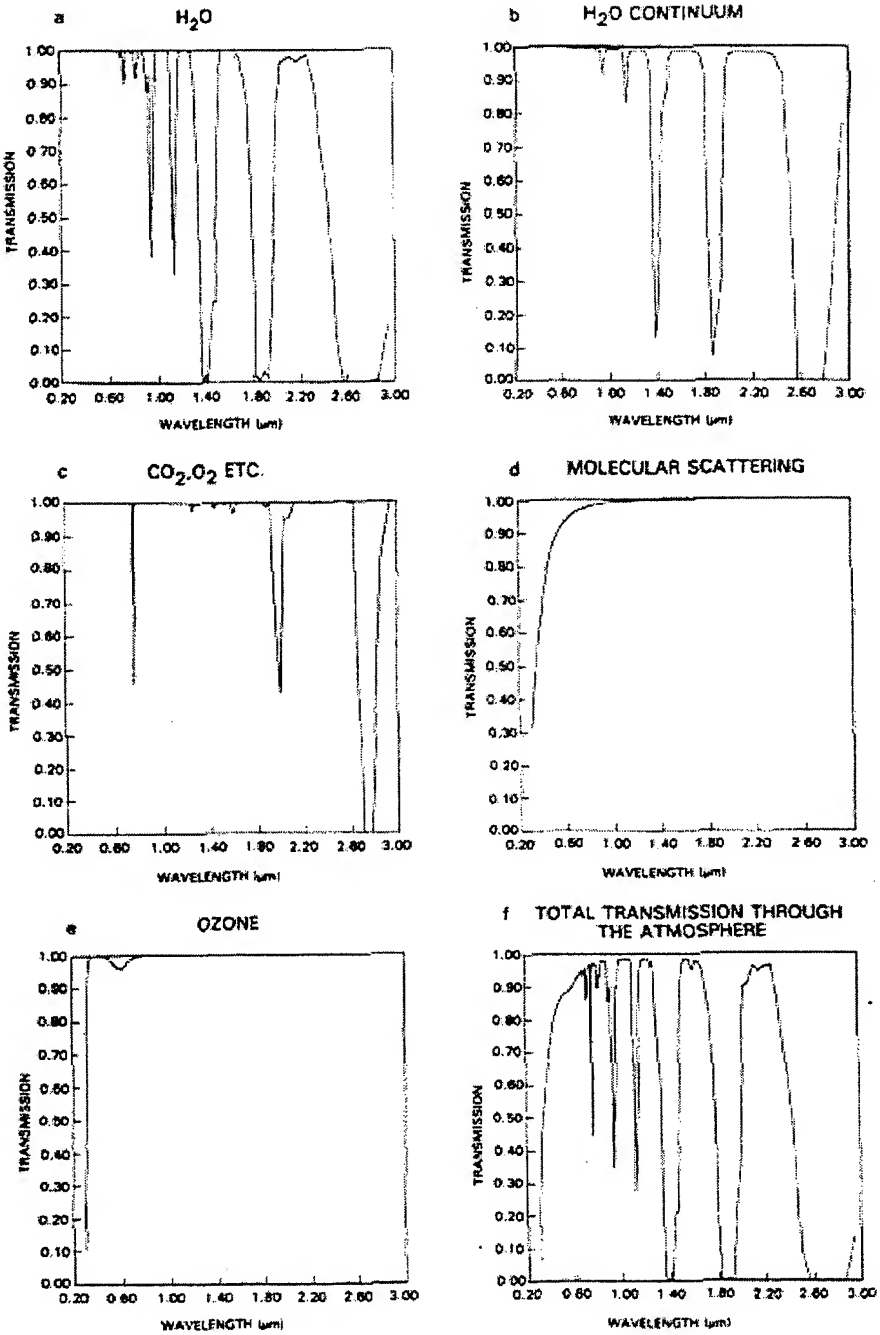

Fig. 2.7 Atmospheric Transmission for the Standard U.S. 1962 atmosphere computed by Lowtran code (Kneizys, 1983) for Sun at Zenith. Attenuation due to: (a) water bands, (b) water continuum, (c) CO_2, O_2, and other minor absorbers, (d) molecular scattering, (e) ozone absorption, and (f) total transmission (From Asrar, 1989)

The density of dry atmospheric gas, $n(z)$, decreases as an exponential with respect to height z from sea level ($z = 0$):

$$n(z) = n(0)\exp(-z/H) \quad (2\text{-}8)$$

where H is the scale height of 8 km (Fraser, 1976). Atmospheric pressure also decreases exponentially with respect to height, because it results from the integration of equation 2-8. (Asrar, 1989)

Water vapor concentration is highly variable. This variability results from the variation in water vapor sources (from evaporation) and losses (clouds/precipitation). Carbon Dioxide is fairly stable throughout the atmosphere, except near large sources such as cities. Ozone is generally restricted to the stratosphere (20-50 km above the surface of the Earth). Figure 2.5 illustrates the effect of the atmosphere on the incident solar illumination.

Aerosols in the atmosphere must also be accounted for to accurately predict the effect of the atmosphere on solar radiation. Aerosols refer to the liquid and solid matter suspended in the atmosphere. To understand the effects of aerosols on remote sensing, one must understand the nature of the aerosol, which requires knowledge of its origin and how it was formulated. Because of this complexity, a model must be formulated to take into account effects from aerosols. This model must take into account the geographic location and the season. Cloud effects are similar to aerosol, however, in the visible and near infrared portions of the spectrum, clouds are highly reflective.

With regards to atmospheric effects, what must be understood is that these effects can be predicted and accounted for. Instead of preventing remote sensing, the atmosphere just adds complications that can be overcome. Also, because NVIS is an airborne platform vice a satellite, the effect is not quite as large, but it must still be accounted for.

3. Wave-Surface Interactions

How electromagnetic radiation interacts with a material affects the radiation subsequently reflected off the material. The most basic description of these interactions includes reflection, transmission, and scattering. Transmission of the radiation is not of concern, because this energy will not be detected by the sensor. Scattering serves to complicate detection, because energy that comes from other, non-target sources may be detected by the sensor. Direct reflection off the target is the simplest means of sensing the target.

Reflection varies depending on the surface illuminated. For a very smooth (λ >> interface roughness) specular reflection is preeminent. However, most natural surfaces are rough relative to the visible wavelengths. Scattering, therefore, plays a larger role.

For a particulate surface, the incident wave is scattered and some of the incident radiation penetrates the particles. Because of this, any absorption bands of the material deplete the radiation of energy in this band. As the particles increase in size, these bands become even more pronounced

The reflection of visible and near-infrared waves from natural surfaces occurs within the top few microns of said surface. Therefore, surface cover plays a very important role. For

example, the iron oxide in desert varnish (the topmost layer) can completely mask the spectrum of the material underneath (Elachi, 1987).

4. Signature of Solid Surface Materials

Solid surface materials can be classified as one of two types: geologic and biologic. Geologic materials obviously are soil and rocks. Biologic corresponds to vegetation cover.

In the visible and near-infrared regions, the signatures of geologic materials arise mainly due to electronic and vibrational transitions. A spectral signature diagram for a variety of geological materials is illustrated in figure 2.8.

The presence of chlorophyll in vegetation leads to a strong absorption of wavelengths shorter than 0.7 μm. Between 0.7 and 1.3 μm, the strong reflectance is due to the refractive index continuity between air and the leaf cell. (Elachi, 1987) Due to the dominant presence of water in vegetation, the spectral signature of plants looks virtually equivalent to the signature of water in the spectral region from 1.3 to 2.5 μm.

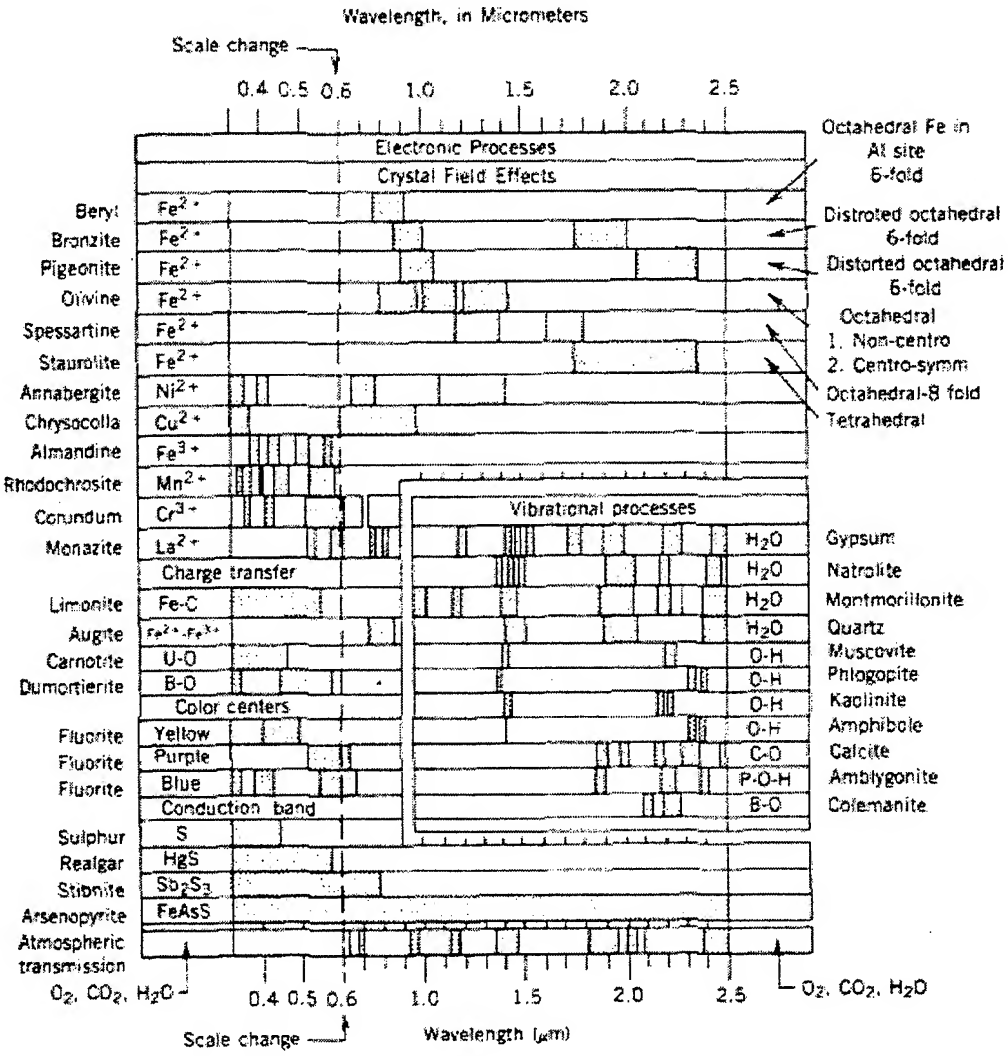

Fig. 2.8 Spectral Signature Diagram of a Variety of Geologic Materials (From Elachi, 1987)

The differences between materials provide an opportunity to discriminate between them using their detected reflectivity. Libraries of spectra have been collected for use in geology and agriculture (for detection of certain types of rock or vegetation.)

C. SPECTRAL DETECTORS

Spectral detectors can be characterized by several different aspects of their design. The region of the electromagnetic spectrum, the number of bands the detector collects, and the resolution of the spectral bands all serve to determine the spectral nature of a detector. Spatially, the ground resolution as defined by type of device and altitude can differentiate detectors. Finally, the method used to collect information also differentiates detectors.

1. Spectral Characteristics

The region of the spectrum one wishes to observe defines various characteristics of the detector. Detectors operating in regions of the spectrum that provide solar illumination or that can detect thermal emissions do not require an artificial illumination source. Unfortunately, one aspect of detecting in the visual/near-infrared region is the requirement to have solar illumination, i.e. daylight is required.

The number of bands detected defines what type of spectral detector is being used. A multispectral detector would detect tens of bands, hyperspectral hundreds of bands, and ultraspectral thousands of bands, as defined by the Multispectral Users Guide, 1995, and illustrated in figure 2.9. The resolution of the bands corresponds somewhat to the

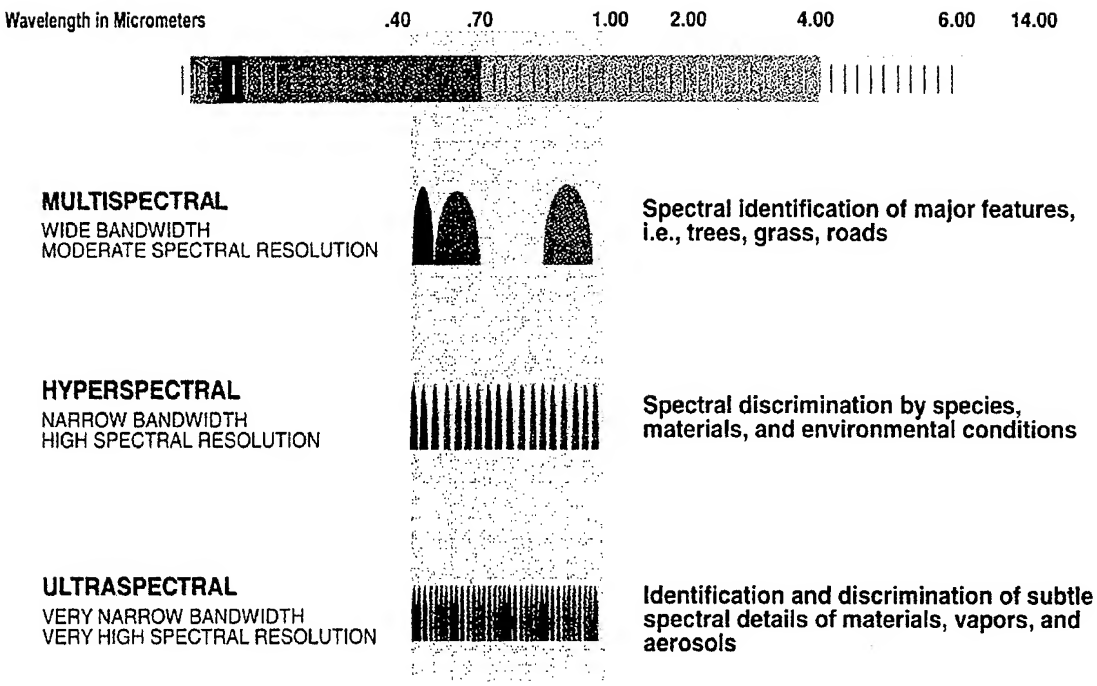

Fig. 2.9 Classifications of Spectral Imagers (From Multispectral User's Guide, 1995)

number of bands studied. The resolution defines the width of the section of the spectrum observed per spectral band. As the number of bands increases (together with reducing the width of the spectral bins), the detail and granularity of the data collected increases. This translates to picking up finer and finer spectral details of the scene being studied.

2. Other Characteristics

There are different methods that can be used to construct a spectral detector. A common detector type and the type chosen for NVIS is the pushbroom imaging system. In the

pushbroom detector, the forward motion of the detector provides for the view of the detector (figure. 2.10).

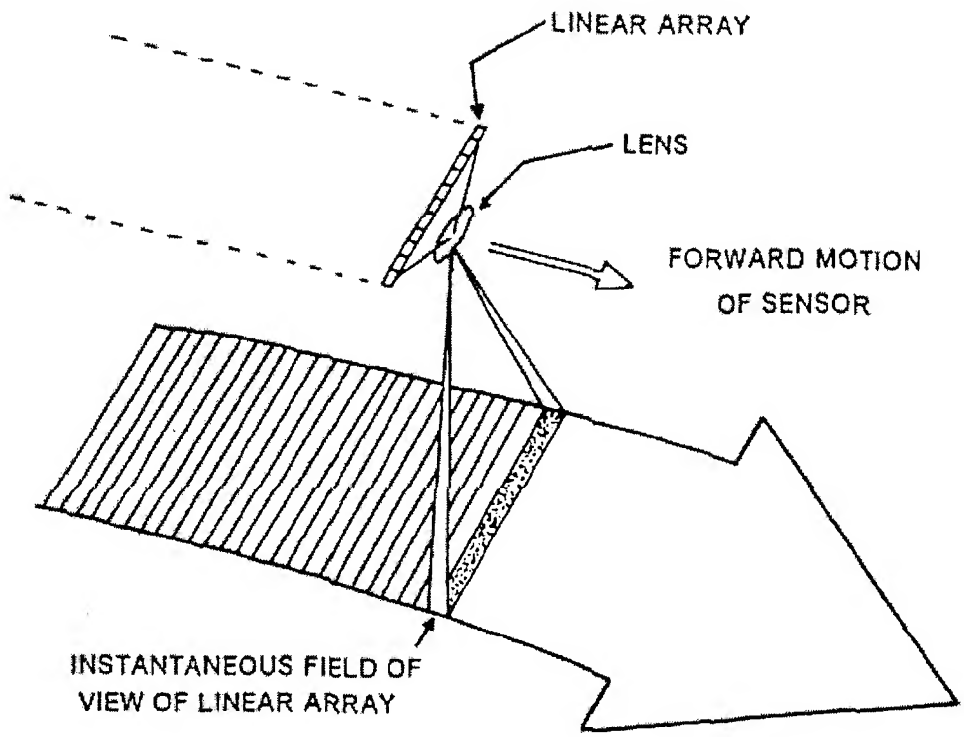

Fig. 2.10 A Pushbroom Scanner (From Campbell, 1996)

The geometry of the detector element itself defines the 'footprint' of the detector on the ground, so obviously this footprint will change in size as the altitude of the system changes. The pushbroom system has comparative advantages over other types, in that it provides longer dwell time over a given area and has no moving parts. However, to give the detector a reasonable observed area, the detector element must be made wider than similar detectors. This causes

problems with distortion near the edges of the detector view. Also, pushbroom detectors are limited in swath width by the dimension of the spectral array.

THIS PAGE INTENTIONALLY LEFT BLANK

III. NIGHT VISION IMAGING SPECTROMETER

The Night Vision Imaging Spectrometer (NVIS) is a hyperspectral imager designed and built by TRW as the TRWIS III. It is an instrument with 384 contiguous spectral channels with bandwidths of 5.25 nm in the Visible/Near-Infrared (VNIR) (Folkman, Gleichauf, 1996) and 6.25 nm in the Short-wave Infrared (SWIR) regions respectively. The 384 spectral channels are simultaneously collected from each pixel in the scene. The entire wavelength range from 0.4 to 2.5 μm is covered at a signal to noise ratio of several hundred to one. The instrument is calibrated at each wavelength to within 5% absolute radiometric accuracy. It can operate on various aircraft or Unmanned Airborne Vehicles (UAV's) (Folkman, DeLong, 1996).

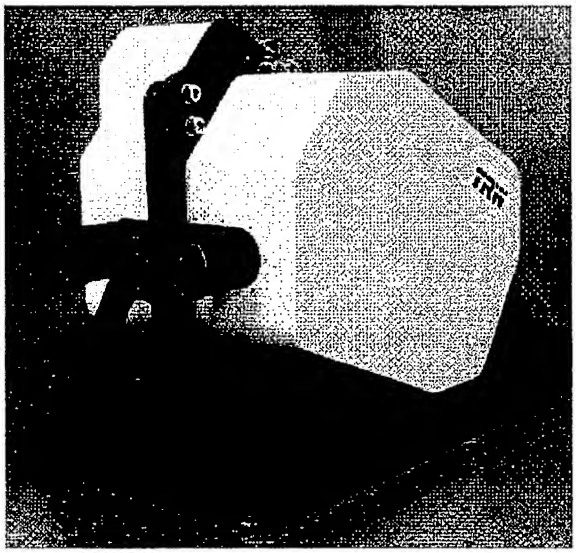

Spectrometer Head

Fig. 3.1 NVIS (From Simi, 2000)

A. SYSTEM DESIGN

The instrument includes a sensor head containing a pair of co-boresighted grating spectrometers and two electronic racks. The VNIR spectrometer covers the wavelength range from 370 to 1040 nm and the SWIR spectrometer ranges from 890 to 2450 nm. The overlap between the two from 890 to 1040 nm allows verification of image co-registration and cross-calibration (Folkman, Gleichauf, 1996). Each spectrometer consists of a set of refractive foreoptics that image the scene onto a slit. Light passes through the slit and is dispersed perpendicular to the slit by a flat grating. The light is then imaged onto a two-dimensional focal plane array (FPA). One dimension of the array, the dimension along the slit, provides spatial scene information. The second dimension of the array, along which the light from any given point in the slit has been dispersed, provides spectral information. Pushbrooming the image of the slit across the scene perpendicular to the slit and storing subsequent frames of information collected by the FPA's generates a two-dimensional spatial image with 384 spectral bands per pixel (Folkman, DeLong, 1996). Simultaneous collection of the spatial and spectral information offers superior data to those instruments (such as AVIRIS) that collect the information separately, in that processing time is shortened and image quality is not as degraded (Folkman, Gleichauf, 1996).

The instrument is designed to interface with many aircraft. The variable frame rate of the instrument (15, 30 or 60 Hz) allows for flight plans anywhere from 600 m to 12 km in altitude and covers the flight envelope of most aircraft in these altitude ranges. The 0.85 mrad

instantaneous field of view (IFOV) of the instrument results in spatial resolution from 0.5 to 11 m, depending on altitude. The cross track field of view (FOV),

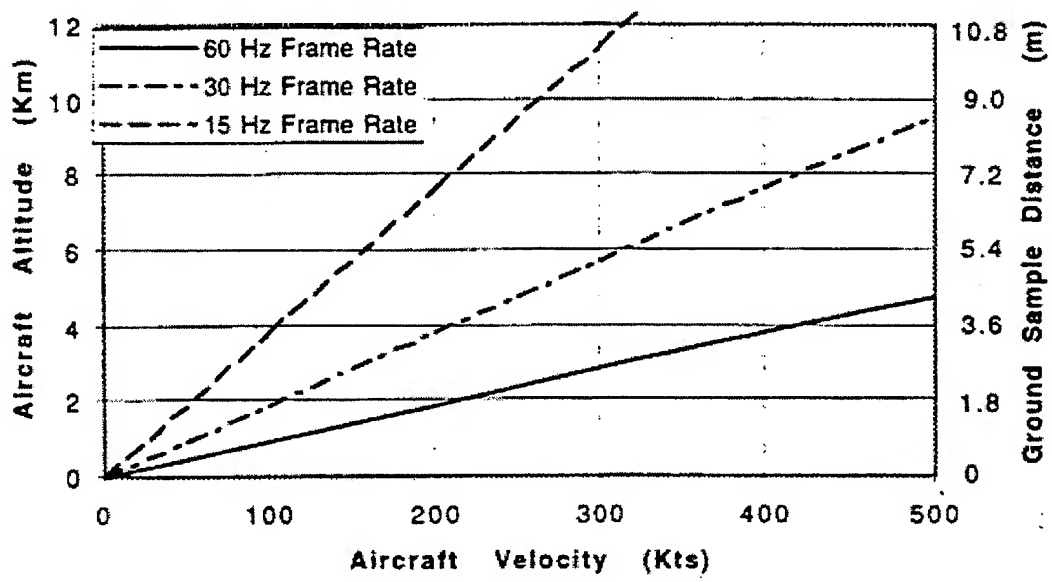

Fig. 3.2 Aircraft Velocity and Altitude as a Function of Frame Rate and Ground Sample Distance (From Folkman, DeLong, 1996)

meaning the range of view for the detector, ranges from 128 m to 2.8 km with the along track FOV limited only by the number of frames collected (Folkman, DeLong, 1996).

B. OPTICAL/MECHANICAL DESIGN

Both spectrometers are similar in optical configuration (see Appendix A). Both have multi-element refractive foreoptics which image the scene onto the entrance slit of the spectrometer. Light passes through the slit and is reflected by an off-axis aspheric element onto a flat, blazed grating where it is dispersed. The reflected light from the grating is reflected by a

second off-axis aspheric element and imaged onto the FPA. Refractive correction lenses are located at two places, behind the slit and in front of the FPA, to minimize field distortion. If uncorrected this distortion would result in excessive spatial mis-registration of spectral channels and cross track spectral errors. This type of error, also known as 'smile' will be explained in more detail in the following sections. An order-sorting filter is located immediately above the surface of each FPA to eliminate order overlap (Folkman, DeLong, 1996).

The optics and FPA assemblies are secured in custom mounts that provide for precision adjustments when required for proper alignment. An enclosure is attached to the baseplate to seal the optical system from the outside environment. All mounts and interior surfaces are painted black to minimize stray light effects (Folkman, DeLong, 1996).

C. FOCAL PLANE ARRAYS

The focal plane module for the VNIR spectrometer is a custom silicon CCD made by Loral Fairchild Imaging Sensor. The basic pixel size is 20 microns with an image area format of 768x384 pixels, spatially by spectrally, respectively. When outputted, the pixels are binned 3x3 resulting in an image array of 256x128 binned 60 micron pixels (Folkman, DeLong, 1996).

The focal plane of the SWIR spectrometer is a custom Mercury Cadmium Telluride photodiode array and CMOS multiplexer hybrid made by Rockwell International. The array has a format of 256x256 pixels, with each pixel being 60 microns square. As the normal operating temperature is 115° Kelvin, the array is mounted in a Dewar and is cooled by a Stirling-cycle cooler. Each pixel on the detector array is coupled to its own Capacitive Trans-

Impedance Amplifier (CTIA) in the CMOS multiplexer and then coupled via switch FET's to one of four output buffers in the device. The hybrid is secured into a ceramic substrate that is mounted to the end of the cold finger inside the Dewar (Folkman, DeLong, 1996). The detector is optimized from 900 to 2450 nm. The cutoff at 2450 nm minimizes thermal background noise (Folkman, Gleichauf, 1996).

D. CHARACTERIZATION MEASUREMENTS

The various parameters of interest for the NVIS detector are collected in Table 3.1. The explanation of these parameters follows.

Table 1: NVIS System Performance for SWIR Spectrometer		
Parameters	**Required Performance**	**Achieved Performance**
Spectral Range	0.80 to 2.40 um	0.904 to 2.40 um
Number of Spectral Channels	256	256
Spectral Resolution	6.25 nm	6.04 nm
Instantaneous FOV	0.90 mrad	0.882 mrad
Full FOV	13.1 deg	12.94 deg
Aperture	21.2 mm	19.1 mm
Effective Focal Length	70 mm	68.66mm
Data Output	12 bit digital	12 bit digital
Frame Rate	15 to 60 Hz	15, 30 and 60 Hz (Selectable)
Integration Time	1/128-125/128 of frame	1/128-125/128 of frame
Signal to Noise Ratio (goal) @ 5% albedo	>50 @ 10nm resolution, all bands	>50 @ 10nm resolution, 1.0 to 2.1um, 15 Hz

Table 2: NVIS System Performance for VNIR Spectrometer		
Parameters	**Required Performance**	**Achieved Performance**
Spectral Range	0.40 to 1.00 um	0.38 to 1.03 um
Number of Spectral Channels	128	128
Spectral Resolution	5.0 nm	5.08 nm
Instantaneous FOV	0.90 mrad	0.875 mrad
Full FOV	13.1 deg	12.83 deg
Aperture	21.2 mm	19.05 mm
Effective Focal Length	70 mm	68.53 mm
Data Output	12 bit digital, 1 port	12 bit digital, 1 port
Frame Rate	15 to 60 Hz	15, 30 and 60 Hz (Selectable)
Integration Time	93% of Frame Time	>93% of frame time
Signal to Noise Ratio (goal) @ 5% albedo	>50 @ 10nm resolution, 0.40 to 0.90 um	>50 @ 10nm resolution, 0.425 to 0.90 um

Table 3.1. NVIS Sensor Specifications (From Simi, 2000)

1. Modulation Transfer Function (MTF)

A way to measure the performance of a detector so that it can be compared in an objective sense with other detectors is the Modulation Transfer Function (MTF). To put it simply, the MTF is a measure of the magnitude response of a detector when looking at different spatial frequencies (Boreman, p.25). A more rigorous description of MTF can be found in Asrar, 1989. The results of the MTF tests for the VNIR and SWIR arrays are shown in figure 3.3.

MTF at 15 FPA Locations on VNIR

A	0.362
B	0.322
C	0.316
D	0.318
E	0.299
F	0.408
G	0.362
H	0.336
I	0.351
J	0.350
K	0.420
L	0.403
M	0.368
N	0.396
O	0.368

spectral

471	603	705	827	928
A	B	C	D	E
F	G	H	I	J
K	L	M	N	O

spatial

MTF at 15 FPA Locations on SWIR

A	0.237
B	0.368
C	0.361
D	0.247
E	0.178
F	0.235
G	0.303
H	0.276
I	0.252
J	0.212
K	0.221
L	0.265
M	0.233
N	0.233

spectral

953	1266	1652	2037	2350
A	B	C	D	E
F	G	H	I	J
K	L	M	N	O

spatial

Fig. 3.3 NVIS MTF Characterization (From Simi, 2000)

2. Crosstrack Spectral Error

The sensor artifact known as 'smile' is caused by distortion in the monochromatic image of the spectrometer slit onto the focal plane and/or by a rotation of the rows of focal plane

pixels relative to the slit. This error was measured by imaging a monochromatic slit target onto a certain crosstrack pixel location. The target was oriented perpendicular to the spectrometer slit, thus effectively creating a point target in the crosstrack axis which was insensitive to in-track motion.

The source was positioned at one edge of the crosstrack field of view and the wavelength set to a specific value. Then the target was moved across the field of view of the detector, stopping at the center of the field of view to readjust back to the desired wavelength. Then the target was moved to the opposite edge of the field of view of the detector. The process was carried out for 475 nm, 700 nm, and 900 nm spectral channels for the VNIR, and 953 nm, 1797 nm, and 2414 nm for the SWIR. (Folkman, Sandor, 1997)

The effect of poor smile characteristics would have an undesirable effect on classification algorithm performance. Most striking, a homogeneous scene may be divided into several different classes if there is a large variation in band center assignment as a function of cross track pixel position. Measurements indicate that the VNIR spectrometer's smile effect appears to be mild, with band center variations of ± 0.3 spectral pixels or 1.5 nanometers in the extreme case. The SWIR system was found to have a more pronounced smile effect and this was determined to be caused by a slight rotation of the FPA. This rotation shifts the band centers by approximately 1.3 spectral pixels as shown in figure 3.4. This smile can be compensated for in post-processing calibration. (Simi, 2000)

Spectra of Atmospheric CO_2 Taken From Left and Right of Focal Plane

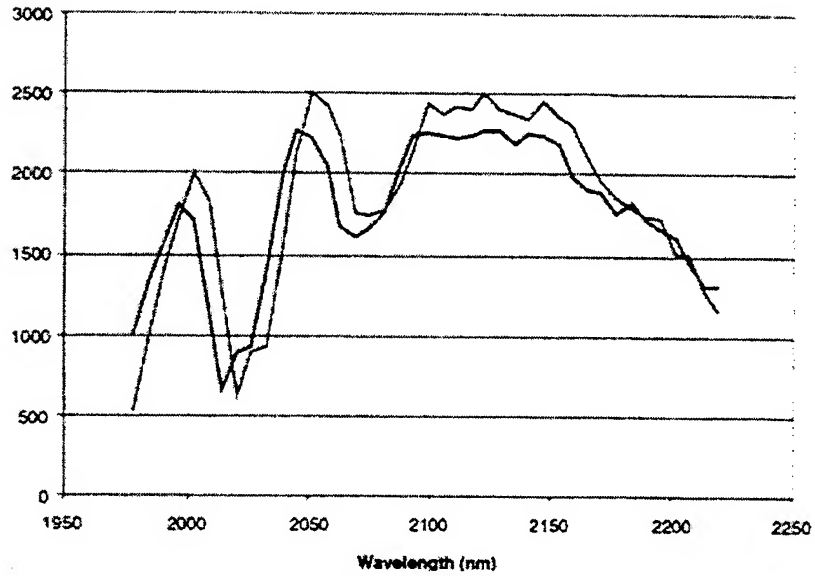

Fig. 3.4 Spectral Shift Due to Smile on SWIR FPA (From Simi, 2000)

3. Spatial Co-Registration of Spectral Channels

Spatial Co-Registration ensures that for a given spatial dimension, as the spectrum is varied, the spatial dimension remains centered. A measure of this is how much the spatial dimension varies as the spectrum is changed. To measure this, a procedure very similar to that for measuring Spectral error is carried out, however, the target is fixed to center on the spatial channel. Then the target wavelength is varied from its original value of 475 nm to various other values for the VNIR and SWIR. The worst-case values for spatial co-registration (at the edges of the focal arrays) were <20% of IFOV for both the VNIR and SWIR. (Folkman, Sandor, 1997)

4. Spectral Calibration and Spectral Purity

Spectral Calibration was done during the Crosstrack Spectral Error measurements. Spectral calibration is simply a measure of the bandwidth of the spectral bins, whereas spectral purity measures the effect of spectral cross-talk. This phenomenon is the result of energy that is directed to a certain spectral bin being detected by other bins, most likely those adjacent to it.

Once the output wavelength of the target had been adjusted for a given spatial location, the center wavelength of the bin was recorded. This was done at the various spatial locations of the target. (Folkman, Sandor, 1997) From these measurements the spectral bandwidth was determined for the two instruments as 5.08 nm for the VNIR and 6.04 nm for the SWIR. (Simi, 2000)

Once the exact wavelength had been set on the target, the signal in adjacent spectral channels was measured. (The spectral bandwidth had been preset at predetermined values for the given wavelengths.) The ratios of the signal on the adjacent spectral channels as well as those two and three pixels away to the total signal were calculated and are shown in figure3.5. (Folkman, Sandor, 1997)

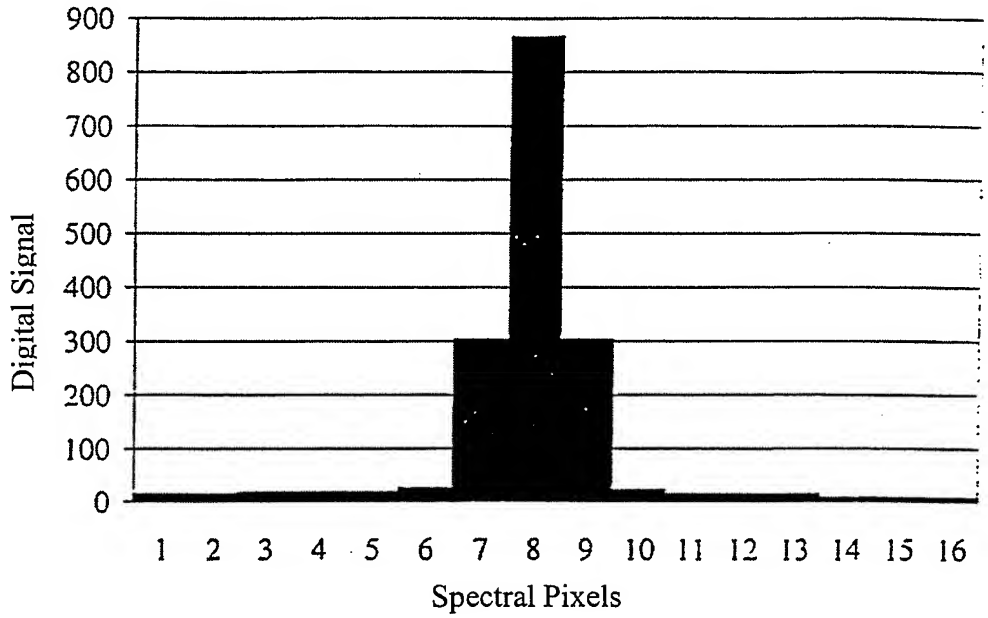

(a) Edge of crosstrack field of view, 1000 nm spectral channel, 3 nm source bandwidth

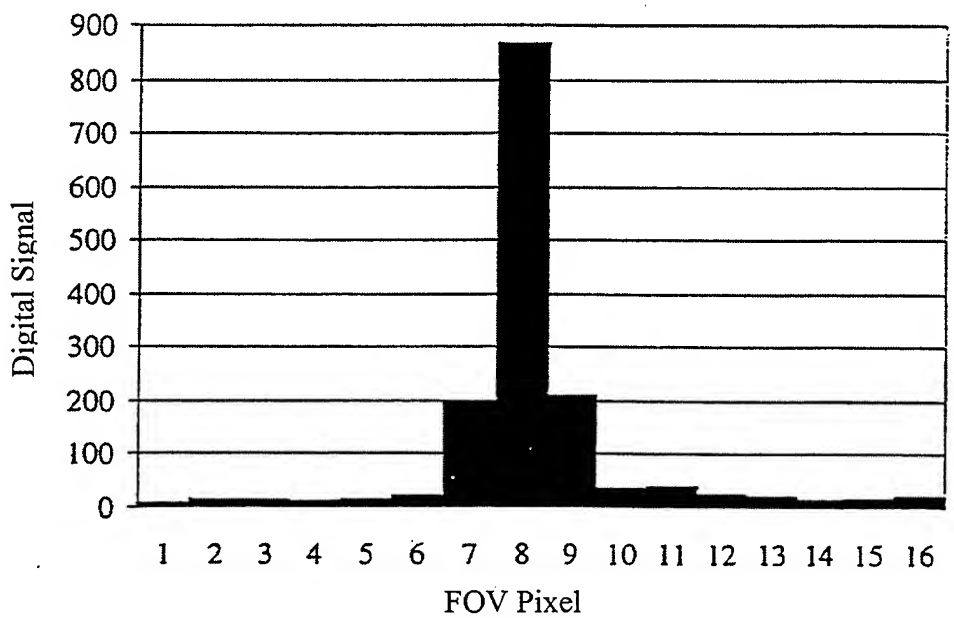

(b) Center of crosstrack field of view, 700 nm spectral channel, 2 nm source bandwidth

Fig. 3.5 Monochromatic Source Images Showing Spectral Band Purity. Each Pixel is 5.25 nm in Bandwidth (From Folkman, Gleichauf, 1996)

E. NVIS DATA CALIBRATION

The raw data produced by NVIS must be calibrated prior to meaningful use. Night Vision Laboratory has developed proprietary software to properly prepare the data for further calibration, e.g. manipulation by ENVI. The software primarily consists of a processing tool and a viewer.

The Hyperspectral Data Processor is a Windows® based software package written in C. It provides spectral processing capabilities that allow the conversion of the raw data captured by the NVIS detector to absolute radiance, as well as allow manipulation of the data set to provide a cleaner product. Spectral processing capabilities also include background subtraction, spatial flat fielding, bad pixel replacement, smile correction, and removal of overlapping bands between the two spectrometers of NVIS. (Simi, 2000)

A separate HSI viewer provides the added capability to view data-cube frames or images, plot spectra at selected points and produce histograms of specific areas. Addition, subtraction, and division of frames can be performed. The viewer specifically assists the user by allowing a view of the data-cube frame by frame. By inspecting the cube in this fashion, the user can immediately see problems with calibration or header information in the data set.

IV. HYPERSPECTRAL DATA TOOLS

Hyperspectral data provides many challenges to the user. Compared to sensors in use before, the amount of data generated by hyperspectral sensors caused a search for tools that allow prodigious amounts of data to be interpreted. A variety of tools provided by the software package ENVI will be evaluated in this thesis, so a review of the various operations is in order.

A. RADIANCE TO REFLECTANCE CONVERSION

While the data generated by the NVIS detector is in terms of radiance, the data is most easily used by the variety of classification algorithms if the data is in terms of the reflectance of the scene. This removes problems associated with varying solar illumination on the scene.

1. Empirical Line Calibration

A method to convert radiance data to reflectance is to use information taken directly from ground measurements. Field spectra must be acquired from the scene, preferably from at least two sources with albedos that span a wide range. Next, pixels must be collected in the target data set that corresponds with the field spectra sources. Then a linear regression is calculated for each band to determine the gains and offsets required to convert the radiance data to reflectance. Finally, the data is multiplied by the gain factor and the offset is added to finish the conversion. The result is the removal of atmospheric effects. (Kruse, Taranik, 1989)

2. Empirical In-Scene Calibration Method

This method is also used to convert from at sensor radiance to reflectance. For each band a histogram of all the pixels in the band is displayed (figure 4.1). The path radiance is removed by adjusting the cutoff of the histogram associated with each band, such that the cutoff in at sensor radiance corresponds to a reflectance of zero. The maximum is adjusted to remove any obvious noise in the figure. To convert to reflectance, each pixel in the scene is divided by the range of the histogram with the new minimum and maximum values. The overall effect is to remove the path radiance from the at sensor radiance, and then to convert this solar irradiance to reflectance.

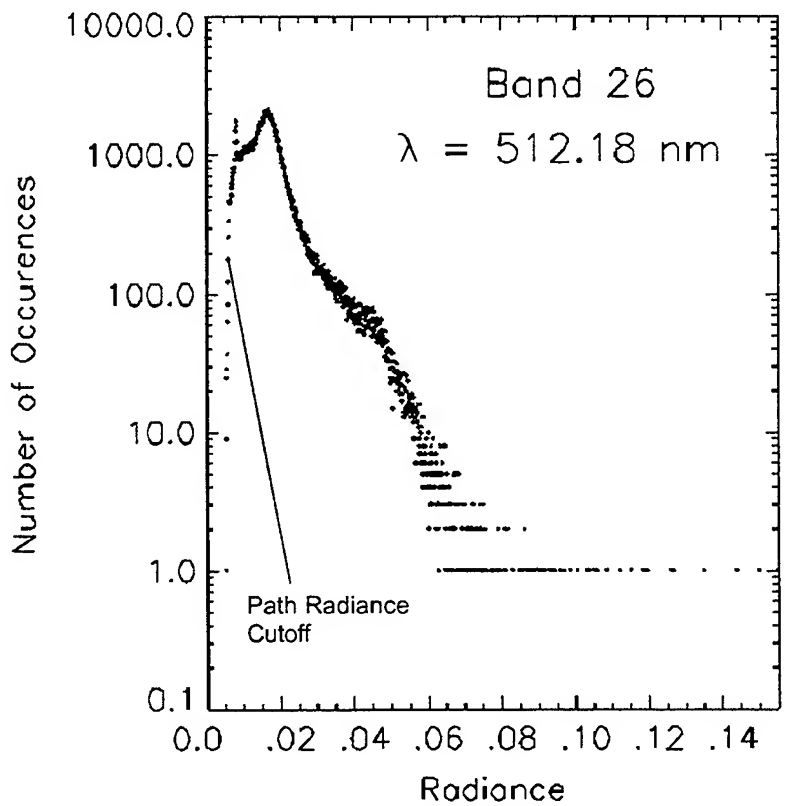

Fig. 4.1 Histogram Illustrating EISC Method

B. PRINCIPAL COMPONENT ANALYSIS

Principal Component Analysis (PCA) is a very useful tool for the manipulation of hyperspectral data. It can be used to discern a great deal of information about the data and the sensor. By using PCA the number of dimensions required to represent the data can be reduced, based on measure of variability. This is very useful in that manipulating the data is more easily accomplished in a data set of reduced dimensionality.

As can be seen by figure 4.2, a comparison between bands in a hyperspectral data set generally will show a degree of correlation between the two bands.

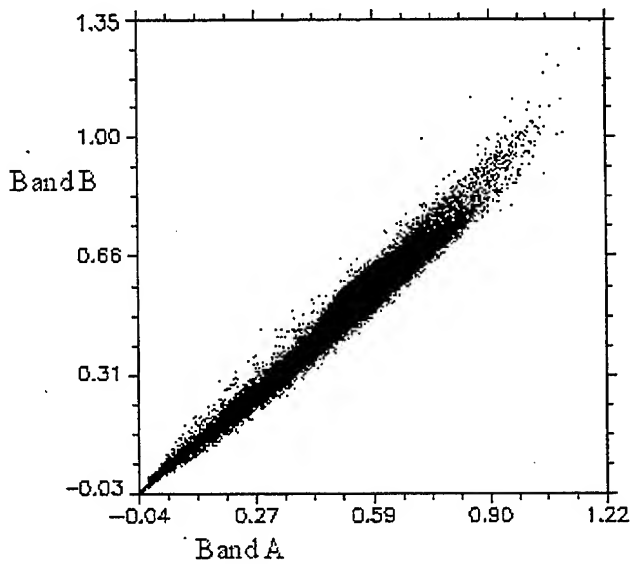

Fig. 4.2 Two-Band Histogram of Hyperspectral Data

That is, an increase in the value of one band is matched by a corresponding increase in the other band. Uncorrelated data would have no corresponding increase. A rotation of the plot can be performed such that the horizontal axis of the new plot lies along the direction of correlation between the two bands. This rotation may provide a more revealing view of the data. This rotation transformation is illustrated in figure 4.3. The extension to higher dimensions is mathematically straightforward, if harder to visualize.

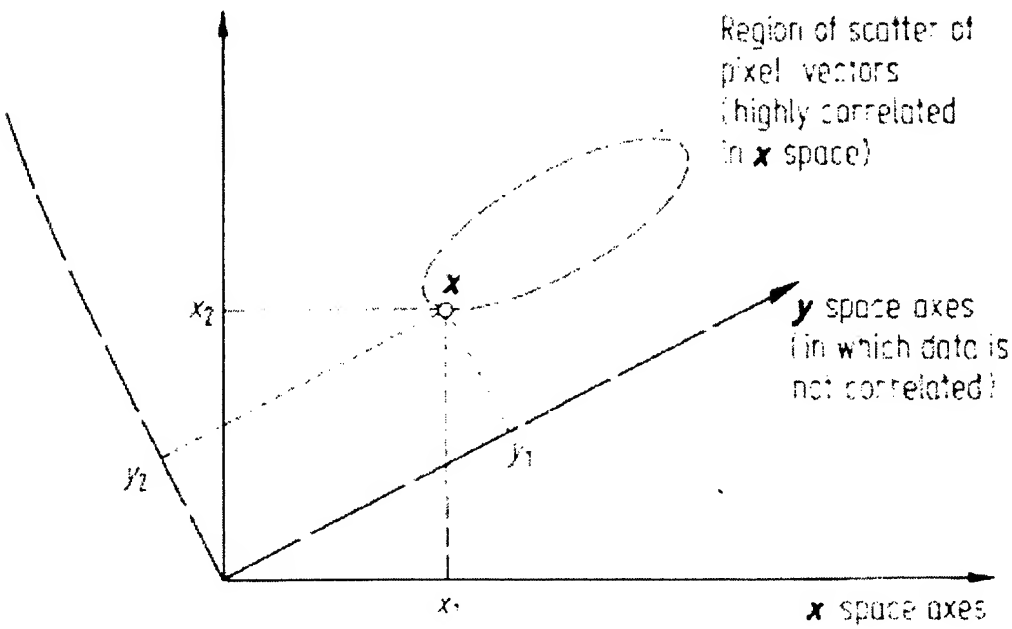

Fig. 4.3 Illustration of a modified co-ordinate system in which the pixel vectors have uncorrelated components (From Richards, 1999)

Mathematically, the principal components transformation, also known as Karhunen-Loeve or the Hotelling transform, is an exercise in linear algebra. The operation transforms the N bands of hyperspectral data into a set of uncorrelated principal component bands. Each of

these bands is a linear combination of the original bands. (Mather, 1999) The first principal component maximizes the variance of the original data, while the subsequent bands each maximize the remaining variance in projections that are perpendicular to the first dimensions. (Collins, 1996)

By viewing each pixel point as a vector, the transformation rotation can be arrived at more stringently. If in the new coordinate system the vectors are denoted as $\boldsymbol{y}$, than a linear transformation operation $\mathbf{G}$ of the original coordinates $\boldsymbol{x}$ is desired, such that:

$$\boldsymbol{y}=\mathbf{G}\boldsymbol{x} \quad (4\text{-}1)$$

where it is assumed that the covariance matrix of the pixel data in $\boldsymbol{y}$ space is diagonal. The covariance matrix in $\boldsymbol{y}$ space, $\sum_y$, can be identified as the diagonal matrix of eigenvalues of the covariance matrix in $\boldsymbol{x}$ space. (Richards, 1999)

$$\sum_y = \begin{bmatrix} \lambda_1 & 0 & & \\ 0 & \lambda_2 & & \\ & & \ddots & \\ & & & \lambda_N \end{bmatrix} \quad (4\text{-}2)$$

N is the dimensionality of the data. Since $\sum_y$ is by definition a diagonal covariance matrix, its elements are the variances of the pixel data in the transformed coordinates. As previously noted, $\lambda_1 > \lambda_2 > \cdots > \lambda_N$, so the values are ordered in decreasing variance. Because the maximum variance is in the direction of the first component, most of the information is contained in it, with decreasing amounts of information in the following principal components. The most obvious illustration of this is the higher degree of contrast in the first component compared to the

second and lesser components, as seen in figures 4.4 (a-d). These figures were created from a standard data set provided in ENVI. The data are from AVIRIS, and are a spectral subset from 1.99 to 2.48 μ. The scene is the infamous Cuprite, Nevada area.

Fig. 4.4 (a) Band One of sample PC Rotation

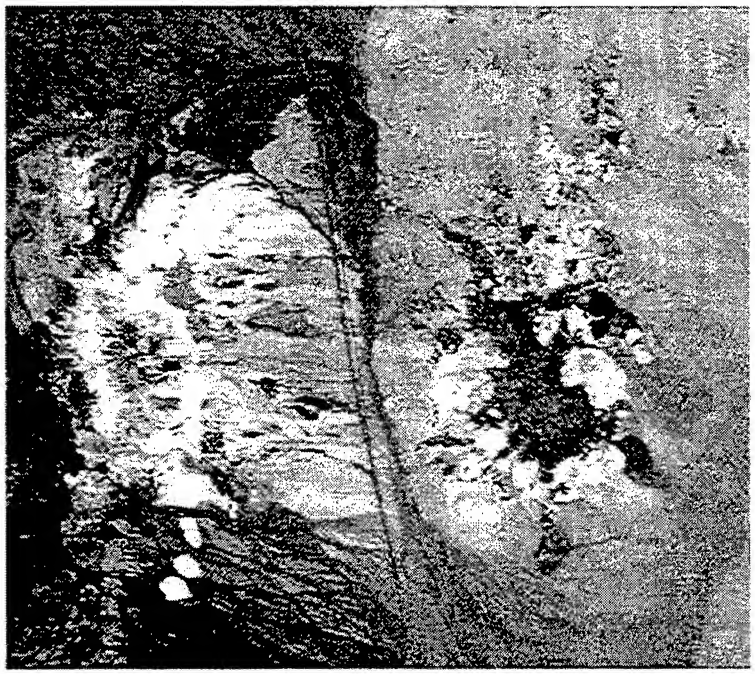

Fig. 4.4 (b) Band Three of sample PC Rotation

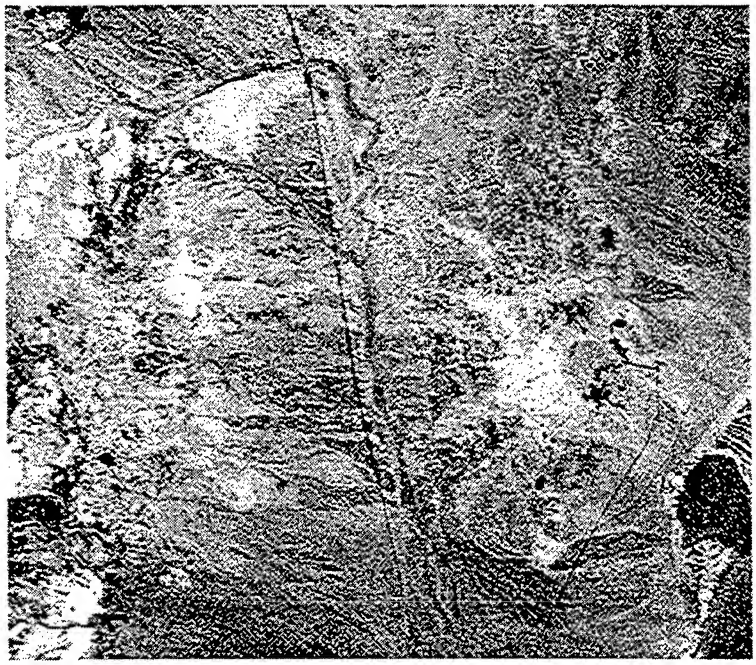

Fig. 4.4 (c) Band Six of sample PC Rotation

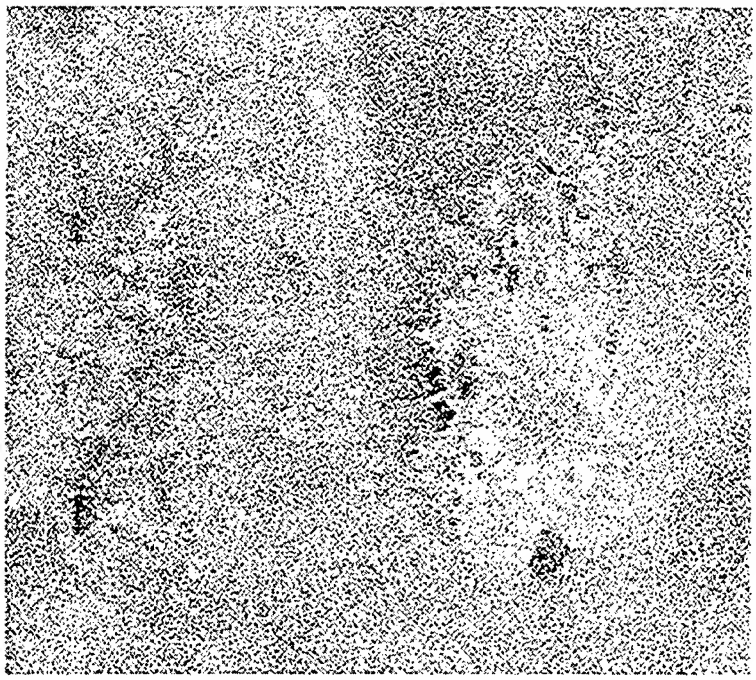

Fig. 4.4 (d) Band Nine of sample PC Rotation

The Principal Components Transformation provides early insight into complex data sets, but rarely is used to discriminate target elements. Subsequent classification techniques must be applied, many of which depend on the reduced dimensionality of the data in PC-space.

C. SUPERVISED CLASSIFICATION TECHNIQUES

Supervised classification relies on a variety of algorithms to determine the types of materials present in a scene. It is referred to as supervised because the user predetermines spectra or regions of interest from the scene, and the algorithm uses this information to classify the rest of the scene.

The essential steps to supervised classification techniques are:

1. Decide upon the materials present in the scene that will be used by the algorithm to classify the scene, such as water, sand, etc.

2. Select representative pixels from each of these material subsets. These pixels form the training data. It must be recognized that the number of training pixels for a given spectra must be equal to or greater than the total number of spectra chosen in the scene.

3. Use the training data to estimate the parameters of the classifier algorithm. The set of parameters for a given class is sometimes called the *signature* of the class.

4. Using the classifier, classify each pixel in the scene into one of the desired types.

5. Create summaries or class maps which summarize the results of the classification.

1. Parallelepiped Classification

The parallelepiped classifier is very simple in that the classifier is trained by inspecting scatter plots of the individual spectral components in the training data. As shown in figure 4.5, a pixel will be characterized as containing a certain material if it is bounded by one of the parallelepipeds.

For each of the classes specified, the user will specify a range expressed in terms of a number of standard deviations on either side of the mean of each feature. This allows an estimation of the position of the boundaries of the parallelepipeds. (Maher, 1999)

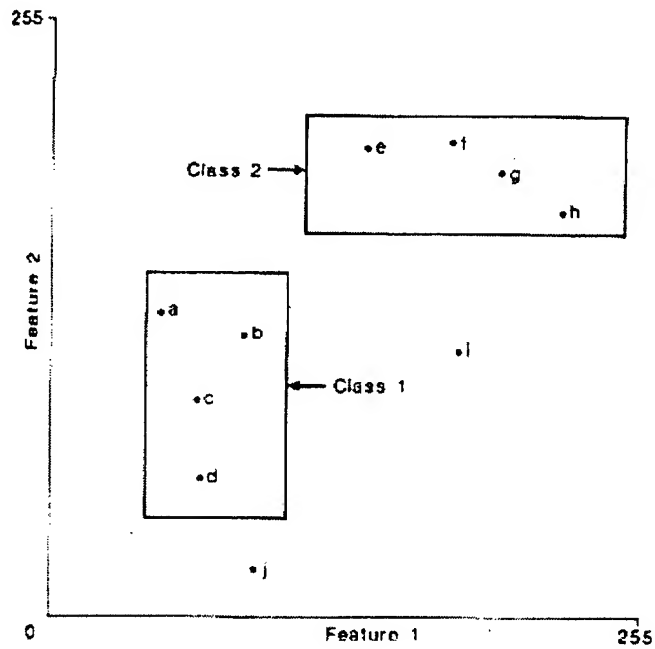

Fig. 4.5 Parallelepiped Classifier in Two Dimensions. Points Bounded by Parallelepipeds are Classified as Belonging to the Respective Classes, Points *i, j* are Unclassified. (From Mather, 1999)

Unfortunately, because of its simplicity several drawbacks are apparent. Gaps are possible between parallelepipeds as seen in figure 4.5. Pixels that fall outside of these regions will not be classified. Also, as seen in figure 4.6, correlated data may cause an overlap, as the sides of the parallelepipeds are parallel to the spectral axes. Thus some pixels will not be separated. (Richards, 1999)

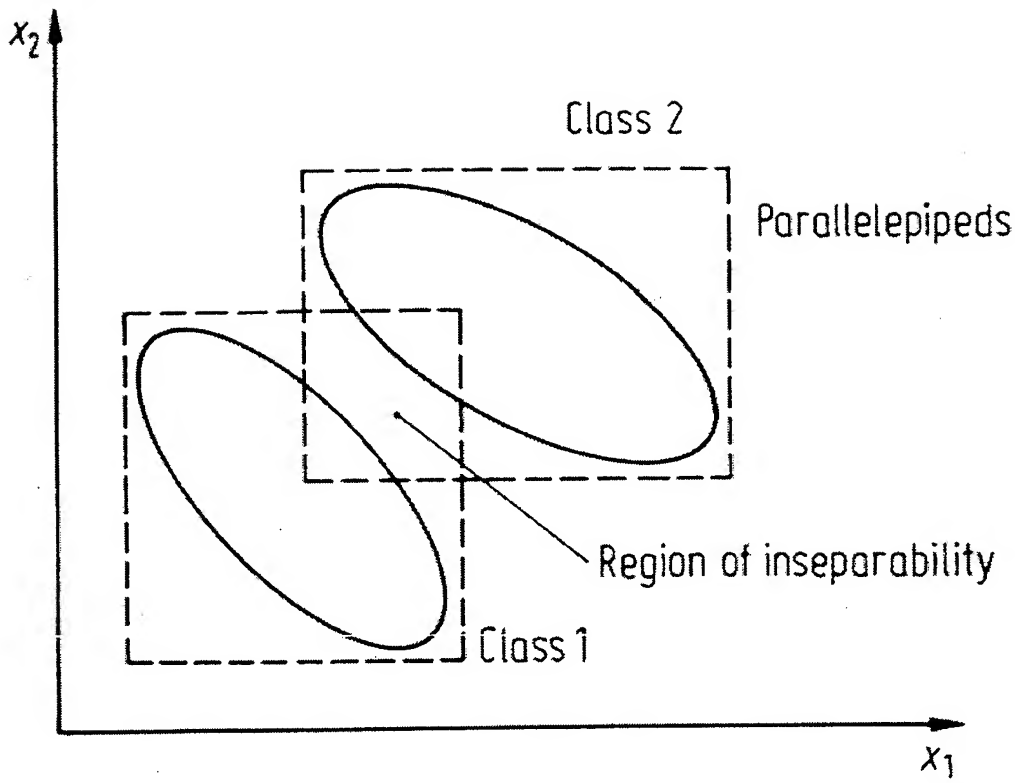

Fig. 4.6 Parallelepiped Classification of Correlated Data Showing Regions of Inseparability (From Richards, 1999)

2. Maximum Likelihood Classification

Maximum likelihood classification is the most common supervised classification method used. (Richards, 1999) The premise of this algorithm is that each pixel has a certain probability to be a given material, as defined by the material subsets chosen by the user. The material that the pixel has the highest probability to be is selected, and the pixel is classified as being that material.

$$x \in \omega_i \text{ if } p(\omega_i|x) > p(\omega_j|x) \text{ for all } j \neq i \quad (4\text{-}3)$$

Unfortunately, the probability that a pixel is a certain material is unknown. However, if enough training data is available, a probability distribution may be estimated that describes the chances of finding a pixel from material ω_i at the position x. This distribution will be denoted as $p(x|\omega_i)$. There are as many $p(x|\omega_i)$ as there are material types as defined by the user.

The desired $p(\omega_i|x)$ and the available $p(x|\omega_i)$ are related by Bayes' theorem. (Devore, 1995)

$$p(\omega_i|x) = \frac{p(x|\omega_i)\,p(\omega_i)}{p(x)} \quad (4\text{-}4)$$

In this, $p(\omega_i)$ is the probability that material ω_i occurs in the data set, and $p(x)$ is the probability of finding a pixel from *any* class at location x. The $p(\omega_i)$ are referred to as *a priori* since they are the probabilities from which the material composition could be guessed before classification.

Applying Bayes' theorem to equation 4-3 it can be seen that the classification rule is now:

$$x \in \omega_i \text{ if } p(x|\omega_i)\,p(\omega_i) > p(x|\omega_j)\,\mathrm{p}(\omega_j) \text{ for all } j \neq i \quad (4\text{-}5)$$

where $p(x)$ has been removed because it is common to both sides of the inequality. The classification rule is more acceptable in this form because the probabilities are known or can be inferred from the image. Further, one can define the function

$$\begin{aligned} g_i(x) &= \ln\left[p(x|\omega_i)\,p(\omega_i)\right] \\ &= \ln p(x|\omega_i) + \ln p(\omega_i) \end{aligned} \quad (4\text{-}6)$$

where ln is the natural logarithm, so that the classification rule becomes

$$x \in \omega_i \text{ if } g_i(x) > g_j(x) \text{ for all } j \neq i \quad (4\text{-}7)$$

where the $g_i(x)$ are now referred to as *discriminant functions*. (Richards, 1999) By assuming that the probability distributions for the target classes are normal, the discriminant function is further simplified for use.

The user may set threshold probabilities on the classification process, meaning that for a given pixel, if the largest probability that it is a certain target material is below a threshold value, the pixel remains unclassified. This will do away with situations illustrated in figure 4.7 a, b where the algorithm may classify a pixel incorrectly due to indeterminate probabilities. (Mather, 1999)

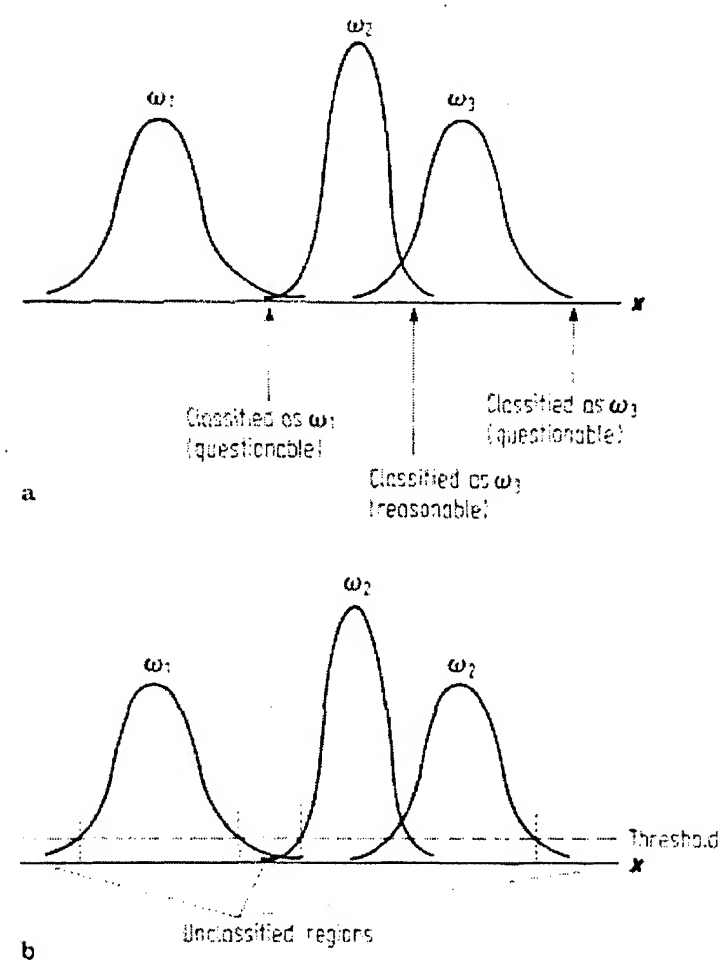

Fig. 4.7 a. Illustration of Poor Classification for Patterns Lying Near the Tails of the Distribution Functions of all Spectral Classes; b Use of a threshold to Remove Poor Classification (From Richards, 1999)

3. Minimum Distance Classification

The minimum distance classifier, or more correctly, the minimum distance to class means classifier, groups pixels by their distance from the various class means. For a given pixel, the distance between it and the mean of the various spectral classes is calculated. The material whose mean is closest to the target pixel determines the material of the pixel.

Useful because of its speed, minimum distance will classify all pixels in a scene. Also, the minimum distance algorithm can be used when a large number of training pixels are not available for each class. Other classifiers such as the maximum likelihood classification algorithm require a certain number of training pixels per class. (Richards, 1999)

4. Mahalanobis Distance

The Mahalanobis Distance algorithm is very similar to the maximum likelihood classifier. It has elements of the minimum distance classifier, but the Mahalanobis distance classifier is a direction sensitive algorithm that uses statistics for each class. Essentially, it is the maximum likelihood classifier with all class variance assumed to be equal. Because of this simplification, it is a faster algorithm than the maximum likelihood classifier. (Richards, 1999)

5. Spectral Angle Mapper

The spectral angle mapper (SAM) allows mapping of the spectral similarity of spectra from a HSI data set to reference spectra. The method assumes the data has been reduced to reflectance spectra, with dark current and path radiance removed. (Kruse, 1993) The algorithm classifies pixels in the target scene according to the angle between the scene spectra and the reference spectra, viewing the spectra as vectors in N-dimensional space, with N as the number of spectral bands in the scene.

Considering the simplified case of a two-band data set represented as a two-dimensional plot (figure 4.8). The lines connecting these two points and the origin contain all

possible positions for that material, equivalent to the range in digital number for that material in the scene. The angle between the vectors is the same regardless of their length. The SAM algorithm generalizes this concept to N-dimensional space.

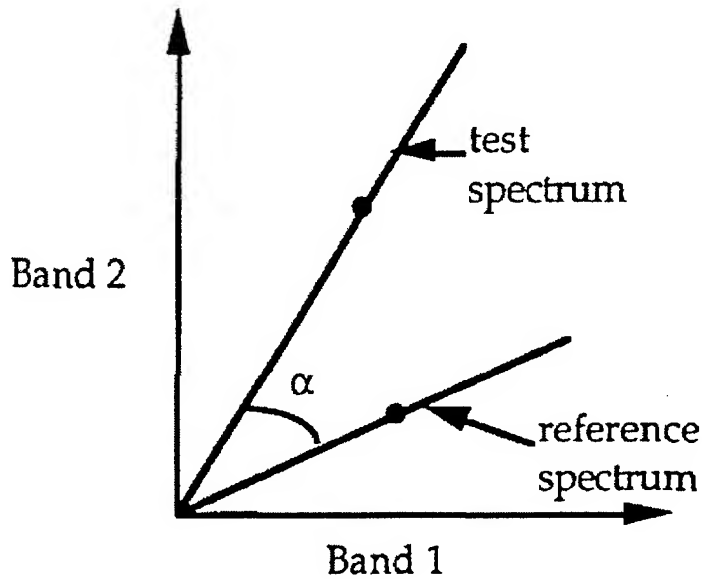

Fig. 4.8 Illustration of Spectral Angle Between Reference and Test Spectra (From Kruse, 1993)

The SAM determines the similarity of a given pixel spectra to a reference spectra by applying the following:

$$\cos^{-1}\left(\frac{\overline{t \cdot r}}{\|\overline{t}\| \cdot \|\overline{r}\|}\right) \quad (4\text{-}8)$$

which can also be represented as:

$$\cos^{-1}\left(\frac{\sum_{i=1}^{N} t_i r_i}{\left(\sum_{i=1}^{N} t_i^2\right)^{1/2}\left(\sum_{i=1}^{N} r_i^2\right)^{1/2}}\right) \quad (4\text{-}9)$$

where N = number of bands.

Because the angle between the vectors is insensitive to the length of the vectors, this algorithm is unaffected by gain factors, such as brightness or topography. This allows comparison between library spectra and the spectra of target pixels even with incomplete knowledge of the illumination characteristics of the target pixel spectra. (Kruse, 1993)

The user can specify a threshold angle to prevent improbable classification of target pixels. Much like user-specified variables in other supervised algorithms, if a target spectrum falls outside this threshold angle, the target will not be classified as the material. If the target pixel falls outside the threshold angle of *all* materials, then the pixel will remain unclassified.

6. Binary Encoding

Binary spectral encoding algorithms are among the earliest attempts to deal with the incredible amount of information in HSI. (The following description of the algorithm comes from Mazer, 1988). To compare the pixels in a scene with training spectra, the algorithm converts each pixel to a vector of dimension N, the number of bands in the detector,

$$\overline{\chi_{ij}} = \left[\chi_{ij}(1), \chi_{ij}(2), \cdots, \chi_{ij}(N)\right]^T \quad (4\text{-}10)$$

where the indices (i, j) refer to the spatial location of the pixel in the scene. Defining the spectral mean of pixel (i, j) as

$$\mu_{ij} = \left[\frac{1}{N}\right]\sum_{l=1}^{N} \chi_{ij}(l) \quad (4\text{-}11),$$

one can then form an N-bit binary code vector $\overline{Y}_{ij}{}^{a}$ by subtracting the mean from each pixel vector

$$\overline{Y}_{ij}{}^{a} = H\left\{\overline{\chi_{ij}} - \mu_{ij}\right\} \quad (4\text{-}12)$$

where $H(u)$ is the unit step operator defined by

$$H(u) = \begin{cases} 1, & u \geq 0 \\ 0, & u < 0 \end{cases} \quad (4\text{-}13)$$

The vector constructed is a binary representation of the spectral amplitude. Combined with a similar N-bit vector, $\overline{U}_{ij}{}^{b}$ (constructed from the local slope at each measured wavelength by the determination of the slope being positive or negative),

$$Y_{ij}{}^{b}(l) = \begin{cases} 1, & \left[\chi_{ij}(l+1) - \chi_{ij}(l-1)\right] \geq 0, \\ 0, & \left[\chi_{ij}(l+1) - \chi_{ij}(l-1)\right] < 0, \end{cases} \quad l = 1,2,\ldots,N \quad (4\text{-}14)$$

the two vectors form a 2N-bit code vector $\overline{Y_{ij}}$, which is the binary code word that represents the spectrum of pixel (i, j). The similarity measure used to determine the pixel is the Hamming distance:

$$D_h\left(\overline{Y_{ij}}, \overline{Y_{mn}}\right) = \sum_{l=1}^{2N} Y_{ij}(l)(XOR)Y_{\min}(l) \quad (4\text{-}15)$$

which is seen as just a 2N sum of bit-wise exclusive-or operations. Since perfect matches are exceedingly rare with real data, allowance for natural variability is made by specifying a threshold distance of acceptance, $\overline{d}$ such that

$$\overrightarrow{Y_{ij}} \equiv \overrightarrow{Y_{mn}} \quad \text{if } D_h \leq \overline{d} \qquad (4\text{-}16)$$

meaning that if the calculated Hamming distance is below the threshold value, then the pixel under scrutiny is of the material being compared to it. When multiple training spectra are used, the minimum distance determines the identity of the material. (Mazer, 1988)

7. Linear Spectral Unmixing

In the linear mixing model all observed spectra are postulated to be linear combinations of a set of basic spectra. The basic spectra, or endmember spectra, represent the spectrum that would be recorded for pure pixels. Mixed spectra are modeled as weighted linear combinations of these basic spectra. The weighting coefficients correspond to the apparent fractional surface coverage of that endmember in the scene. These coefficients may sum to one at each pixel in a constrained solution, or the user may elect to perform an unconstrained analysis, meaning negative coefficients are not barred. Spectral unmixing tries to differentiate the endmembers by inverting this procedure. One interesting note is that the number of endmembers must be less than the number of spectral bands. This allows a typical HSI detector with bands that number in the hundreds to be able to differentiate a similar number of endmembers!

ENVI performs Linear Spectral Unmixing but the user must have some prior knowledge of the scene. Training spectra are required for the algorithm to run.

8. Matched Filtering and Mixture Tuned Matched Filtering™

Matched filtering performs a partial unmixing to find the abundances of endmembers defined by the user from training spectra. It allows determination of the amount of a material in a scene with just the knowledge of that target spectra. In other words, regardless of the other endmembers present, the algorithm can 'look' for the desired endmember.

The operation of the matched filter algorithm reduces each pixel to a scalar that is a measure of the presence of the spectrum of interest. The end result is to turn the hyperspectral data cube into a single image where pixels with high intensity indicate the presence of the desired signature. The resultant image can then be thresholded and fed into a binary type classification algorithm to maximize the probability of detecting the signature of interest. (Harsanyi, 1994) This operation applies just as effectively to an operation where several spectra are of interest.

ENVI also provides an extension of the classic Matched Filter, the Mixture Tuned Matched Filter (MTMF™). It performs a match filter but also adds a measure of 'Infeasibility' to the results. This is supposed to reduce the number of false positives that may arise from a conventional matched filtering. Pixels with a high infeasibility will likely be matched filter false positives.

9. Spectral Feature Fitting™

Spectral Feature Fitting (SFF™) is an absorption feature based methodology for comparing the fit of image spectra to selected reference spectra using a least-squares technique. After a continuum removal is performed on both the scene spectrum and the training spectra, the two spectra are compared at each selected wavelength in a least squares sense and the root mean square error is determined for each scene spectrum. (Crowley, 1992)

D. UNSUPERVISED CLASSIFICATION TECHNIQUES

Unsupervised classification differs from supervised in that the algorithm does not depend on inputs of reference spectra from the user. While this may offer the advantage of not poring over data and establishing regions of interest and deriving training spectra, it does not allow the user to bring in information about the scene that may be useful.

The K-means and ISODATA algorithms have been widely used as unsupervised training techniques. (Hung, 1992)

1. K-means

K-means clustering is a commonly used technique to segment large image regions into specific objects or areas of interest. (Chai, 1999) The implemented algorithm takes as input the data-fused image to be analyzed and the number of clusters to be constructed (K). First, all possible pixel clusters in the image are identified according to a particular threshold metric. All

pixels that satisfy the threshold condition are grouped into M clusters based on a connectivity criterion.

Once the centroids for the M (M>K) clusters are determined, the algorithm maps these clusters into K new clusters. To do this, the algorithm chooses K clusters randomly out of the M original, and maps the remaining M-K clusters into these. The centroids of these K clusters are denoted as seeds. After the remaining clusters are mapped, the centroid of each of the newly expanded clusters is recalculated. This newly recalculated centroid replaces the old as one of the K seeds. The algorithm continues until no centroid changes cluster. At the end, there will be K clusters that will hold the original M clusters. Each of the K clusters will have a specific centroid calculated using all internal pixels. Of important note is that the clusters generated will depend on the choice of seed points. (Chai, 1999) Each cluster is then classified as an individual endmember.

2. ISODATA

The ISODATA classifier, while considered by ENVI to be an unsupervised classification algorithm, is more accurately a hybrid of supervised and unsupervised techniques. As pointed out by (Campbell, 1996), it can be considered a variation of the minimum distance method, as described earlier.

ISODATA starts with the training data selected as previously described, and these data can be envisioned as clusters in a multidimensional space. All unassigned pixels are then assigned to the nearest cluster centroid. Much as in K-means, the cluster centroids are then

recalculated with the new pixels. The process of allocating pixels to the closest centroid is repeated if the centroid changes in position. This continues until there is no change, or only a very small change, in class centroids from one iteration to the next. (Campbell, 1996)

The main difference between K-means and ISODATA is ISODATA requires entry of training data by the user. (Tou, 1974) Because of this, ISODATA does not have the susceptibility of the K-means algorithm to false local means because the algorithm is very dependent on initial seeds.

THIS PAGE INTENTIONALLY LEFT BLANK

V. SPECTRAL ANALYSIS

Data was collected on April 29, 2000 at Fort A.P. Hill in Virginia. The NVIS detector was utilized in AP2K, an exercise performed at A.P. Hill from April 24-May 5. For this exercise, a variety of targets were deployed in the exercise area, and a variety of sensors were flown over the targets. Ground truthing of the various targets was performed, and spectral calibration panels were deployed to allow faithful calibration to reflectance of the data. For this data set, NVIS was flown in NVL's Twin Otter aircraft at 3000 ft., giving a resolution of 1 meter.

The figures that will be described in this chapter that are designated figure B.X are all presented in Appendix B.

A. RADIANCE TO REFLECTANCE CONVERSION

The data as obtained from NVL was in terms of radiance at the sensor (figure B.1). NVL had previously converted the raw data from at-sensor Digital Number (DN) to at sensor radiance by use of its Data Processing software.

As discussed in Chapter II, radiance measures the Sun's energy incident onto a surface. Because of this solar dependence, variations in illumination alter the signature of the surface. To remove the effect of the Sun, a conversion to reflectance is performed. This gives spectra that are dependent on the material, not the illumination of the Sun (of course without illumination reflectance is undefined.)

As described before, in this thesis two methods for conversion from radiance to reflectance were used. ELM was used to compare all the various classification and mapping algorithms.

Ground truth reflectance for the calibration panels was provided by NVL (figure 5.1) and was converted into a spectral library. The panel spectra were obtained directly from the data set and converted into another spectral library (figure 5.2). These two libraries were used by ENVI to adjust the entire data set from radiance to reflectance. The calibration coefficients are illustrated in figure 5.3.

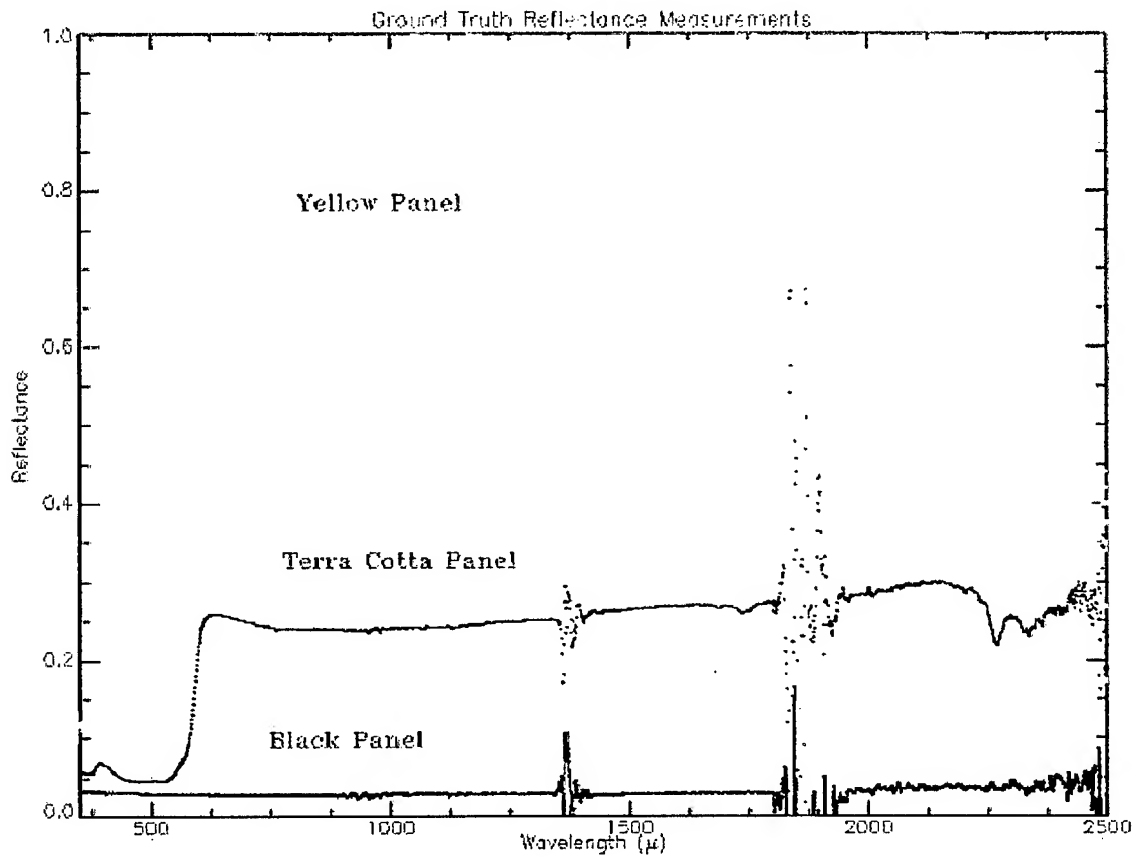

Fig. 5.1 Panel Ground Truth Reflectance

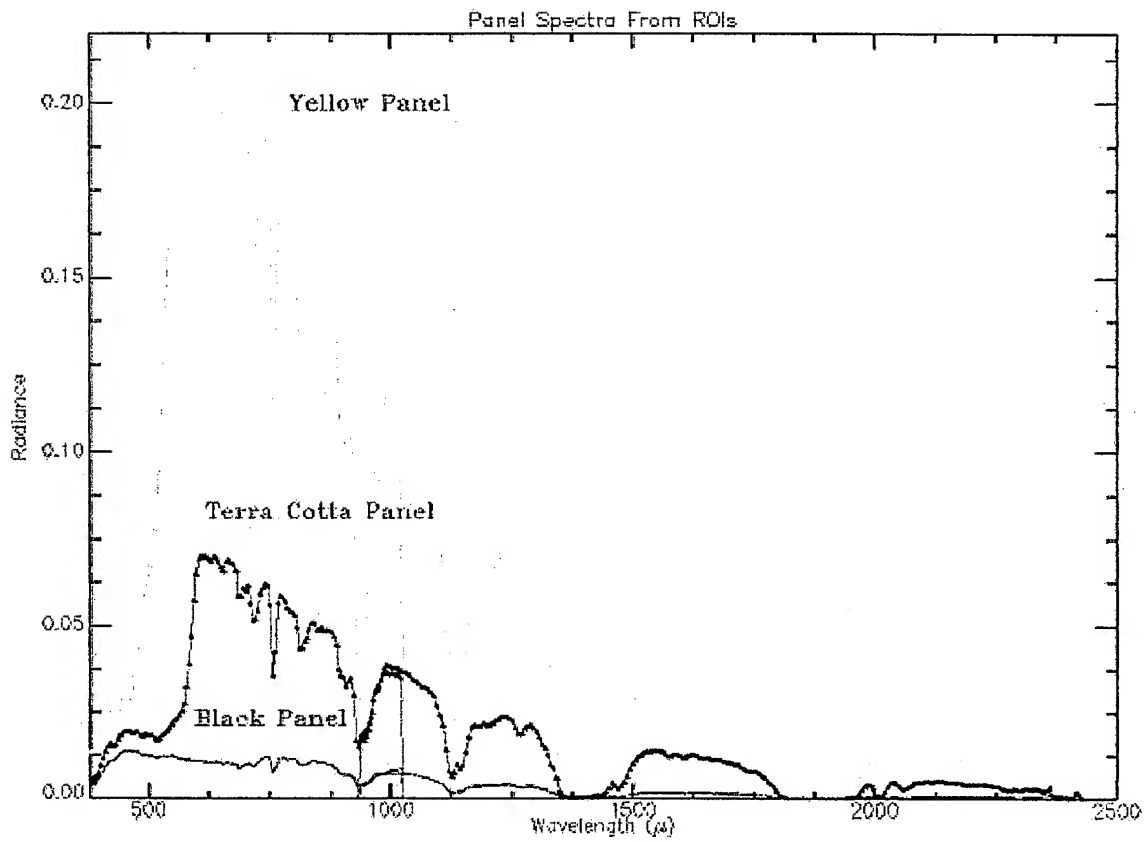

Fig 5.2 Panel Spectra from ROI's

To compare against ELM, an EISC calibration was performed and was demonstrated with one of the classification algorithms (SAM). This allowed a comparison between the two calibration processes to ascertain if these processes create any sort of effect on the classification output. The EISC coefficients are shown in figure 5.4.

Originally, a third calibration procedure was going to be included. This would have entailed using ATREM, a software package that can reduce radiance data to reflectance. However, ATREM requires the spectral resolution of the data to be no less than 8 nm

(ATREM, 1999). As NVIS spectral resolution is better than this, ATREM could not be used on the NVIS data.

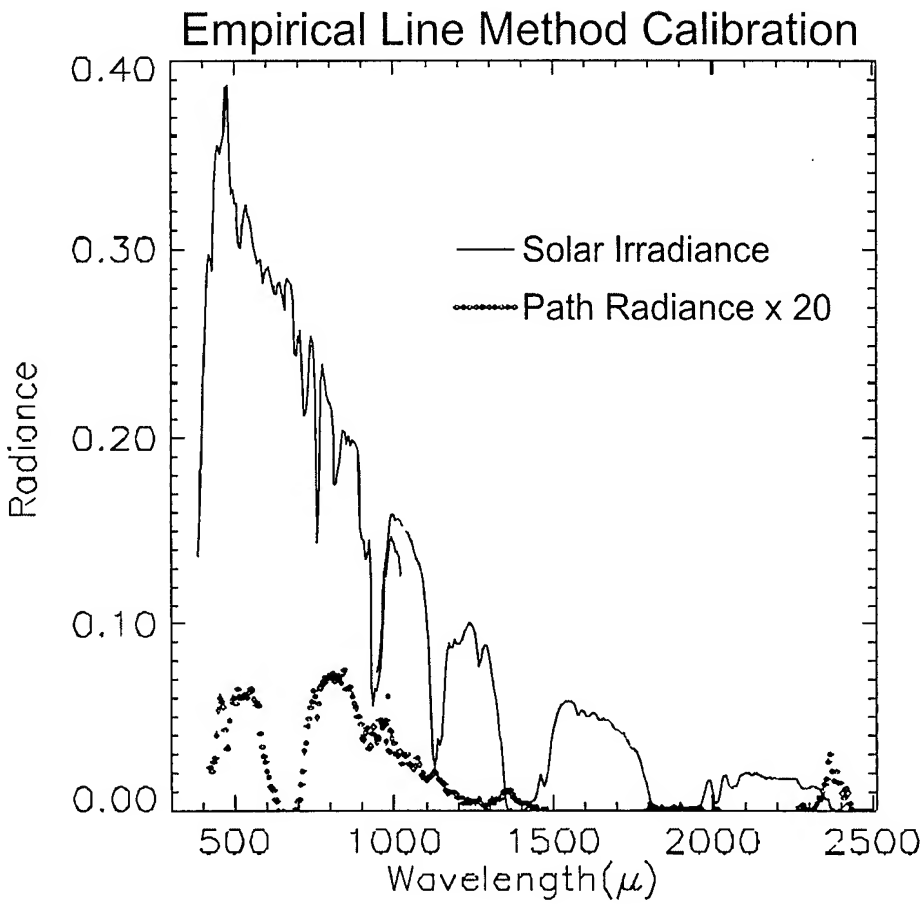

Fig. 5.3 Empirical Line Method Coefficients

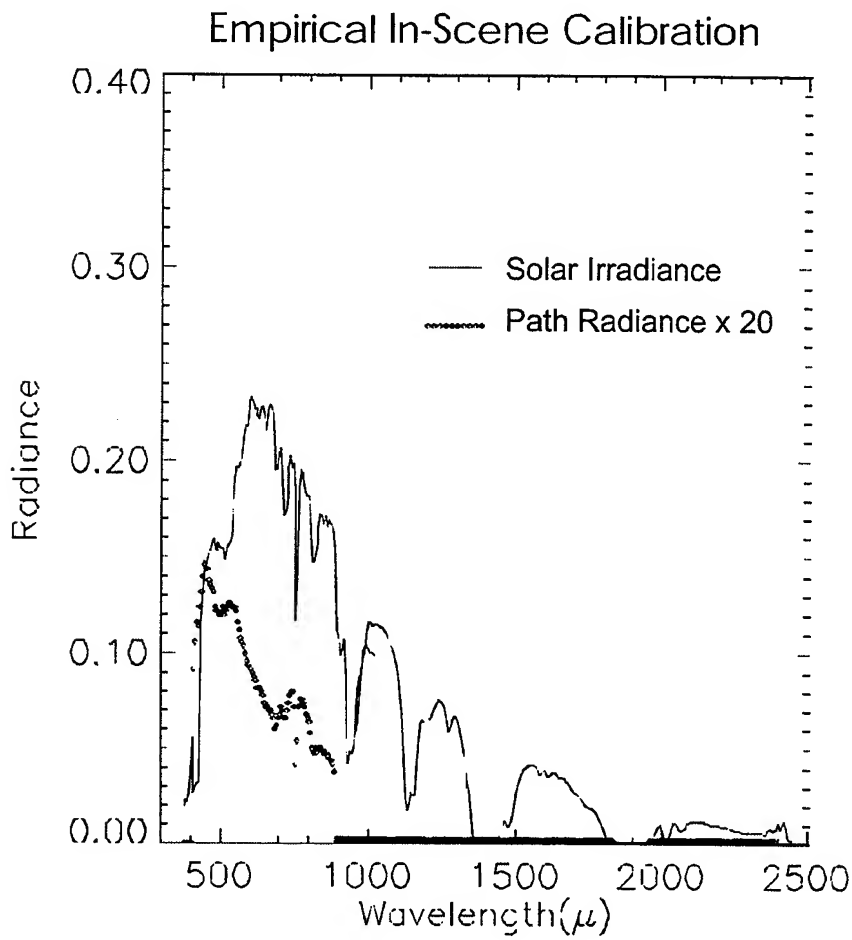

Fig. 5.4 Empirical In-Scene Calibration Coefficients

B. SPECTRAL AND SPATIAL SUBSETTING

To remove any detrimental effects from problems with portions of the data, the data was thoroughly inspected for edge effects and other problems. The edges of the data set (notably column one and columns 246-256) were essentially blank. To ensure that the edges of the data would not interfere with any of the classification algorithms, the edges were excluded from the data set. To remove the possible confusion in regions of the spectrum where

atmospheric absorption was high, the bands that fell into these regions were excluded (bands 200-208, 274-297, and 360-388.) This removed the spectral regions 1.36-1.41μ, 1.81-1.95μ, and 2.33-2.50μ respectively. Lastly, to remove the overlap inherent in the NVIS design between the SWIR and VNIR, bands 117-134 were removed, which removes the last bands of the VNIR (0.97-1.03μ) and the first bands of the SWIR (0.93-0.96μ) without leaving a gap in the spectrum observed.

C. DATA SET TRAINING

A Principal Components transformation into 30 bands was performed on the radiance data. This was done to allow working on a data set that has much lower dimensionality, thereby making operations on the data set easier to accomplish.

Regions of interest were created by use of ENVI's N-dimensional Visualizer, which attempts to picture the pixels of various bands as a rotated, two-dimensional image. This allows the user to separate out pixels as groups that share common spectral characteristics After selecting various classes and exporting them back to the main image, the user can determine that the individual classes selected in the Visualizer were various items in the scene, such as vegetation, water, etc.

The regions of interest initially created had a wide variety of materials included, as determined by the image. When the Visualizer was run, a fairly obvious clump of pixels was separate from the rest of the pixels in the group (figure 5.5). By exporting this new class back

to the original scene, it was determined to be a target in the trees near the water. This was later called target #1 (figure B.1).

Targets #2 and #3 (figure B.2) were located near the calibration panels and were not hidden in the trees in the scene. The Visualizer was used to separate the spectra of these targets from the surrounding area, by choosing a smaller region of interest that included these targets and the calibration panels. When this was done, the spectra of the two targets were distinct from the rest of the spectra in the region, and the new target spectra were exported to the original scene.

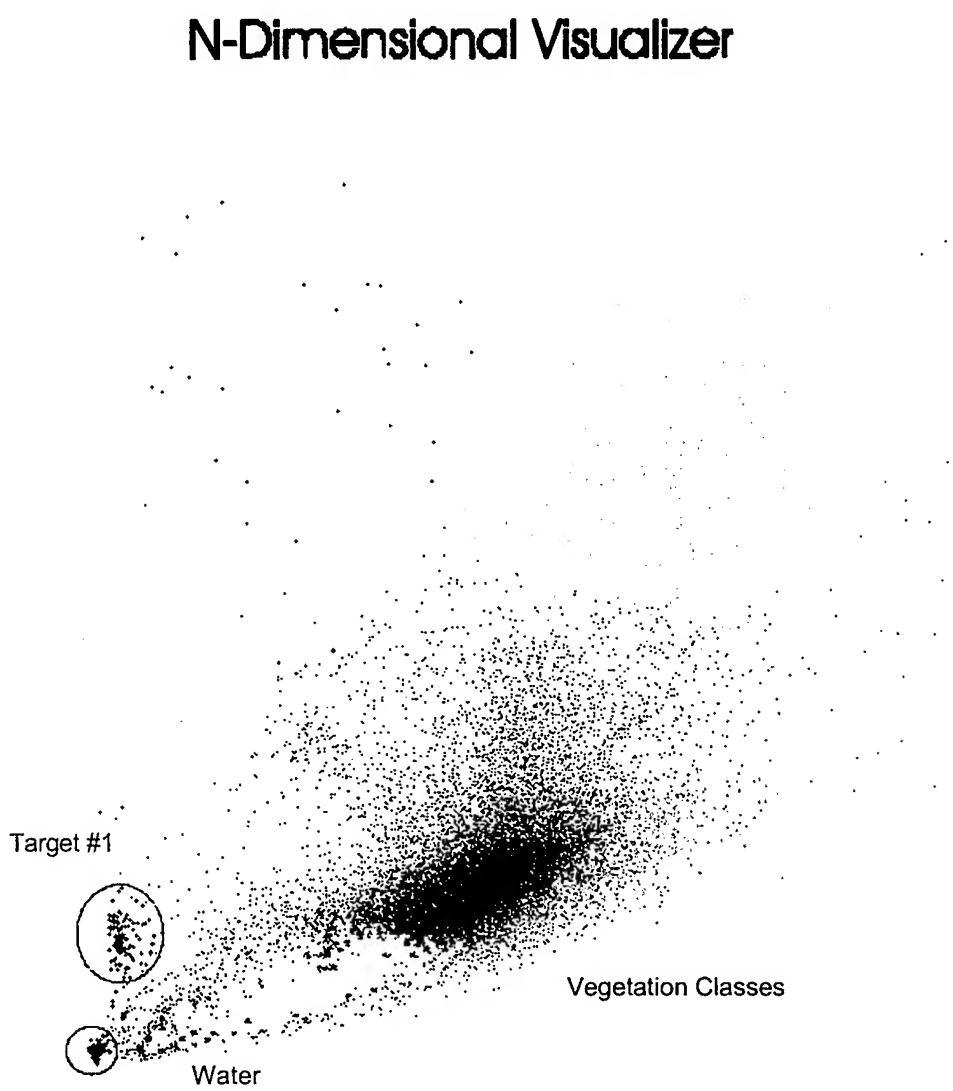

Fig. 5.5 Illustration of Using N-Dimensional Visualizer to Separate Spectral Classes

Target #4 was found by the user while looking at a false color image of the data set (figure B.1). As with targets #2 and #3, a small region of interest was created that included the new target as well as surrounding background materials. Again, the spectrum of the new target

was distinct from the spectra of nearby pixels, and this new target was exported back to the original scene.

The classes that were determined in this data set are shown in table 5.1.

	Classes	Color
1	Interesting target	Purple
2	Another Target	Orchid
3	Target near Panels	Sienna
4	Target near Water	Aquamarine
5	Black Panel	Black
6	Red Panel	Red
7	Yellow Panel	Yellow
8	Grass	Green
9	Dark Bushes	Chartreuse
10	Bright Trees	Magenta
11	Bright Trees2	Coral
12	Water	Blue
13	Road	Maroon
14	Dirty Water	Sea Green

Table 5.1 List of Training Classes

Once these classes were determined and quantified, they were used by the various supervised classification algorithms in ENVI to classify or map the data set.

A second classification image was created, using the first ten bands of the PC transform. This was done to allow the Maximum Likelihood and Mahalanobis distance algorithms to be performed. This was necessary for these algorithms because the number of training examples (pixels) must be more than the number of spectral bands in the data set. Given the limited

number of pixels on the targets, this ruled out the chance to use the full data set. The same regions of interest were imported into this ten-band set to perform the algorithms.

D. SUPERVISED CLASSIFICATION ALGORITHMS

1. Spectral Angle Mapper

a. Empirical Line Method

The Spectral Angle Mapper algorithm was applied to the ELM reflectance data. The angular separation allowed was varied from 0.1 radians to 0.5 radians. As can be seen from the images, SAM does a fairly good job of breaking out the obvious targets, such as the calibration panels. From figures B.2 and B.3, one can see the emergence of the vegetation classes and the calibration pixels, as well as the differentiation of the two water classes as the separation angle is opened from 0.1 radians to 0.2 radians. As an example, figure B.4 shows the red calibration panel rule image. As can be seen in the gray-scale figure, the panel pixels were classified with an angle of 0.05 radians.

However, from the rule images, the targets of interest are not well broken out, if at all, except for Target #1. As can be seen from its rule image (figure B.5), target #1 was easily recognizable and was well classified in the scene. Interestingly, the target required a separation angle of 0.4 before it was classified, but it was markedly different than the rest of the spectra in the scene. Target #2 was not classified at all (figure B.6). As can be seen in the figure, a large portion of the scene was classified as target #2. Target #3 was classified, but a portion of the background was also classified as target #3, however to a lesser extent (figure

B.7). Target #4 was not considered classified. While the target was classified, enough of the background was also included such that differentiation from background was not possible (figure B.8).

b. Empirical In-Scene Calibration

The spectral angle mapper was also performed on the EISC data, to function as a check to determine if the choice of radiance to reflectance calibration mattered on the classification of the targets.

The similarities between the mapping images of the ELM and EISC outputs are not surprising (figures B.9, B.10). One striking difference is the larger differentiation angle required to classify the same object. The water area is a prime example. In the ELM set, the water is well classified at 0.2 radians, whereas in the EISC data set, the water is not well classified until 0.5 radians.

Much as was found in the ELM data, a SAM performed on the EISC data broke out target #1 (figure B.11). Interestingly, the target again required a large angle (0.4 radians) of separation to be differentiated. Again, the target was drastically different from the rest of the scene.

Target #2 was confused with much of the background in the scene. This was precisely the result derived in the ELM data for target #2 (figure B.12).

Target #3 was differentiated from background (figure B.13). As was found in the ELM data, much of the background was classified as target #3, but the target itself required a much smaller angle to be differentiated.

Target #4 was again not differentiated from background. However, in the EISC case, very little of the background was mistakenly classified as target #4 (figure B.14)

2. Parallelepiped

The parallelepiped algorithm was performed on the ELM reflectance data. The algorithm allows the classes to be discriminated in terms of the width, measured in standard deviations, of an n-dimensional rectangle. As can be seen from figures B.15 and B.16, the mapping characteristics of this algorithm leave much to be desired. While the more obvious classes like the calibration panels as well as one of the more significant targets were mapped (target #1), the algorithm appeared confused by the majority of the background.

This algorithm showed a striking ability to classify target #1. As seen in the rule image for target #1 (figure B.17), this object's difference from the background makes it a fairly obvious non-background target, however, there does seem to be some confusion regarding nearby pixels in the water that are misclassified as target #1.

Much of the entire scene was classified as target #2. This is very apparent when looking at the rule image for target #2 (figure B.18). It is interesting that target #2 is actually well differentiated compared to the surrounding area, yet the algorithm classifies a large portion of the forest background as target #2.

Target #3 (figure B.19) was correctly classified by the algorithm. As seen in its rule image, the target is easily differentiated from the background.

Target #4 (figure B.20) was not differentiated against much of the background. To a lesser degree than target #2, a significant portion of the forest background was classified as target #4.

3. Binary Encoding

This method was the most successful at mapping vegetation while at the same time did a fair job of target discrimination from background. However, this algorithm was not as successful as the others in breaking out even the more obvious targets like the calibration panels at high levels of probability. As can be seen in figures B.21 and B.22, as the level of probability required increases, the obvious targets disappear from view, leaving just scattered vegetation and water.

Target #1 broke out at over a 90% degree of certainty (figure B.23). Much as the other algorithms, binary encoding did a fair job of differentiating this target from the background. However, as can be seen in figures B.24 and B.25, this algorithm had particular difficulty in separating targets #2 and #3. Target #2 was confused with the vast majority of the scene. As seen in the histogram in figure B.24, most of the pixels in the scene were classified as target #2 with at least a 90% degree of certainty.

Target #3 shows a similar result. However, as can be seen in its rule image, target #3 itself was classified to less certainty than much of the surrounding background.

Target #4 is not differentiable from background unless the histogram and enlarged picture of the target are checked (figure B.26). The histogram shows a sharp drop above 85% certainty, with a small number of pixels at 90%. When checking the image, it is apparent that the small number of pixels that are classified at 90% are associated with target #4.

4. Minimum Distance

The results for the minimum distance algorithm were very similar to the binary encoding. When forced to classify the entire scene, the algorithm looked like it provided accurate results (figures B.27, B.28). This algorithm was the most accurate in classifying the water as definitely having two distinct classifiable areas. However, when the individual rule images were observed, a very different portrayal of the scene was evident.

As before, target #1 stood out from the rest of the scene remarkably well (figure B.29). Also as noted, the water in the scene was characterized as having two distinct characters (denoted 'water' and 'dirty water' in the class list.) When the rule images for the other three targets of interest were observed, the images did not provide any indication of separation from background. Targets #2 and #3 were not recognizable from the background without prior knowledge of their existence (figures B.30, B.31). Because the targets are physically separated from the trees in the scene, it appears as if they are differentiated. However, it is made apparent by checking the gray scales and histograms for the two targets that if they were hidden in the trees, they would not be differentiated.

The same is true for Target #4 to a lesser extent. While the algorithm excluded much of the background, it did not show any distinction between the target and the small amount of background that was apparent in the image (figure B.30).

5. Mahalanobis Distance

As stated previously, this algorithm was performed on a 10 band PC rotation set of the original radiance data. The mapping images (figures B.33, B.34) show this algorithm was successful at breaking out the panels and the water. With regards to the four targets, however, the rule images must be observed because of the subtlety of the target differentiation is not apparent in the mapping images.

Target #1 was differentiated fairly well from the background (figure B.35). While it may be noted that a number of background pixels were also classified as this target, the difference between these few pixels and the target is large and noticeable.

More so than with many of the other algorithms, target #2 was differentiated from the rest of background. While fairly subtle, the target is nevertheless apparent (figure B.36).

Target #3 also was well differentiated (figure B.37), however not so obviously as target #1. While it was obvious from the figure that a significant portion of the scene was remarkably similar to target #3, the target itself was easily seen.

Target #4 was not differentiated from background (figure B.38). While the majority of the background was excluded, so much of the background was included in the rule diagram that the location of the target is not at all apparent.

6. Maximum Likelihood

As with Mahalanobis distance, this algorithm was performed on a 10 band Principal Component set of the radiance data. By noting the mapping images (figures B.39, B.40), one can immediately see that the two water classes and the panels are obvious to the viewer, as well as target #1. Consequently, it is not surprising that the algorithm broke out target #1 very well (figure B.41).

Targets #2 and #3 were not differentiated from background at all. As apparent from the rule images, #2 was confused with much of the grass in the scene (figure B.42). #3 on the other hand was confused with much of the road and grass in the scene (figure B.43). Unlike the other targets, the histograms for #2 and #3 exhibited the characteristics of a 'smile' in that while a large portion of the scene was given a likelihood of 0 (in a scale from 0 to 1), much of the rest of the scene was given a likelihood of 1.0.

Target #4 was relatively well broken out from the background of the scene (figure B.42). While some background pixels were classified as well, the contrast from the rest of the scene was sufficient to differentiate the class from the rest of the classified pixels.

7. Linear Spectral Unmixing

This algorithm adds a level of complexity to the results. Not only are rule images produced as output, but the algorithm also creates an error image, which can be used to judge how accurately a classification is made. The algorithm can be run with or without a unit sum

constraint. It was not apparent that there was a noticeable difference between the two by the author.

Looking at the error image (figure B.45) where large error is dark, it is apparent that the majority of the error exists on the boundaries between groups of vegetation, as well as around the water. With that in mind, it must be noted that for the individual rule images, if an image denotes a positive target classification, and this is coupled with a high error, than the classification is in doubt. In these cases, there were no apparent instances of a target being incorrectly classified, whereas three of the four targets were not differentiated from background.

Unlike the other algorithms, this algorithm was unsuccessful at differentiating target #1 from the background (figure B.46). As apparent in the rule image, the target blends in with the background completely. Target #2 was also inseparable from the background (figure B.47), in that there was no means to differentiate the target from the rest of the scene.

Target #3 was separated from the background very well (figure B.48). The contrast between the target and the rest of the scene was remarkable, and left no question as to the presence of the target.

The rule image for target #4 (figure B.49) was very similar to that of target #1, in that the target was completely indistinguishable from the rest of the scene.

8. Matched Filter

The Matched Filter outputs rules images that, as a function of brightness, denote pixels that the algorithm has classified as the target pixel. There is no indication of error as there is in MTMF™.

The Matched Filter broke out target #1 easily from the background (figure B.50). However, the algorithm classified a significant portion of the water's edge as well. Unfortunately, this casts doubt on the validity of the classification. Also, target #1 was broken out to varying degrees in all of the other three target rule images.

The algorithm differentiated target #2 (figure B.51). Unfortunately, when performing this classification, target #3 was also included in the classification, and target #1 to a much lesser extent. When actually performing the classification for target #3 (figure B.52), it was again well differentiated. Unfortunately, targets #1 and #3 were also broken out when classifying target #4 (figure B.53). As no amount of error is able to be determined, there is no justification as to whether a classification is correct or not, so the inclusion of target #3 in all of these other classifications brought much confusion to the results.

9. MTMF™

The MTMF™ algorithm output was very similar to the Matched Filter; however, it also includes a measure of 'infeasibility' to allow a means to differentiate between positive matches in a rule image. To generate the rule images, the classification images were divided by the

infeasibility. Therefore, if a pixel had a high probability and a low infeasibility, it would output a high MTMF^{TM} value.

Target #1 shows up very plainly in its rule image (figure B.54). When observing the infeasibility image it is also notable that except for a few other pixels (some of which belong to target #4) the pixels that are classified as target #1 are the only feasible pixels in the scene. This gives a good indication that the pixels classified as target #1 are actually target #1.

Targets #2 and #3 were also differentiated from background (figures B.55, B.56). Interestingly, a sort of sensor artifact is evident in the rule image for target #2 that was not plain in any of the other rule images. This can be seen as the line of feasible pixels that vertically intersects the image above target #2.

Target #4 gave an interesting result that was not reproduced in the other algorithms. Target #4 was classified and deemed feasible, but target #1 was also included, reducing the effectiveness of this algorithm to differentiate target #4 (figure B.57). Also, the algorithm classified a number of pixels as target #4 in a shadowy region in the data set that it also described as having high feasibility. Whether this is a true false alarm or another target is not easily determined, as this detection did not evidence itself in the other algorithms.

10. Spectral Feature Fitting

Much like MTMF^{TM} and Linear Spectral Unmixing, SFF provides a rule image as well as a measure of error. As was done with the MTMF^{TM} algorithm, the rule image was divided

by the RMS error image to provide a better picture of what the algorithm considers to be classified as a target.

The algorithm again characterized target #1 quite easily (figure B.58). However, the other targets were all classified by lesser and varying degrees of success. The algorithm was completely unsuccessful at breaking out target #2 (figure B.59). So much background was included that even given the position of target #2, it is not possible to differentiate the target from all the background pixels.

Much like target #2, a large portion of the background was included in the classifier for target #3 (figure B.60). However in this case, the background actually shows as more of a definitive match due to its darker presentation. Target #4 was classified, but enough background pixels were included to introduce confusion in classification (figure B.61). However, due to the darkness of the classification image, the target was definitely broken out.

E. UNSUPERVISED MAPPING ALGORITHMS

While the proceeding algorithms attempted to classify the pixels in the scene according to training spectra, these algorithms broke the scene up into as many endmembers as the user specified.

For both algorithms, a varying number of endmembers were specified, meaning the algorithm attempted to find that many individual endmembers in the scene. This was done to explore the capabilities of the algorithms to differentiate the endmembers.

1. K-Means

The K-Means algorithm did not adequately differentiate the four targets of interest from the background. While the calibration panels were usually separated, the targets were misclassified, generally the same as water.

For the five-endmember case (figure B.62), as expected the scene was broken down into a combined shadow and water class and the four classes that covered the rest of the scene. Because the algorithm was so limited, it was of no real use to attempt to differentiate between the targets in the scene.

For the ten and sixteen endmember cases though (figures B.63, B.64), sufficient endmembers were available to break out some of the variation in the scene. However, due to the nature of the algorithm, even the calibration panels were classified as belonging to classes that from the picture were vegetation classes or water. The same was definitely true with the targets of interest. Interestingly, the most striking target, target #1, showed up as belonging to the water class from the mapping results. Because of these findings, it was not shown that the K-Means test is a useful one for distinguishing targets in this data set.

2. ISODATA

The results from the ISODATA algorithm were much the same as from the K-Means, which, owing to the similarity between the algorithms, is not surprising. For the 5-endmember scenario (figure B.65) there was not enough granularity available for the algorithm to differentiate any of the interesting targets.

While some of the targets were apparent in the ten and sixteen endmember results (figures B.66, B.67), without prior knowledge of the location of the targets, the inclusion of the targets in such classifications as a water or vegetation class would confuse the differentiation process. As can be seen in these results, target #1 again is classified the same as the water class, while the other targets are variants of vegetation classes.

As the results for both the K-Means and ISODATA are similar, it may be inferred that perhaps a non-supervised mode of classification is not sufficient to differentiate targets in a wooded, camouflaged environment. However, if the possible number of differentiable endmembers were increased, the required granularity may be achieved. ENVI allows more than sixteen endmembers to be differentiated. However, it only supports up to sixteen mapping colors. Consequently, if the algorithm was run to search for more than sixteen endmembers, a repetition of colors would result. This leads to confusing classification and a less meaningful image.

F. SUMMARY

The performance of the various algorithms in differentiating the four targets of interest is summarized in the following table (5.2).

	Target #1	Target #2	Target #3	Target #4
ELM				
SAM	Yes	No	Yes	No
Parallelepiped[1]	Yes	No	Yes	No
Binary Encoding[2]	Yes	No	No	Yes
Minimum Distance	Yes	No	No	No
Mahalanobis Distance	Yes	Yes	Yes	No
Maximum Likelihood	Yes	No	No	Yes
Linear Spectral Unmixing	No	No	Yes	No
Matched Filter[3, 4]	Yes[5]	No	Yes	No
MTMF™	Yes	Yes	Yes	No[6]
Spectral Feature Fitting	Yes	No	No	Yes
K-Means	No	No	No	No
ISODATA	No	No	No	No
EISC				
SAM	Yes	No	Yes	No

Yes = Target differentiated from background

No = Target not differentiated

Notes:

1 – Large portion of the scene was classified as Target #2
2 – Most successful at mapping vegetation
3 – Target #1 was classified in all four of the rule images
4 – Target #3 was classified in the rule images for target #2 and #4
5 – Portion of the water class was also classified as target #1
6 – Target #1 was also classified and considered feasible by the algorithm

Table 5.2 Summary of Algorithm Results

THIS PAGE INTENTIONALLY LEFT BLANK

VI. CONCLUSION

In this thesis a comparison of the classification algorithms provided by ENVI was performed. A data set collected by use of the Night Vision Imaging Spectrometer was analyzed. This also allowed a determination of the usefulness of NVIS to differentiate targets in a scene, specifically targets that are in varying degrees of concealment. The algorithms were performed on the data, and differences in the output of the algorithms were noted.

The main measure of performance that was observed was the ability of the algorithm to differentiate four targets of interest from the rest of the scene. While terrain categorization is also a performance parameter, no marked differences between the algorithms were observed. The algorithms all were able to distinguish the water from the differing types of vegetation. In fact, the varying types of trees and grass were also classified. However, due to the methods used in this thesis, the most useful object of this work is the ability of the algorithms contained within ENVI to differentiate targets from background.

As opposed to other work done in the field of HSI, no ground truth spectra were used to differentiate targets from background. Ground truth spectra were used only to perform a calibration from radiance to reflectance. Because ground truth spectra were not used to classify, this gives a more realistic real-world evaluation of these classification algorithms. If these algorithms were to be used to meet military needs, the capability to act without prior knowledge of the targets in the scene is vital.

The perfect classifier for military use would be the type that requires no input from the user. This would of course mean an unsupervised classification algorithm. Unfortunately these types of algorithms require a fairly large amount of computing power, as well as being lengthy in time. This is not conducive to a military use. Because of this, at the current stage of development, supervised classification algorithms are more appropriate for use. The downside to this is that some means to differentiate spectra, as was done in this thesis using ENVI's N-dimensional Visualizer, must be performed by the user. This is unfortunate in that any inaccuracies introduced by the user, such as poor spectral differentiation, will be carried forward by the algorithm, degrading its results.

In this thesis, the most successful algorithms in differentiating the four targets of interest were Mahalanobis Distance and the Mixture Tuned Match Filter™. Unfortunately, neither of these algorithms was able to classify all four of the targets of interest. Neither of the two algorithms was able to differentiate target #4. MTMF™ actually did classify target #4, but it also included target #1 in its classification, leading to confusion between the targets. With regards to truly differentiating target #4, only three algorithms were able to do this. They were Binary Encoding, Maximum Likelihood, and Spectral Feature Fitting.

MTMF™ was the best of the algorithms in differentiating the targets in this data set. While it could not classify target #4 without also including target #1, nevertheless target #4 was classified. This was not the case for Mahalanobis Distance.

NVIS has been shown to be useful in differentiating targets in a CCD setting, as well as performing TERCAT. Modern military operations require the type and quality of information

provided by NVIS, and it is hoped that further investigation of its properties will be performed. However, a more accurate algorithm or combination of algorithms must be discovered and applied to NVIS such that accurate, timely differentiation of targets from background can be performed, and this information disseminated to the user.

THIS PAGE INTENTIONALLY LEFT BLANK

APPENDIX A. NVIS LINE DRAWINGS

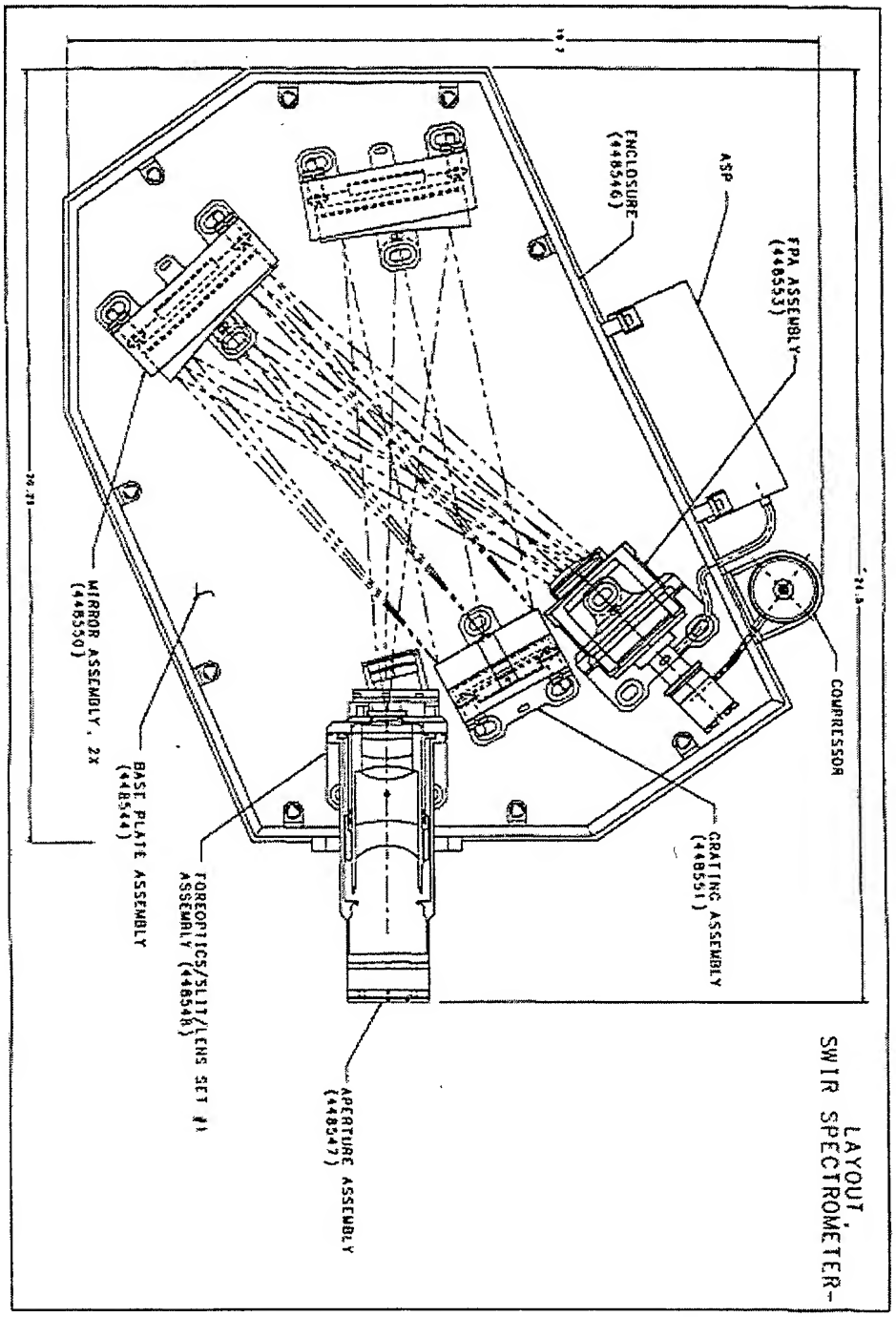

Fig. A.1 Layout of the SWIR Spectrometer (After Folkman, DeLong, 1996)

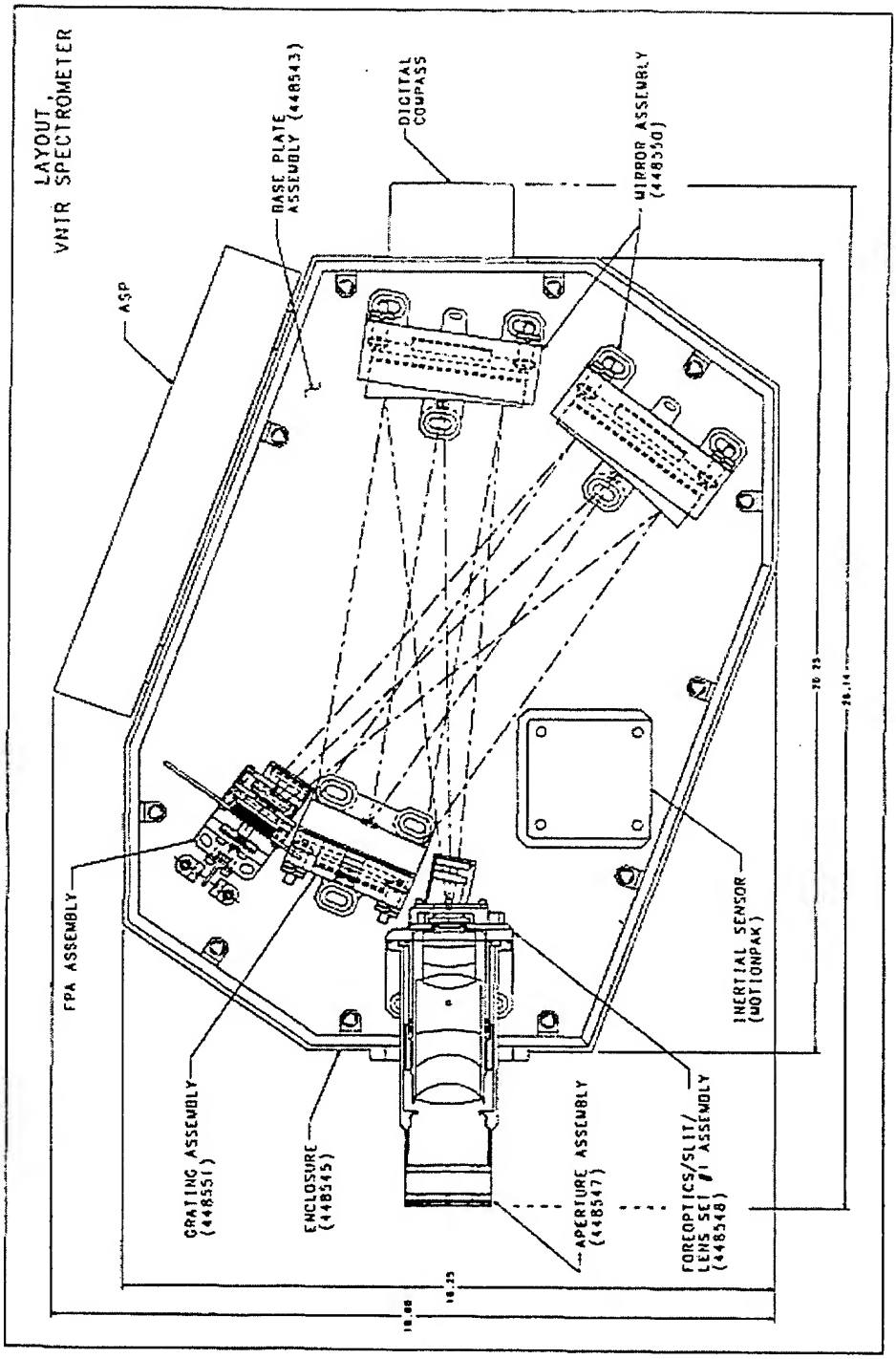

Fig. A.2 Layout of the VNIR Spectrometer (After Folkman, DeLong, 1996)

APPENDIX B. CLASSIFICATION IMAGES

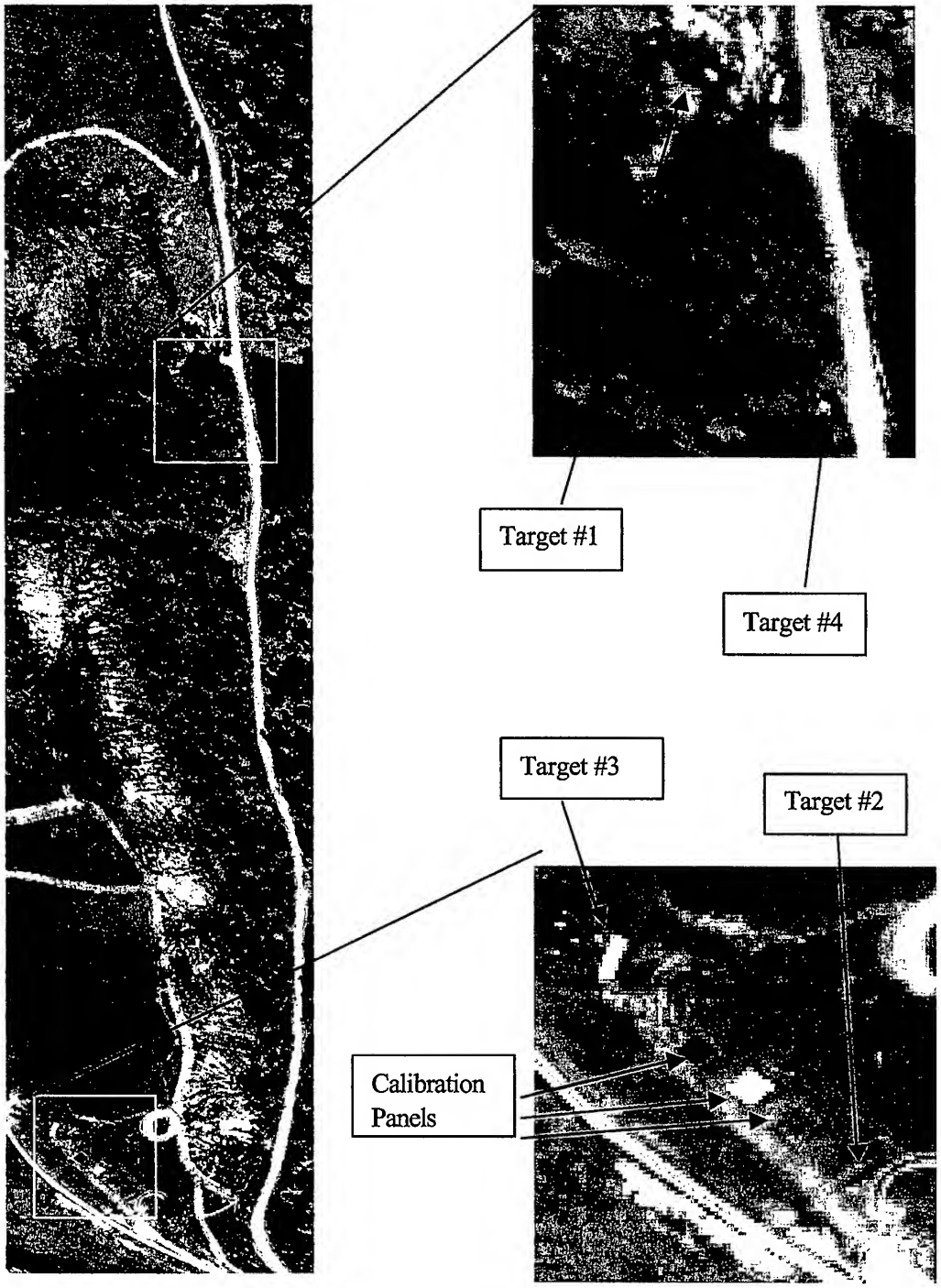

Fig. B.1 False Color Image of the Scene, Illustrating Targets of Interest

0.1 Radians

0.2 Radians

Fig. B.2 ELM SAM Mapping Output for 0.1 and 0.2 Radians

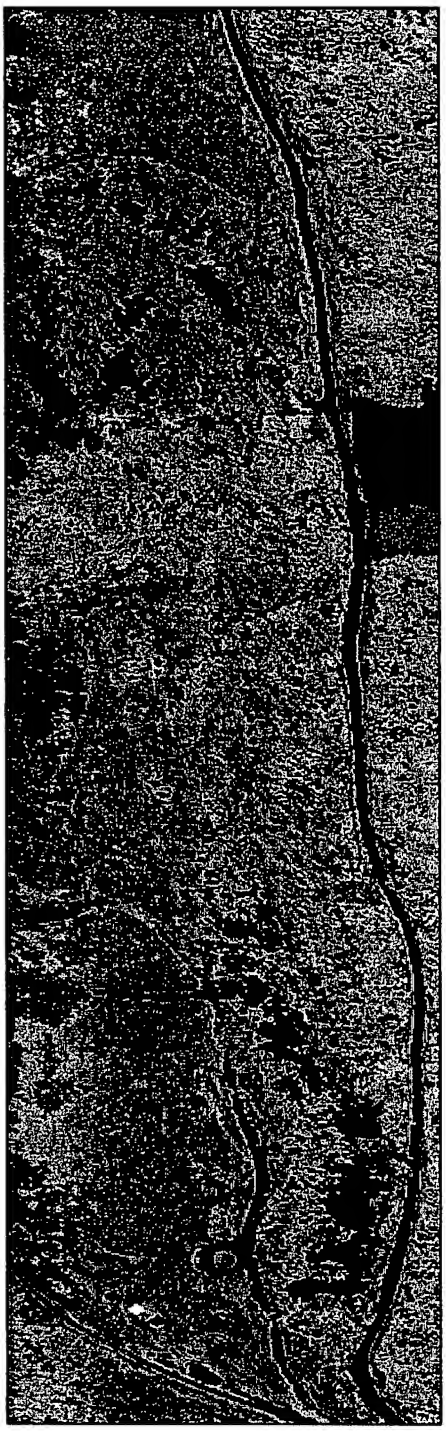

0.3 Radians

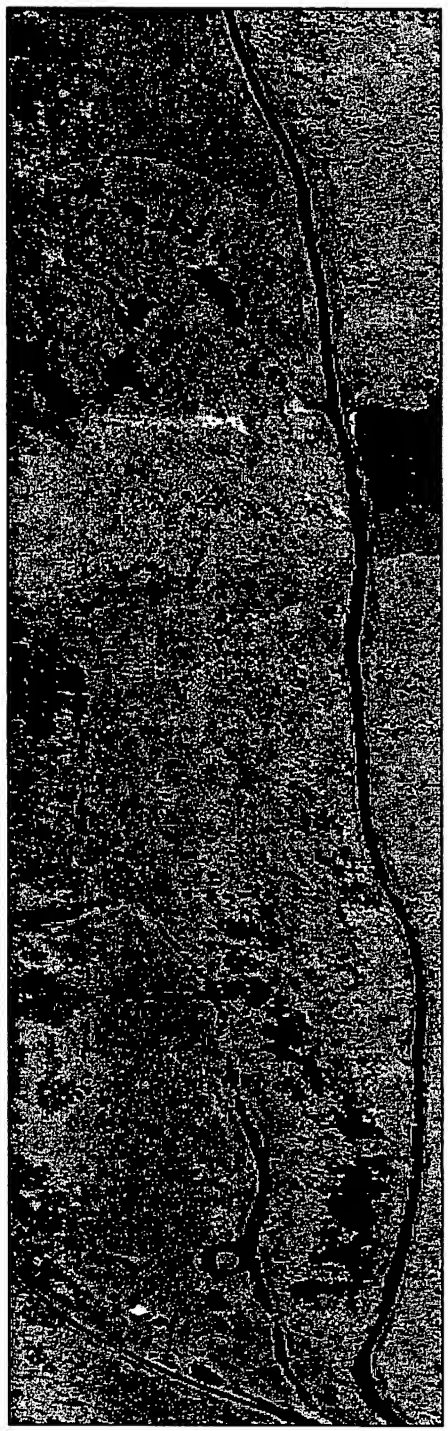

0.5 Radians

Fig. B.3 ELM SAM Mapping Output for 0.3 and 0.5 Radians

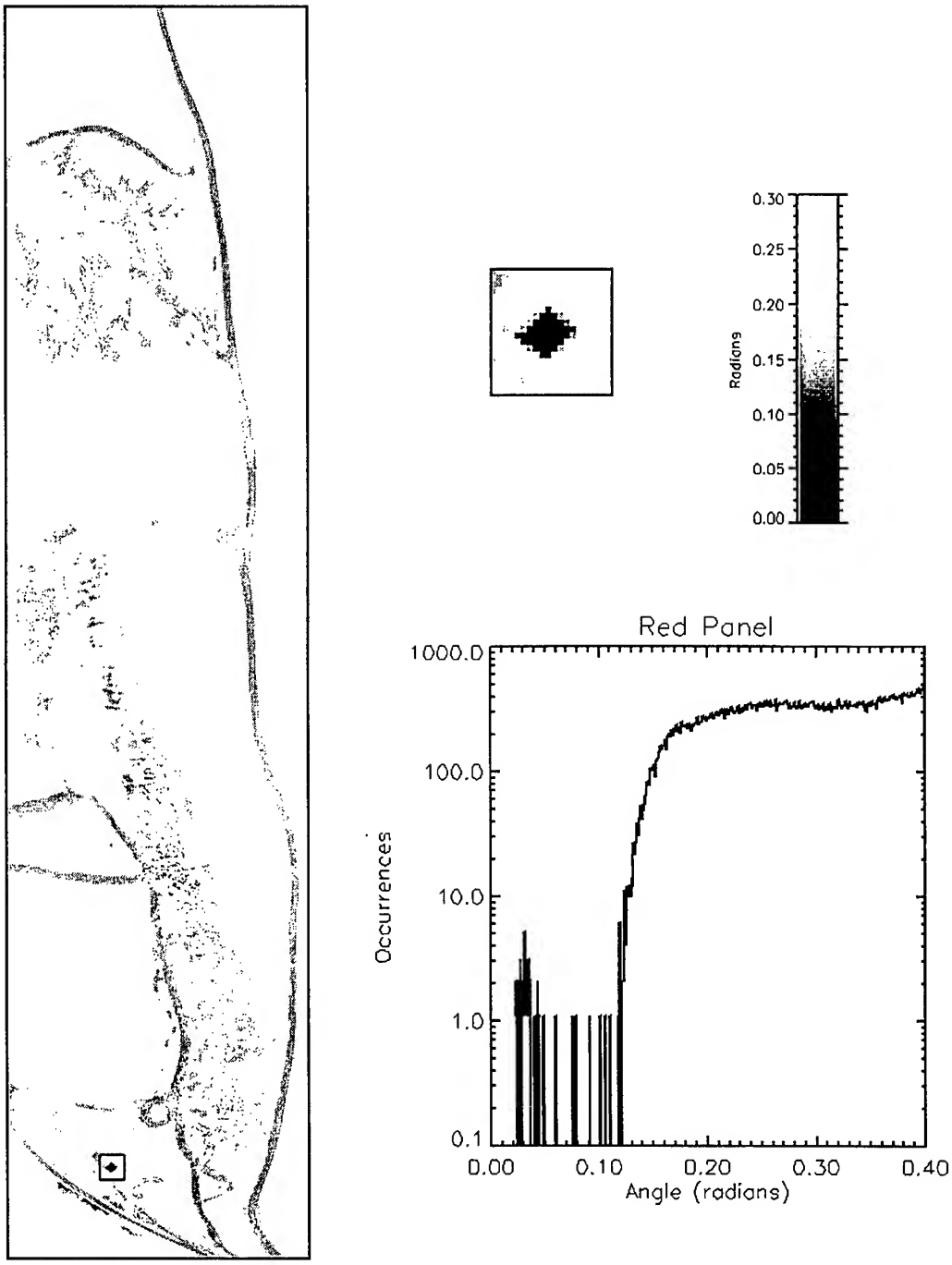

Fig. B.4 ELM SAM Rule Image for Red Panel

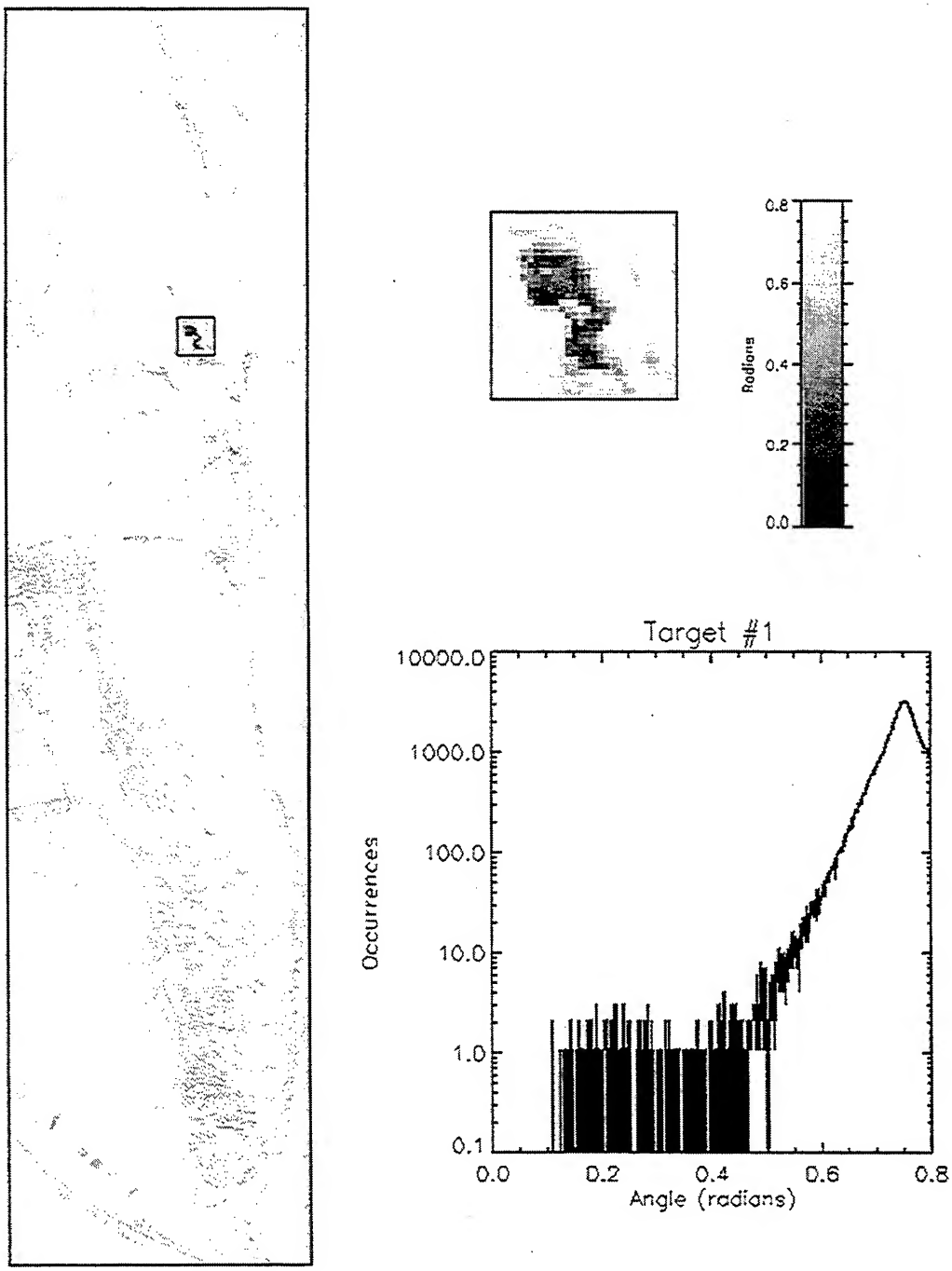

Fig. B.5 ELM SAM Rule Image for Target #1

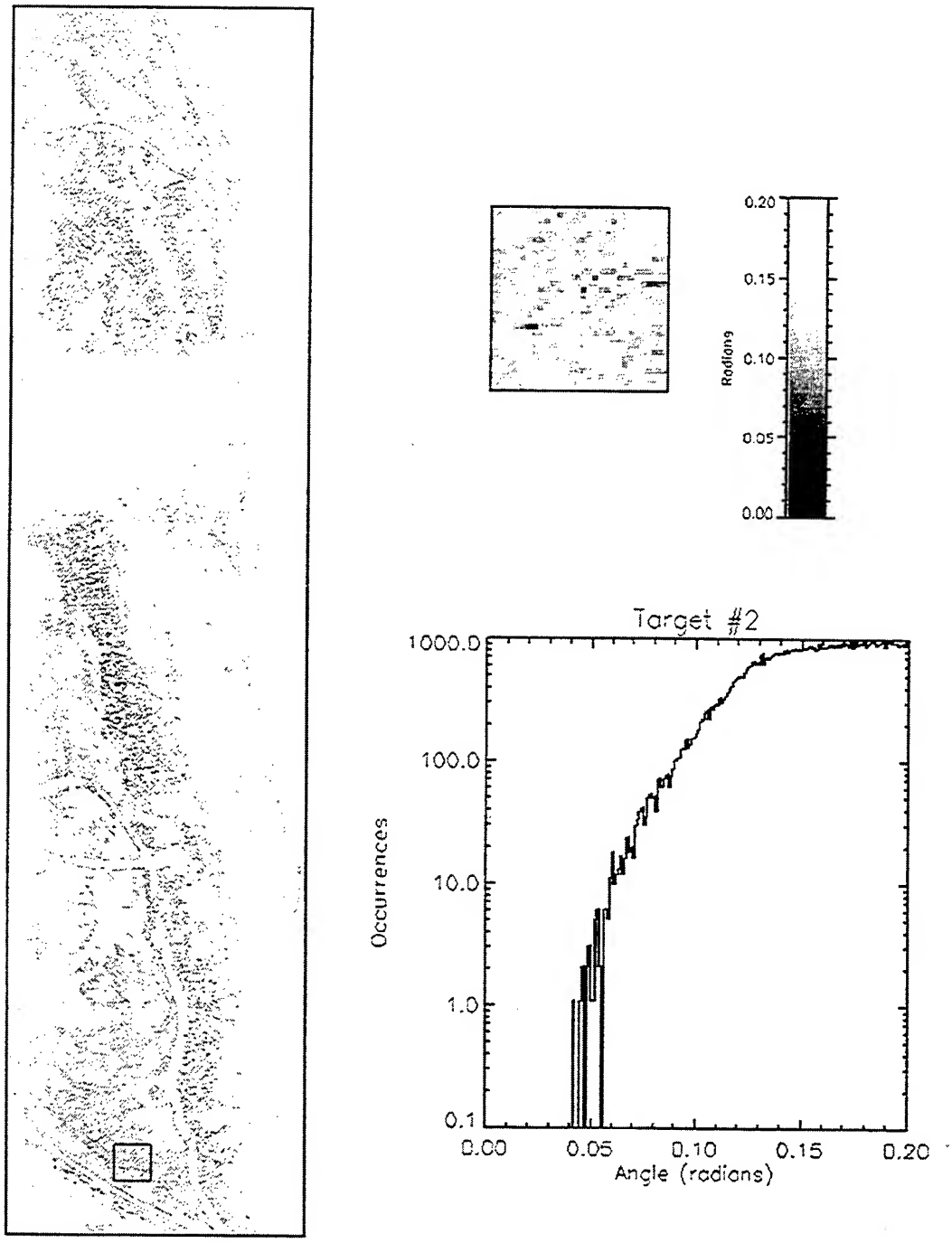

Fig. B.6 ELM SAM Rule Image for Target #2

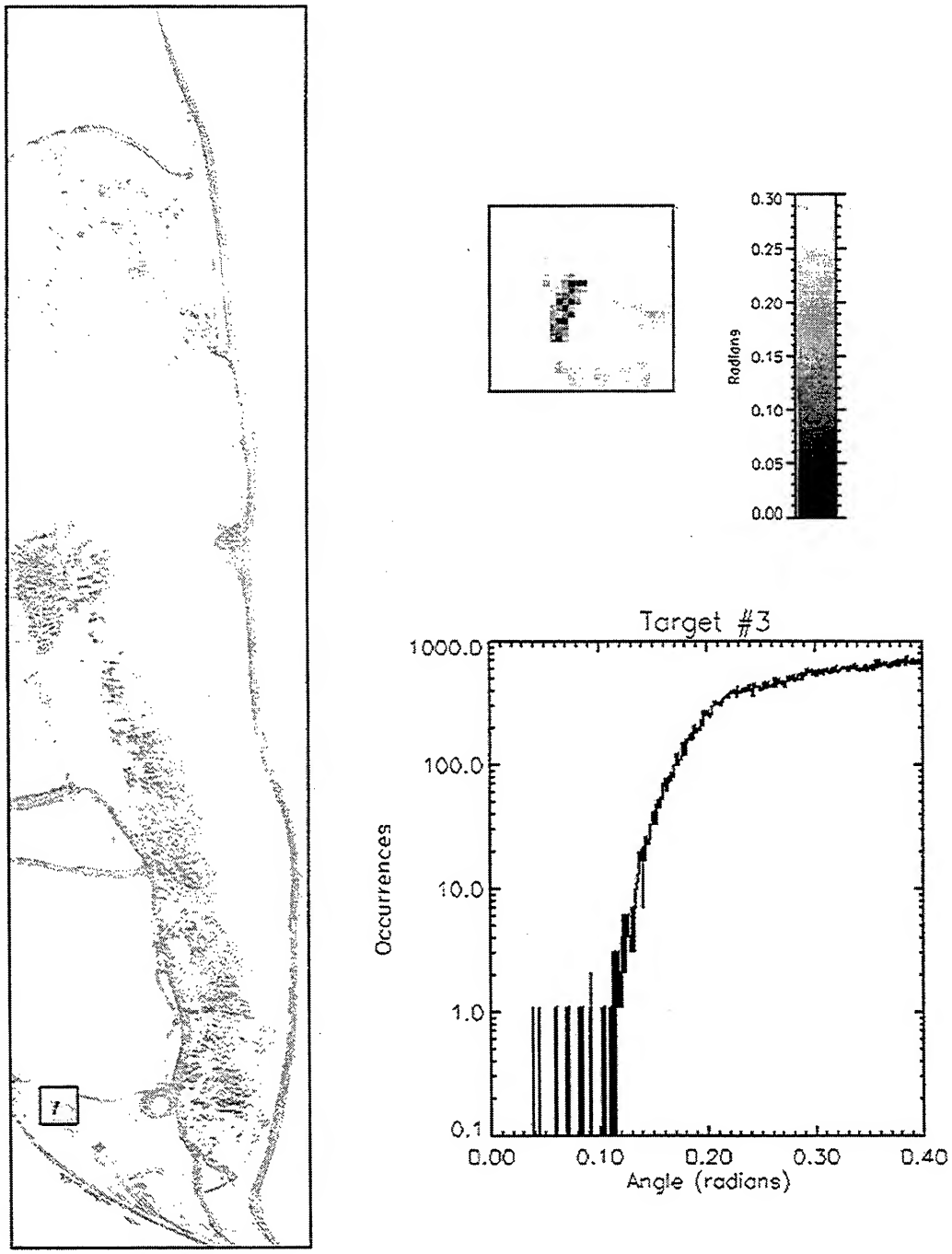

Fig. B.7 ELM SAM Rule Image for Target #3

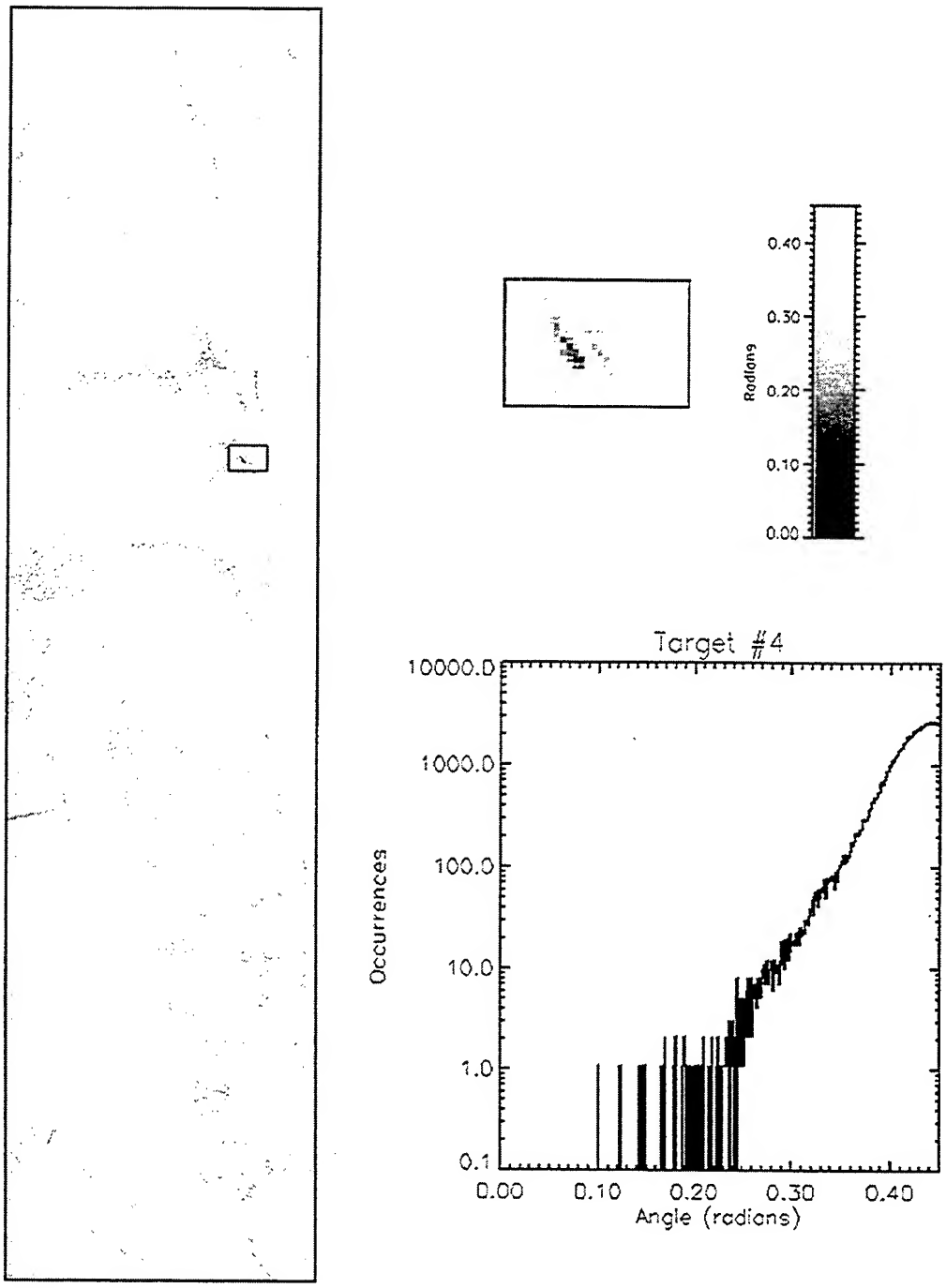

Fig. B.8 ELM SAM Rule Image for Target #4

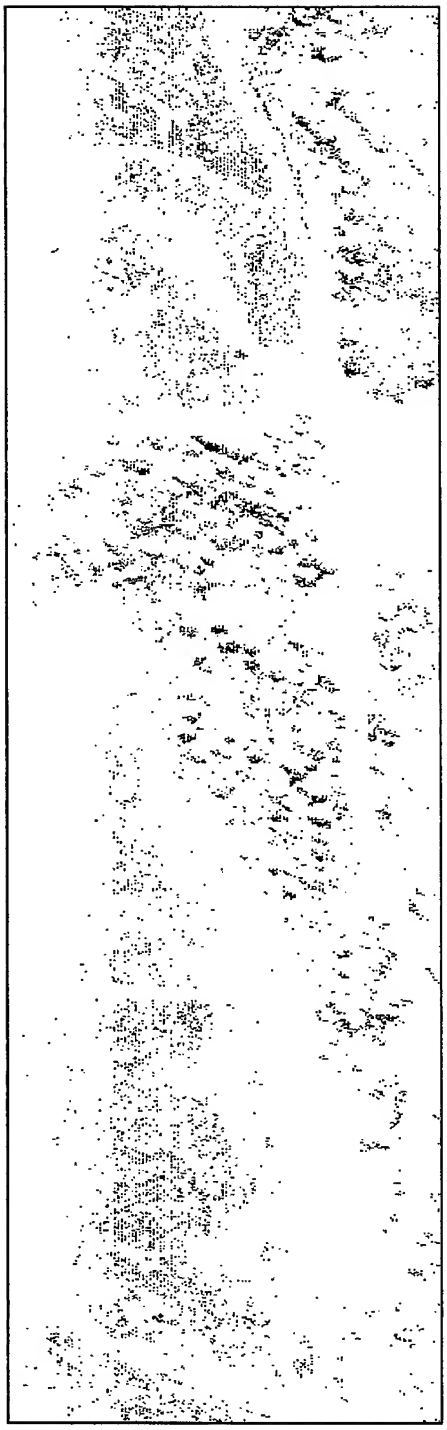

0.1 Radians

0.2 Radians

Fig. B.9 EISC SAM Mapping Output for 0.1 and 0.2 Radians

0.3 Radians

0.5 Radians

Fig. B.10 EISC SAM Mapping Output for 0.3 and 0.5 Radians

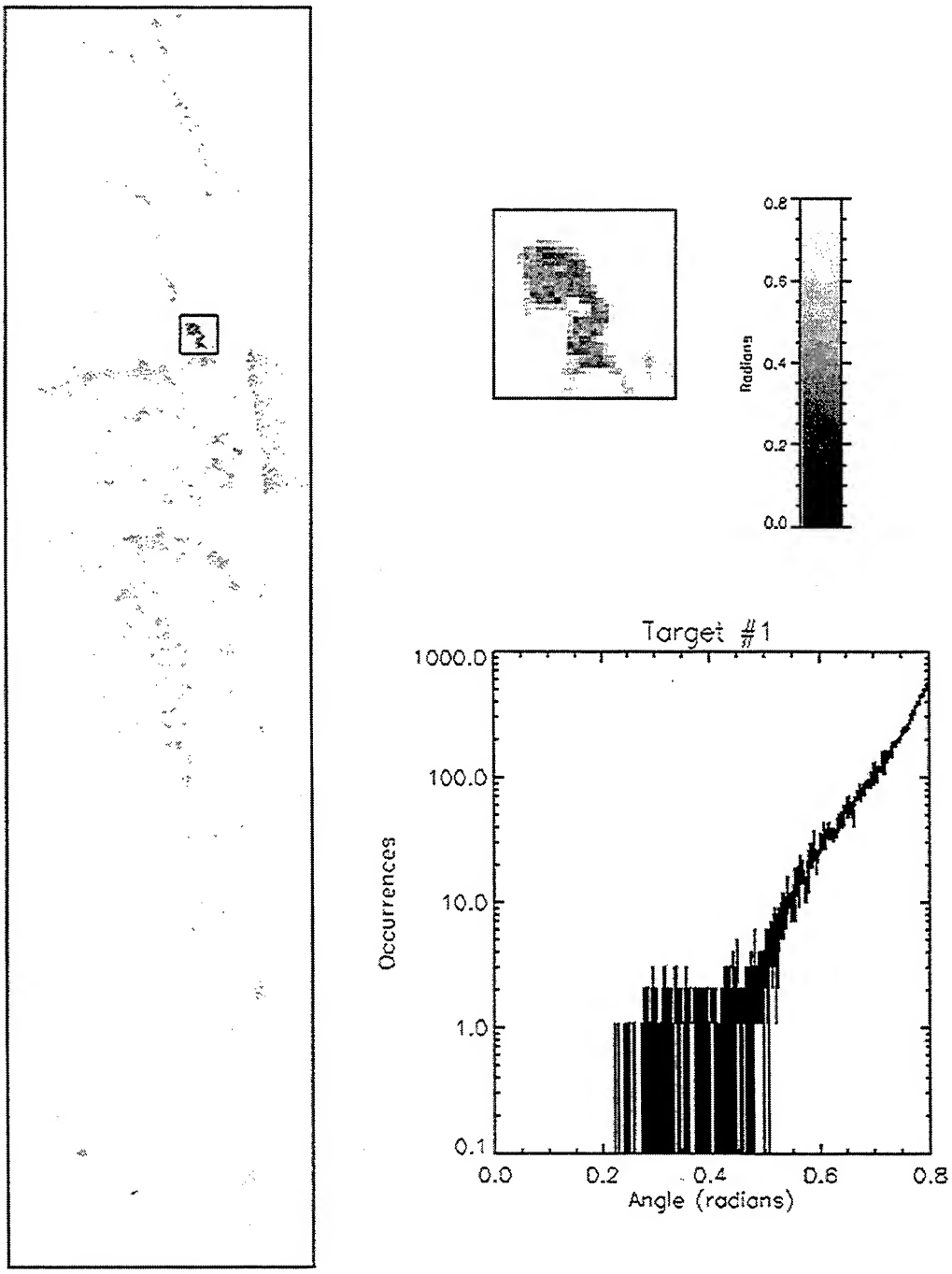

Fig. B.11 EISC SAM Rule Image for Target #1

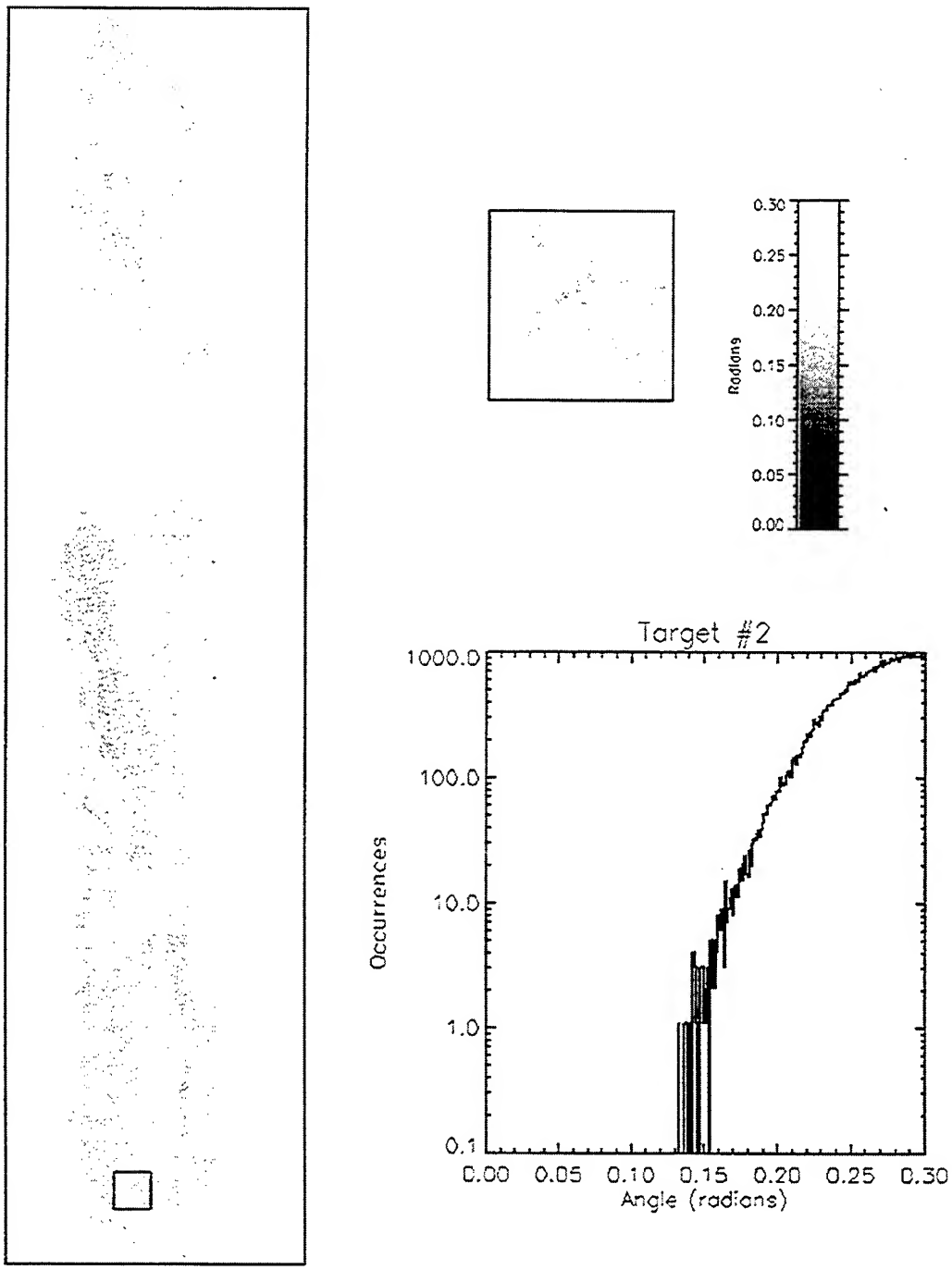

Fig. B.12 ELM SAM Rule Image for Target #2

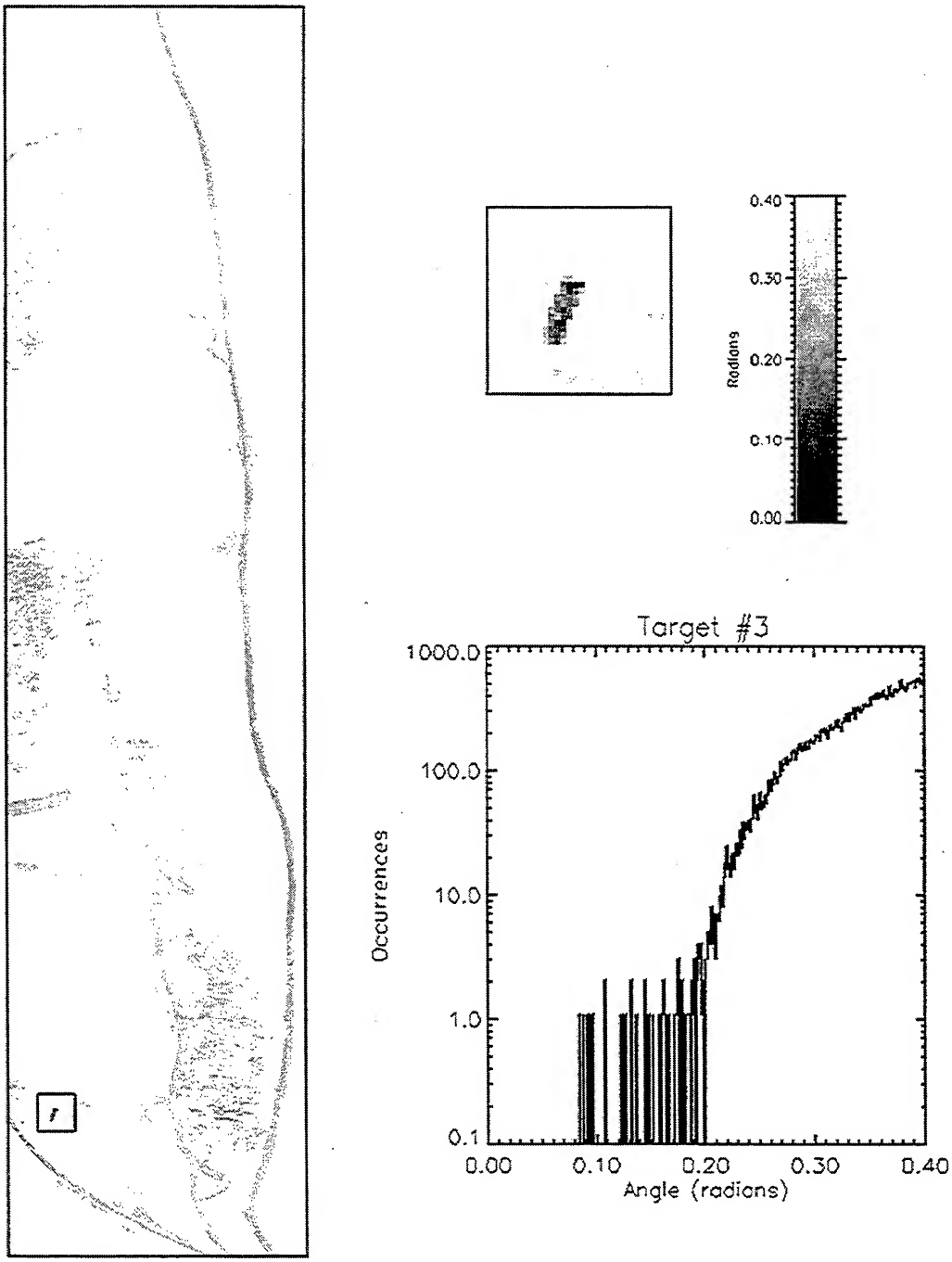

Fig. B.13 EISC SAM Rule Image for Target #3

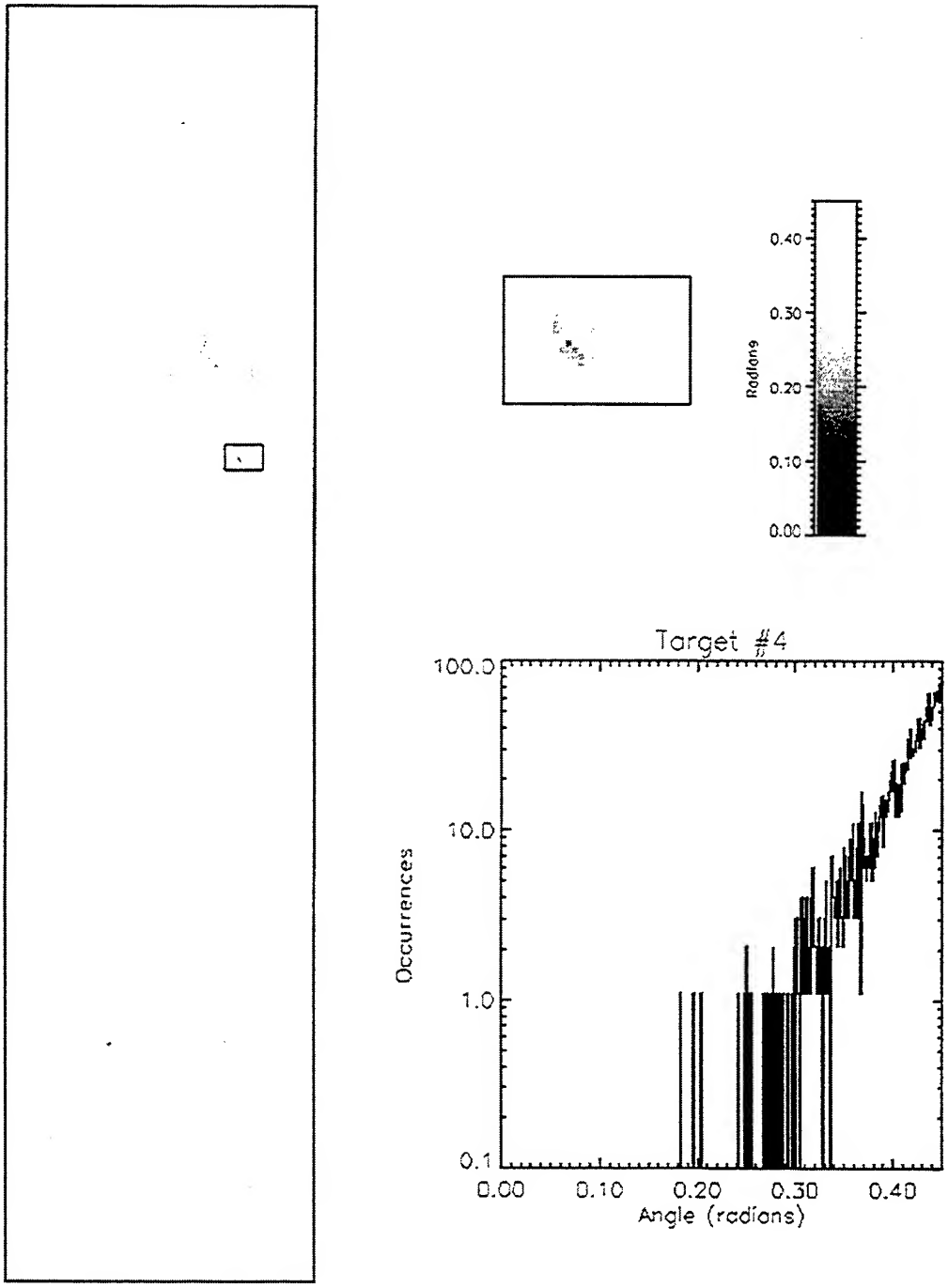

Fig. B.14 EISC SAM Rule Image for Target #4

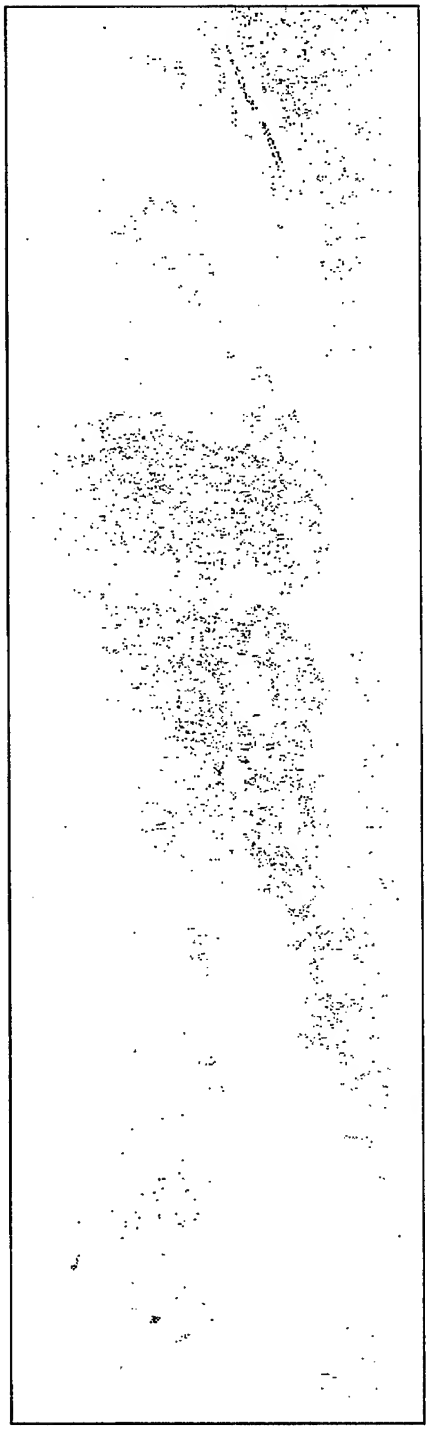

1.5 Std Dev

2.0 Std Dev

Fig. B.15 Parallelepiped Mapping Output for 1.5 and 2.0 Std Dev

3.0 Std Dev

4.0 Std Dev

Fig. B.16 Parallelepiped Mapping Output for 3.0 and 4.0 Std Dev

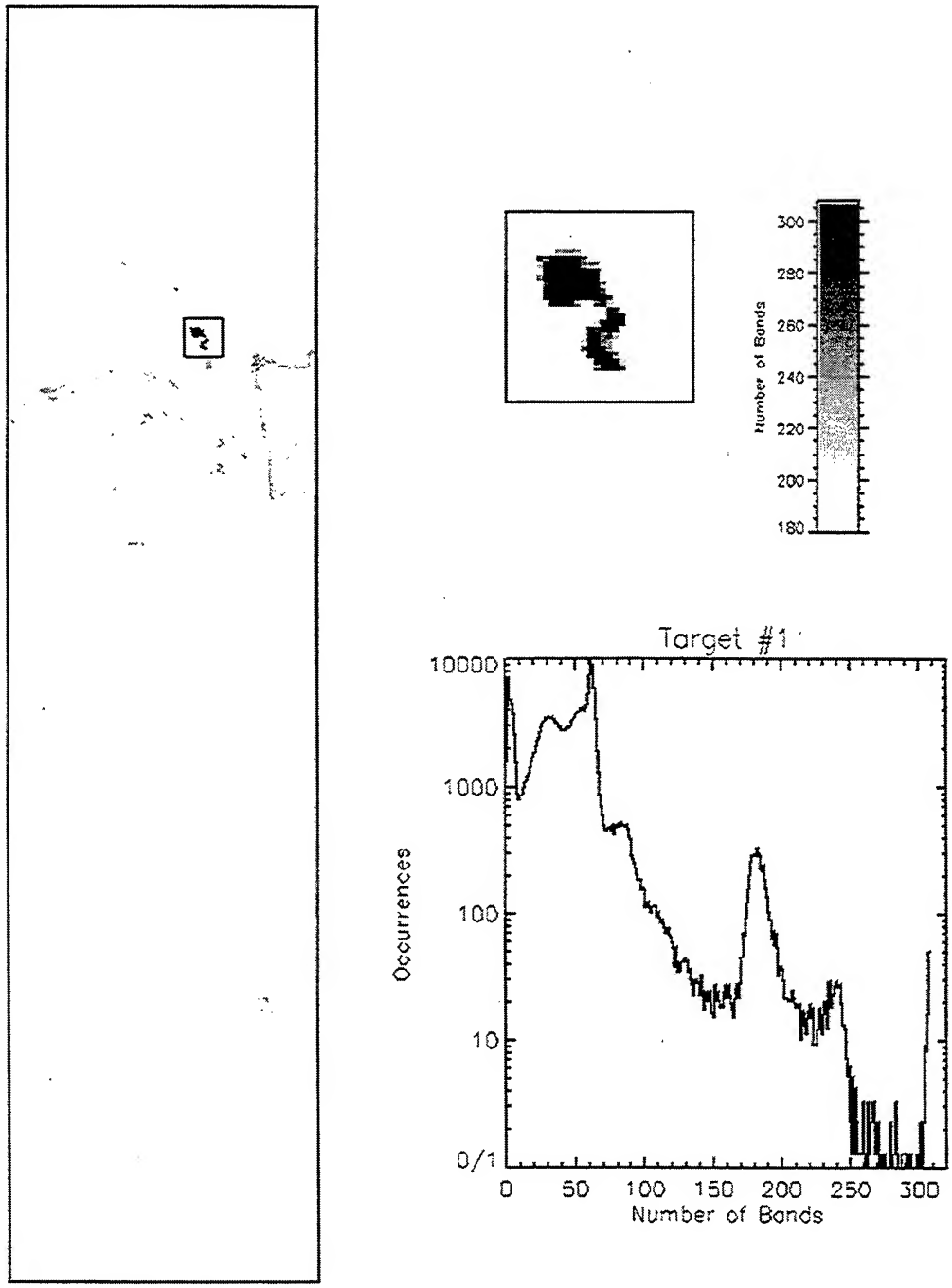

Fig. B.17 Parallelepiped Rule Image for Target #1

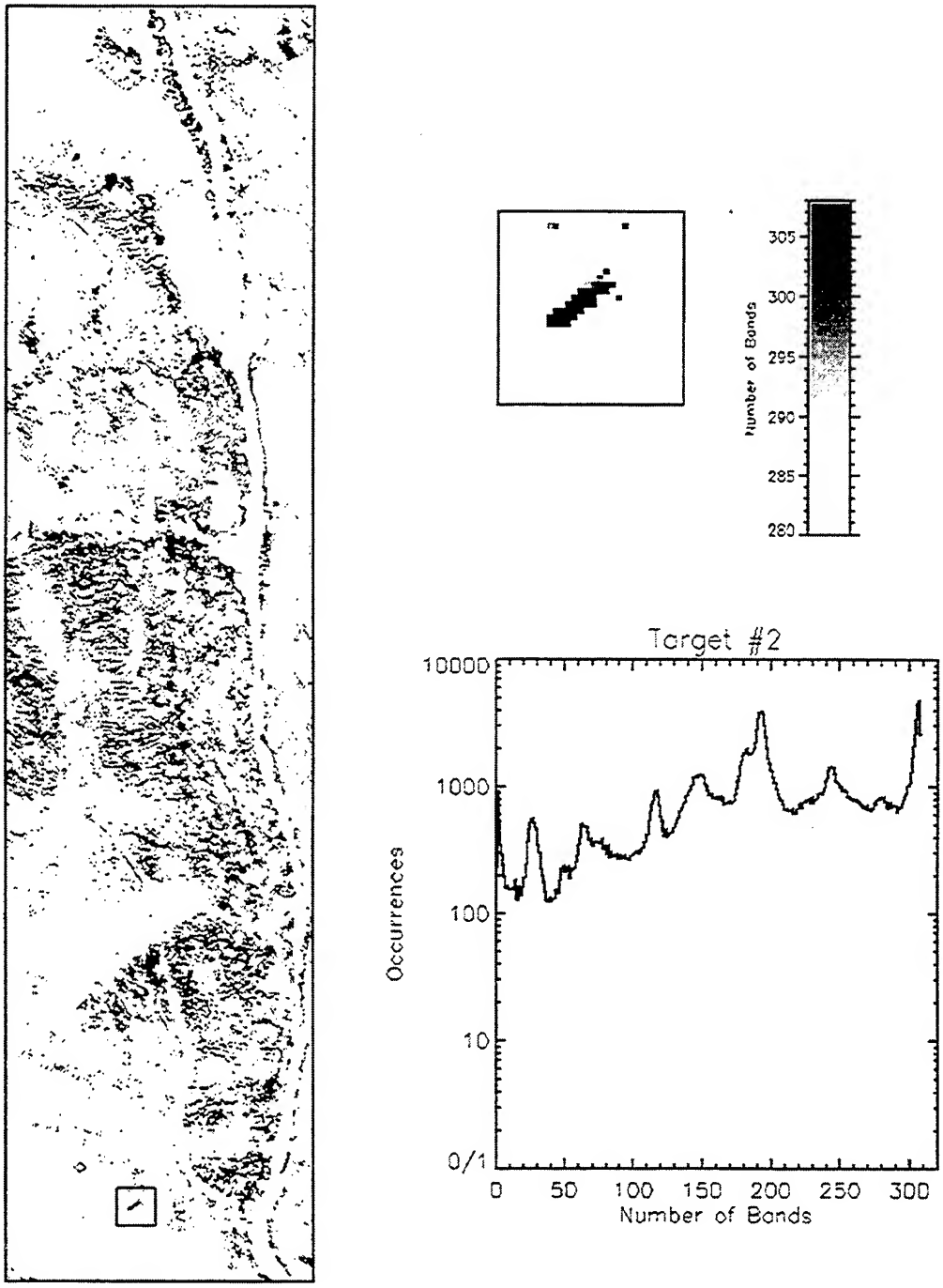

Fig. B.18 Parallelepiped Rule Image for Target #2

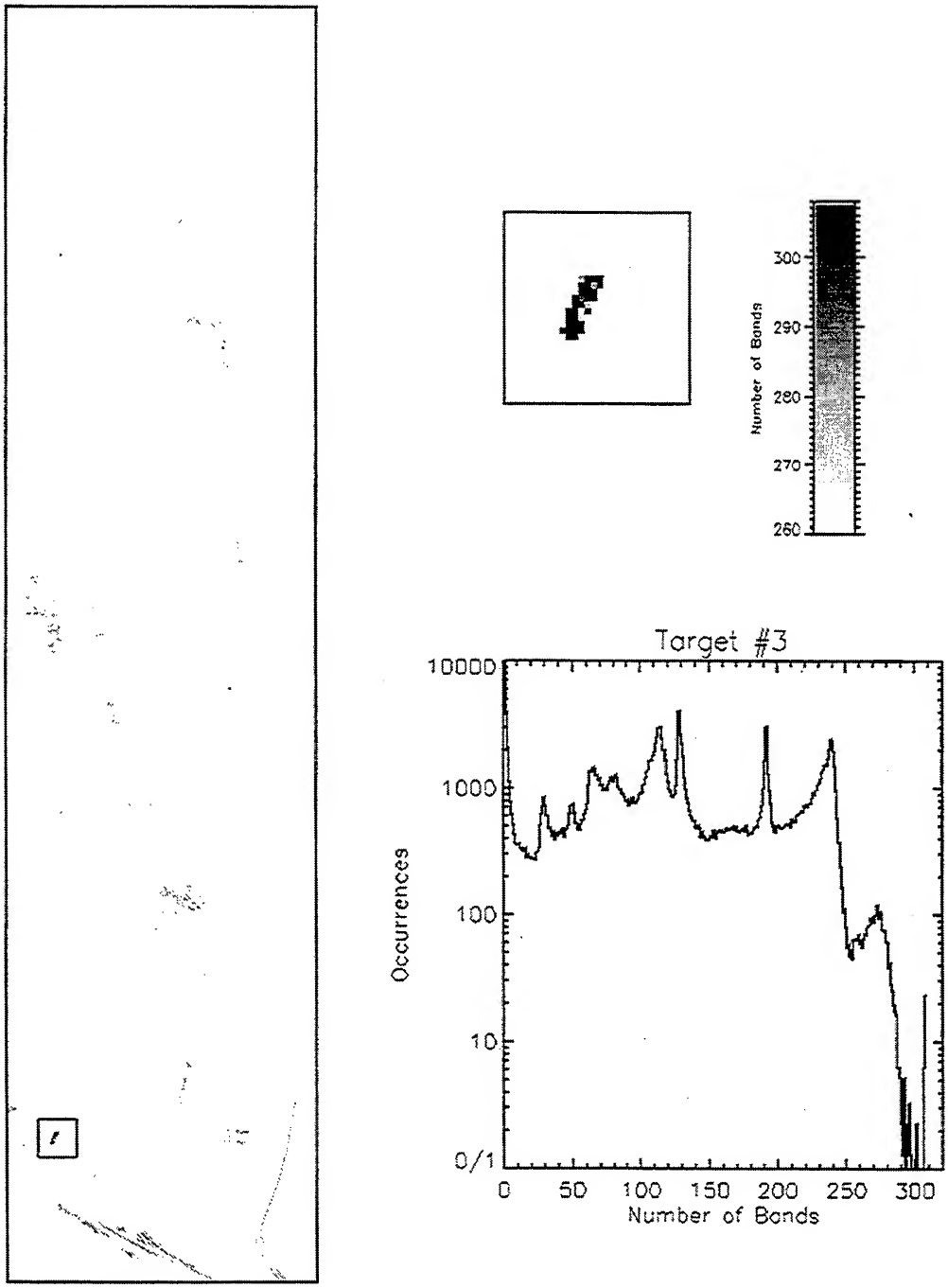

Fig. B.19 Parallelepiped Rule Image for Target #3

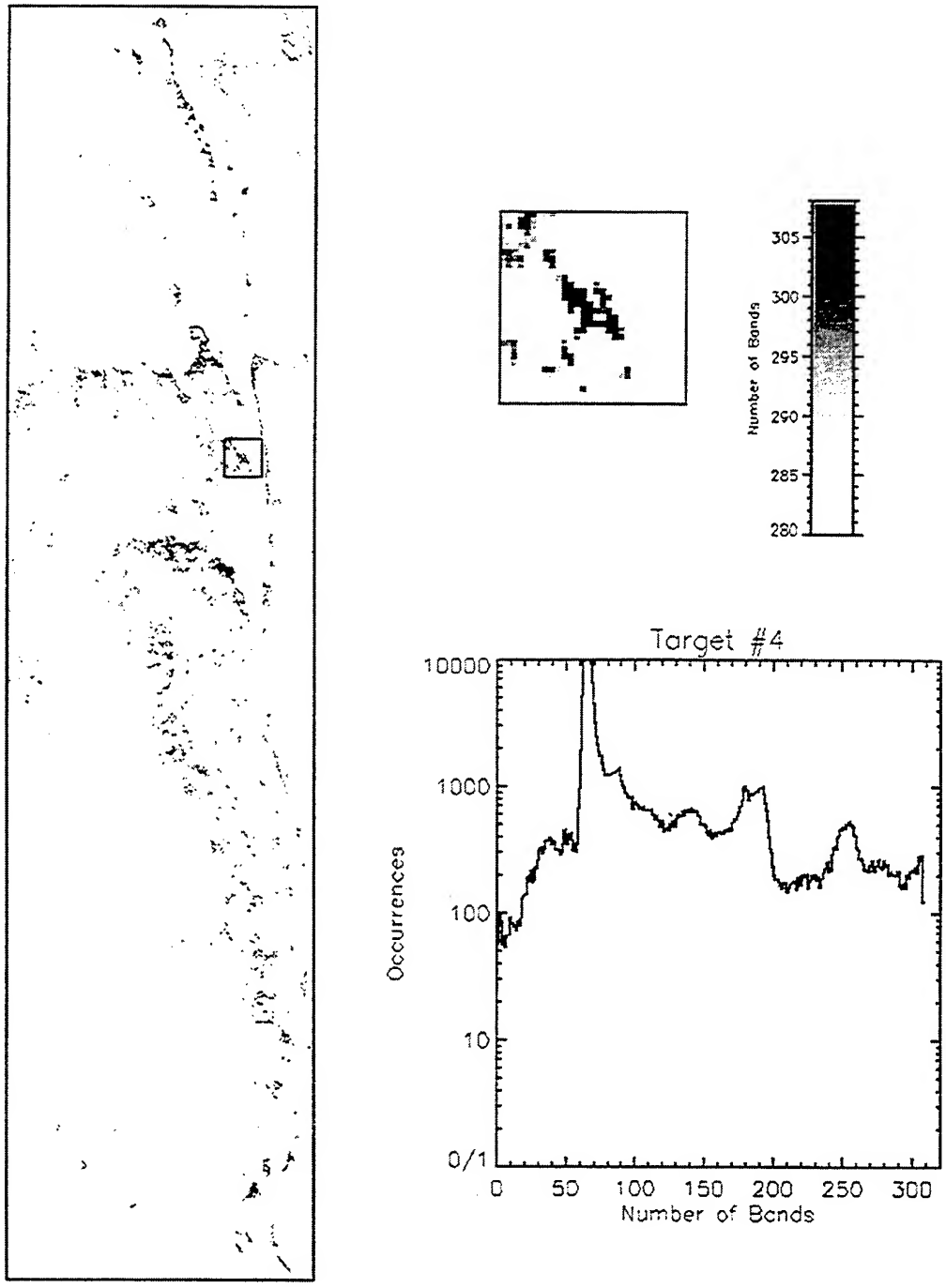

Fig. B.20 Parallelepiped Rule Image for Target #4

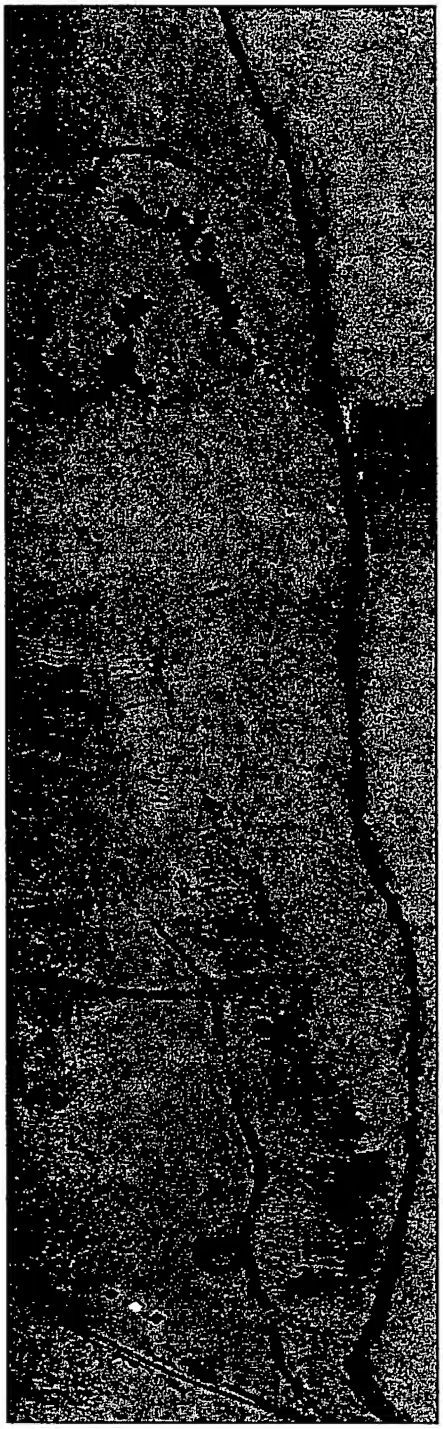

50%

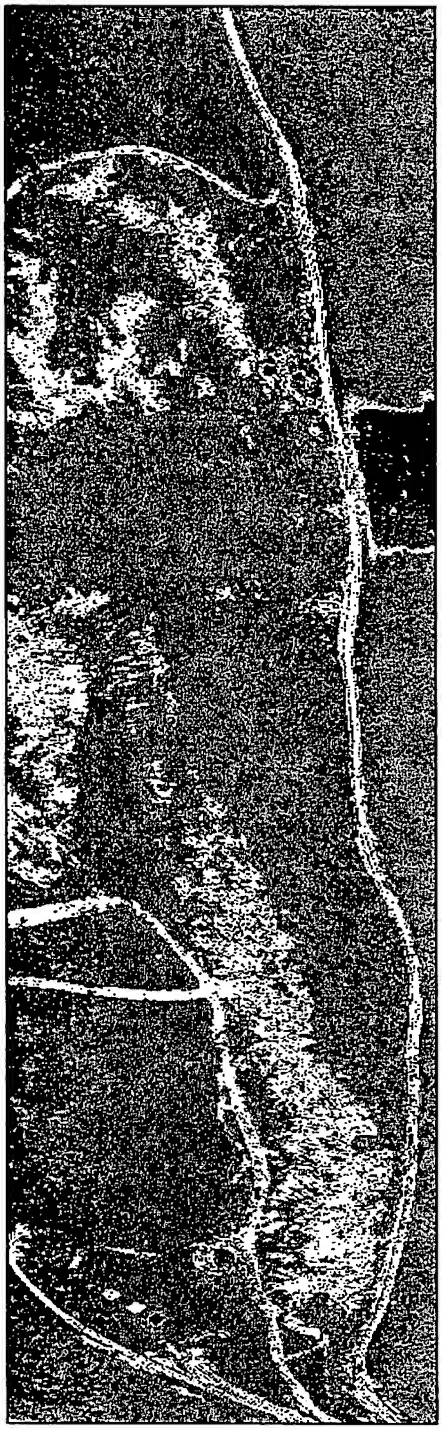

90%

Fig. B.21 Binary Encoding Mapping Output for 50% and 90% Certainty

95%

99%

Fig. B.22 Binary Encoding Mapping Output for 95% and 99% Certainty

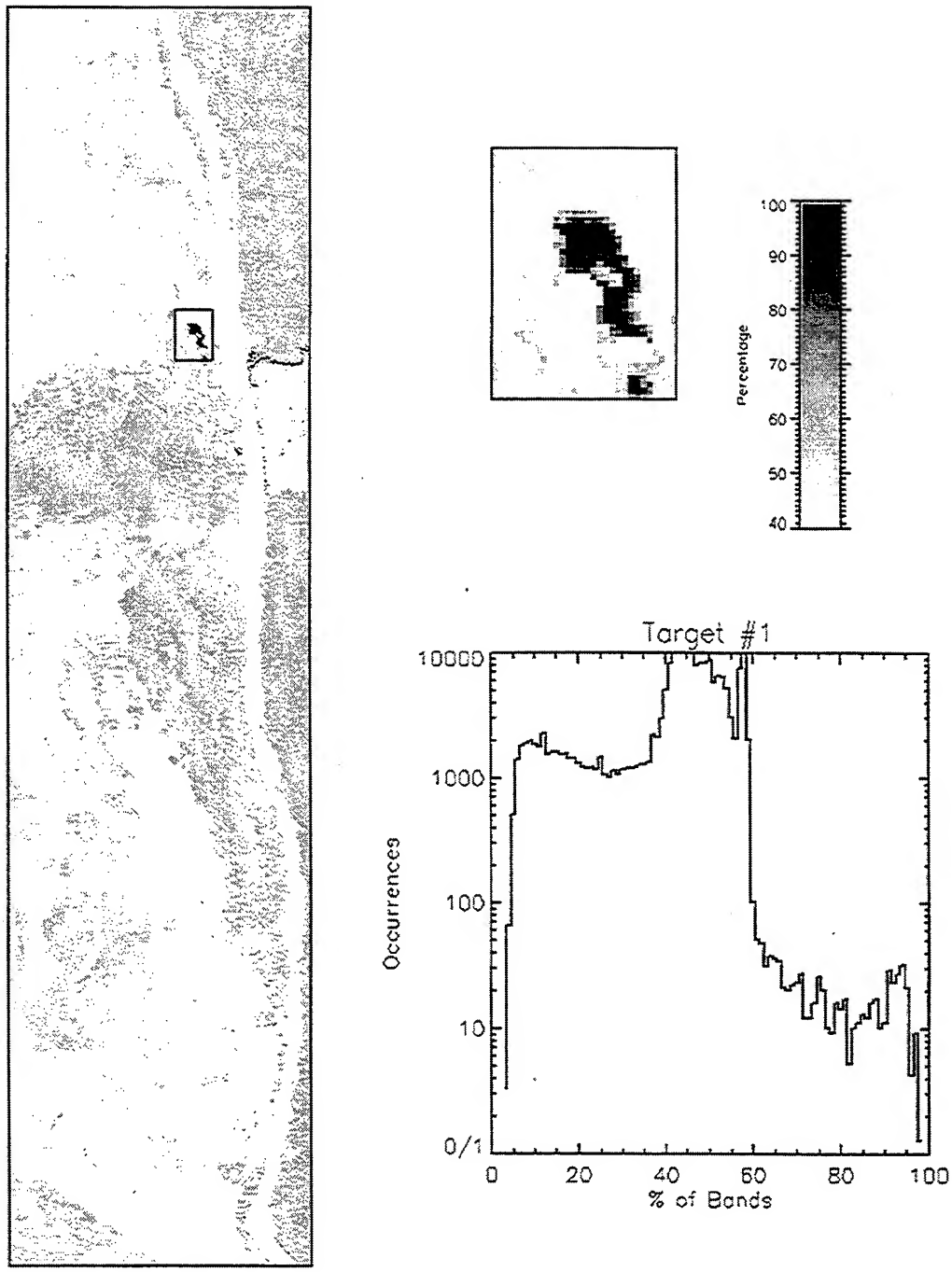

Fig. B.23 Binary Encoding Rule Image for Target #1

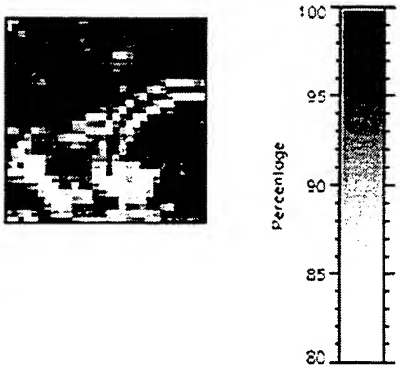

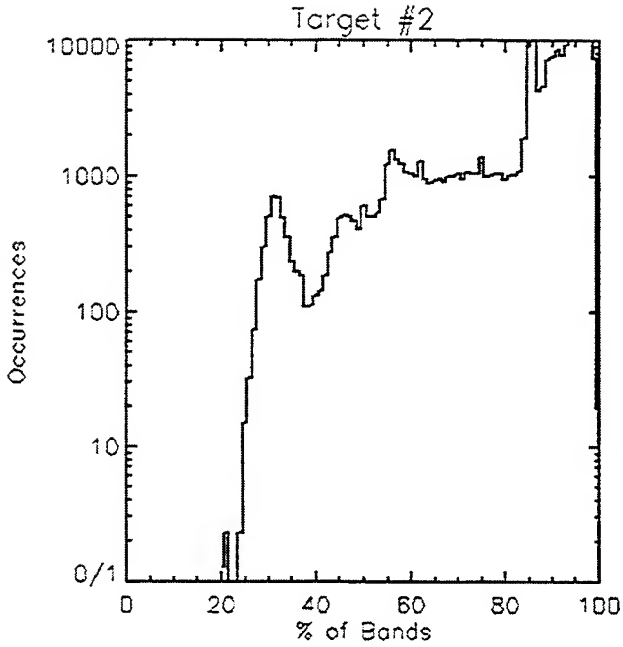

Fig. B.24 Binary Encoding Rule Image for Target #2

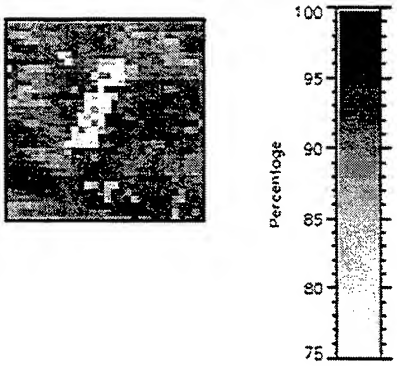

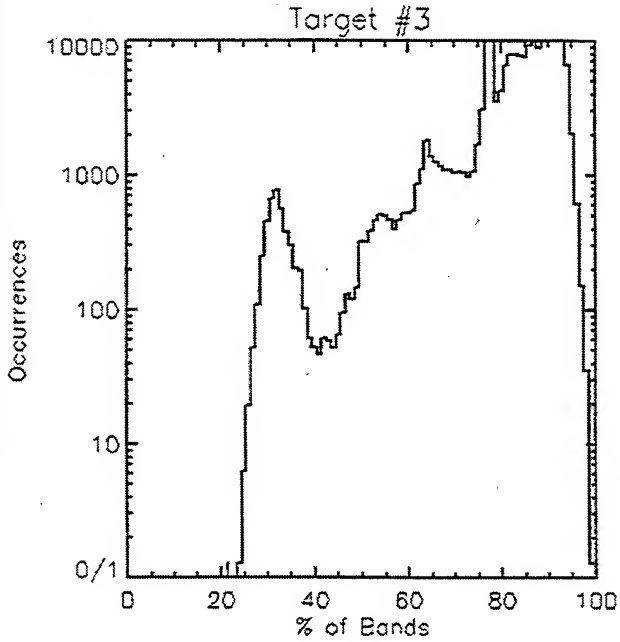

Fig. B.25 Binary Encoding Rule Image for Target #3

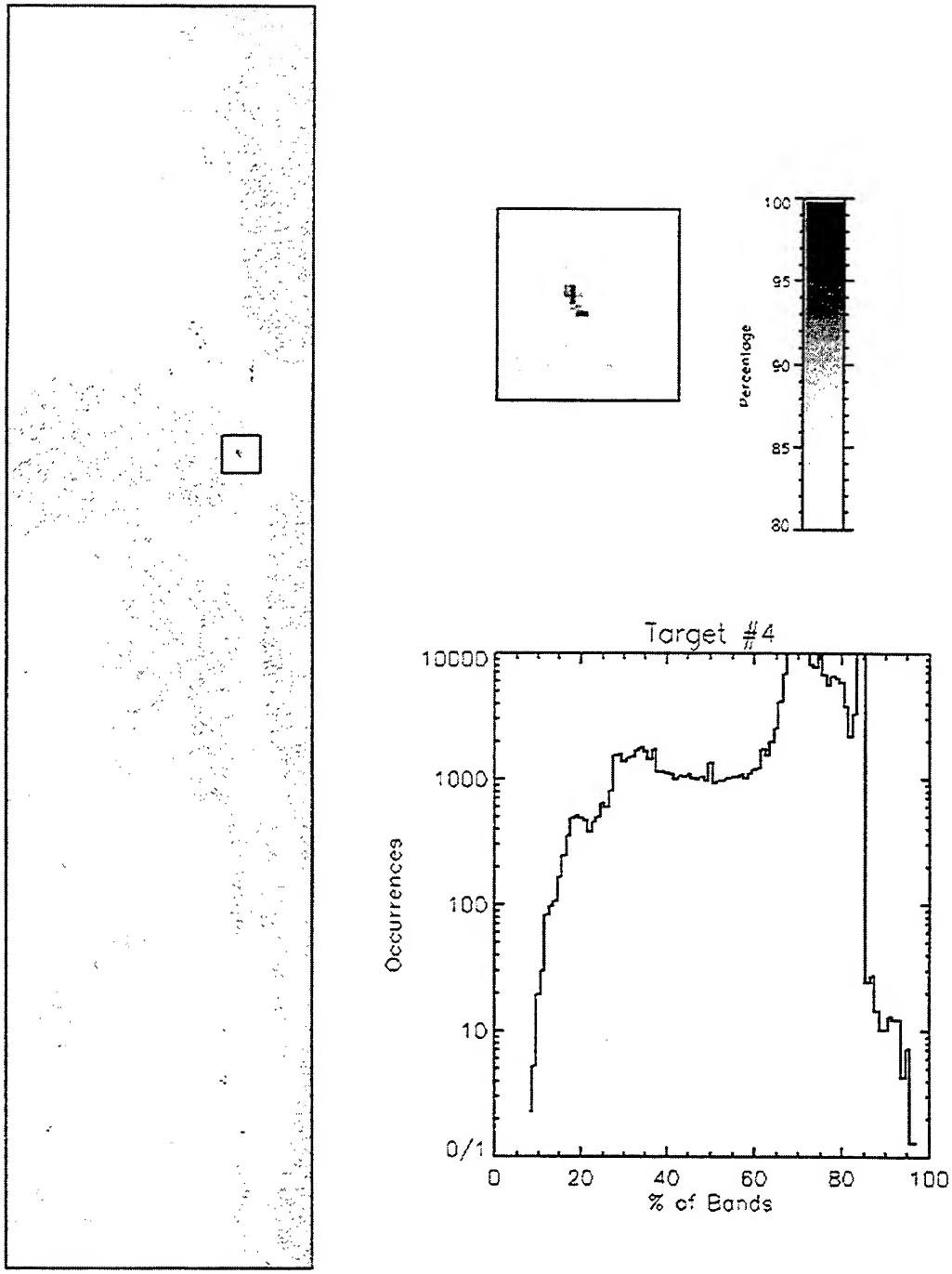

Fig. B.26 Binary Encoding Rule Image for Target #4

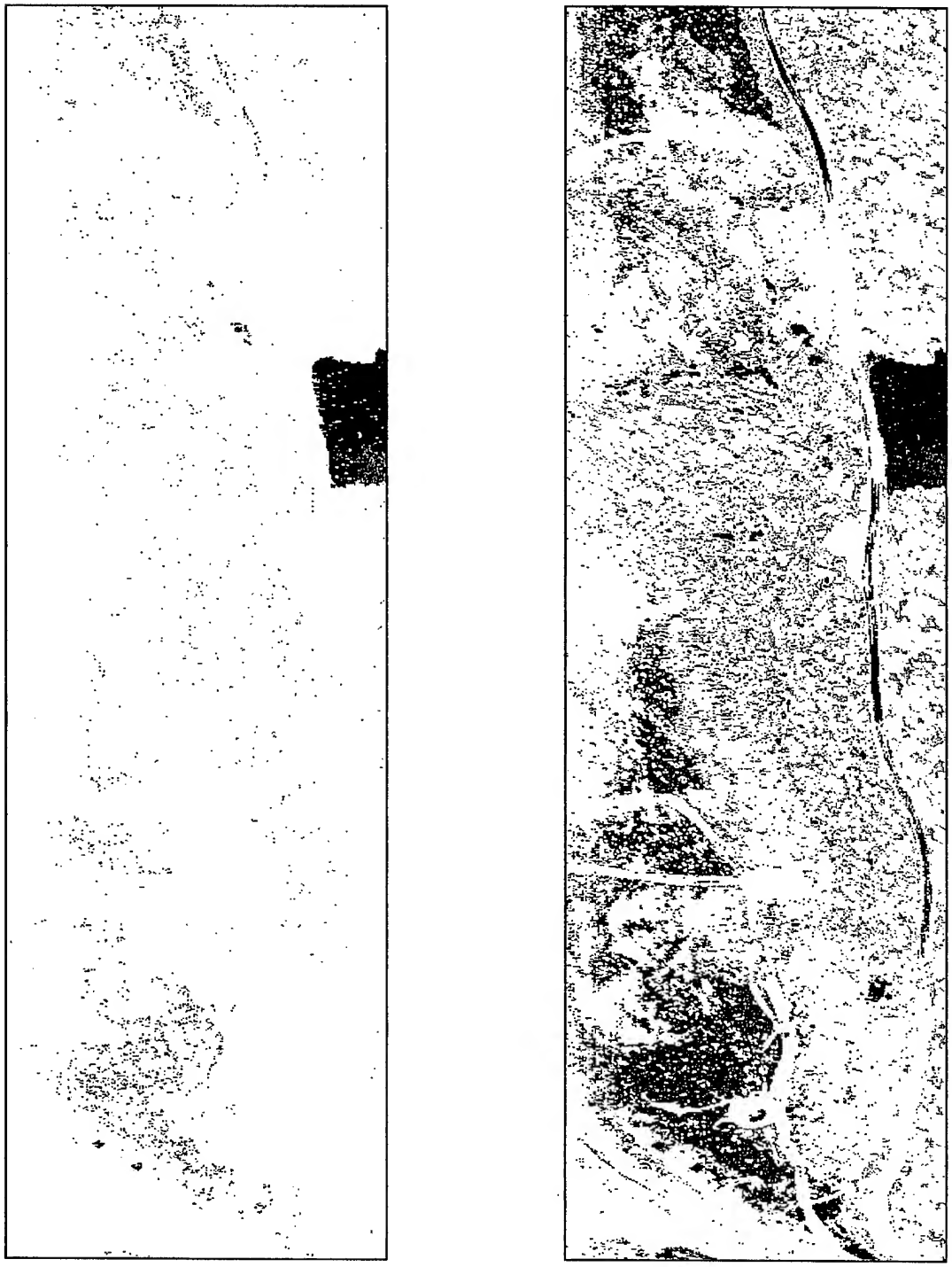

0.2 DN

0.5 DN

Fig. B.27 Minimum Distance Mapping Output for 0.2 and 0.5 DN

1 DN

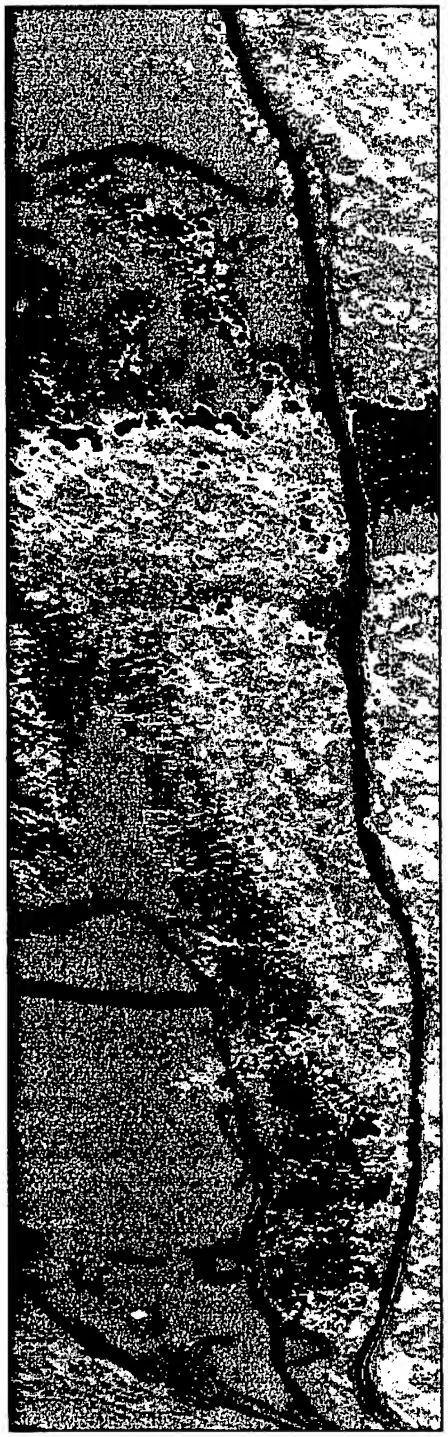

Full Scene

Fig. B.28 Minimum Distance Mapping Output for 1 DN and Full Scene Mapping

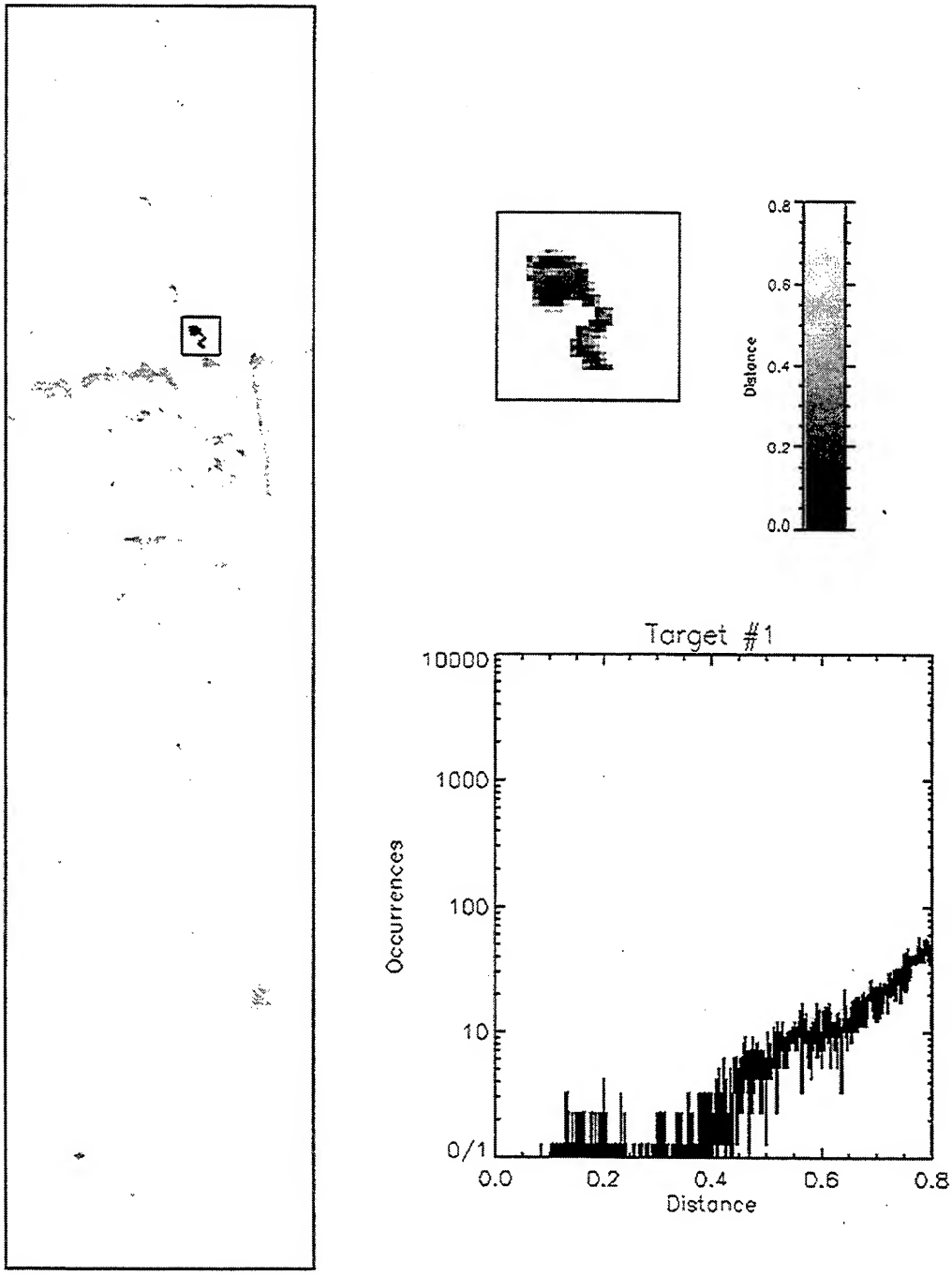

Fig. B.29 Minimum Distance Rule Image for Target #1

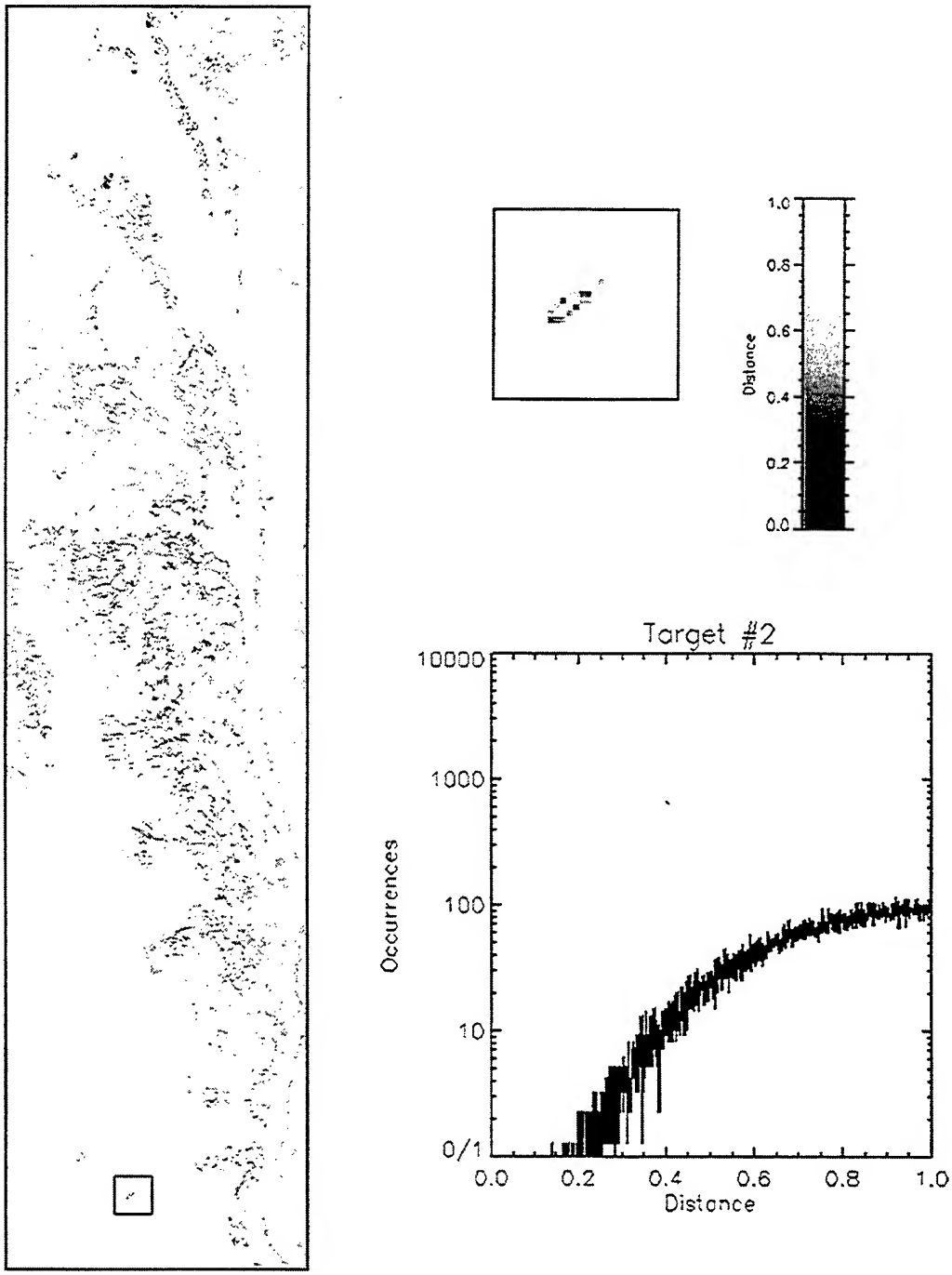

Fig. B.30 Minimum Distance Rule Image for Target #2

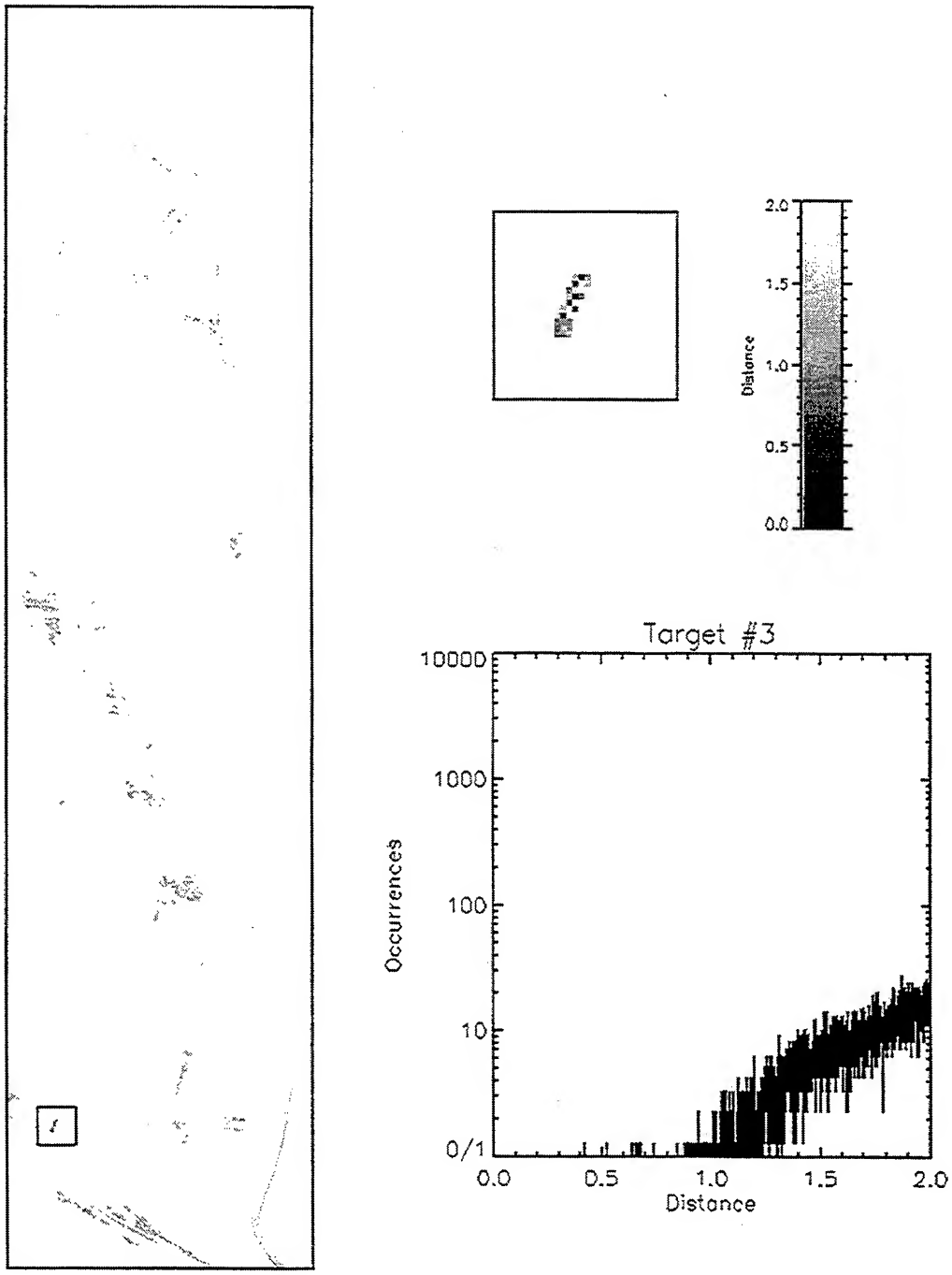

Fig. B.31 Minimum Distance Rule Image for Target #3

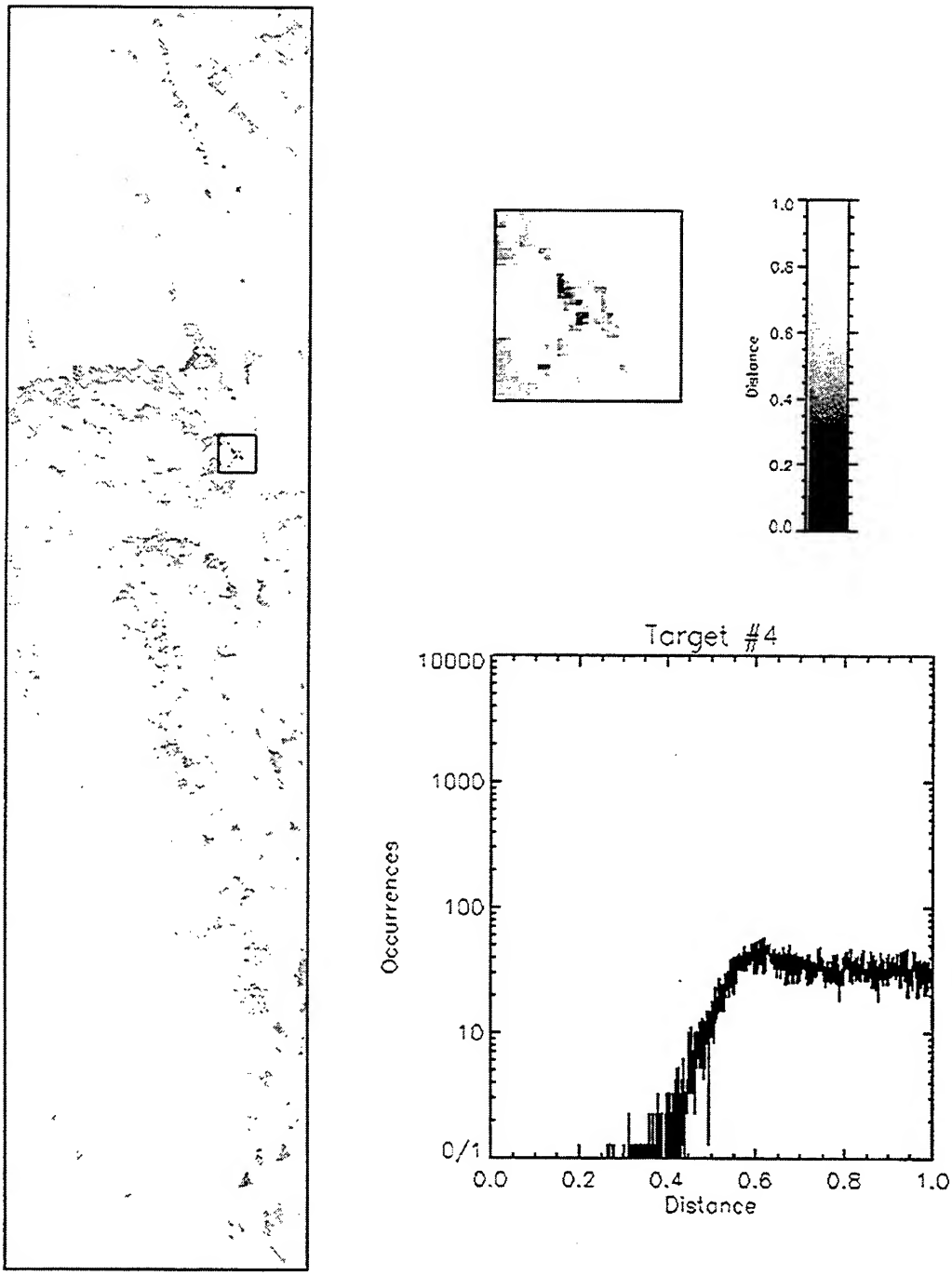

Fig. B.32 Minimum Distance Rule Image for Target #4

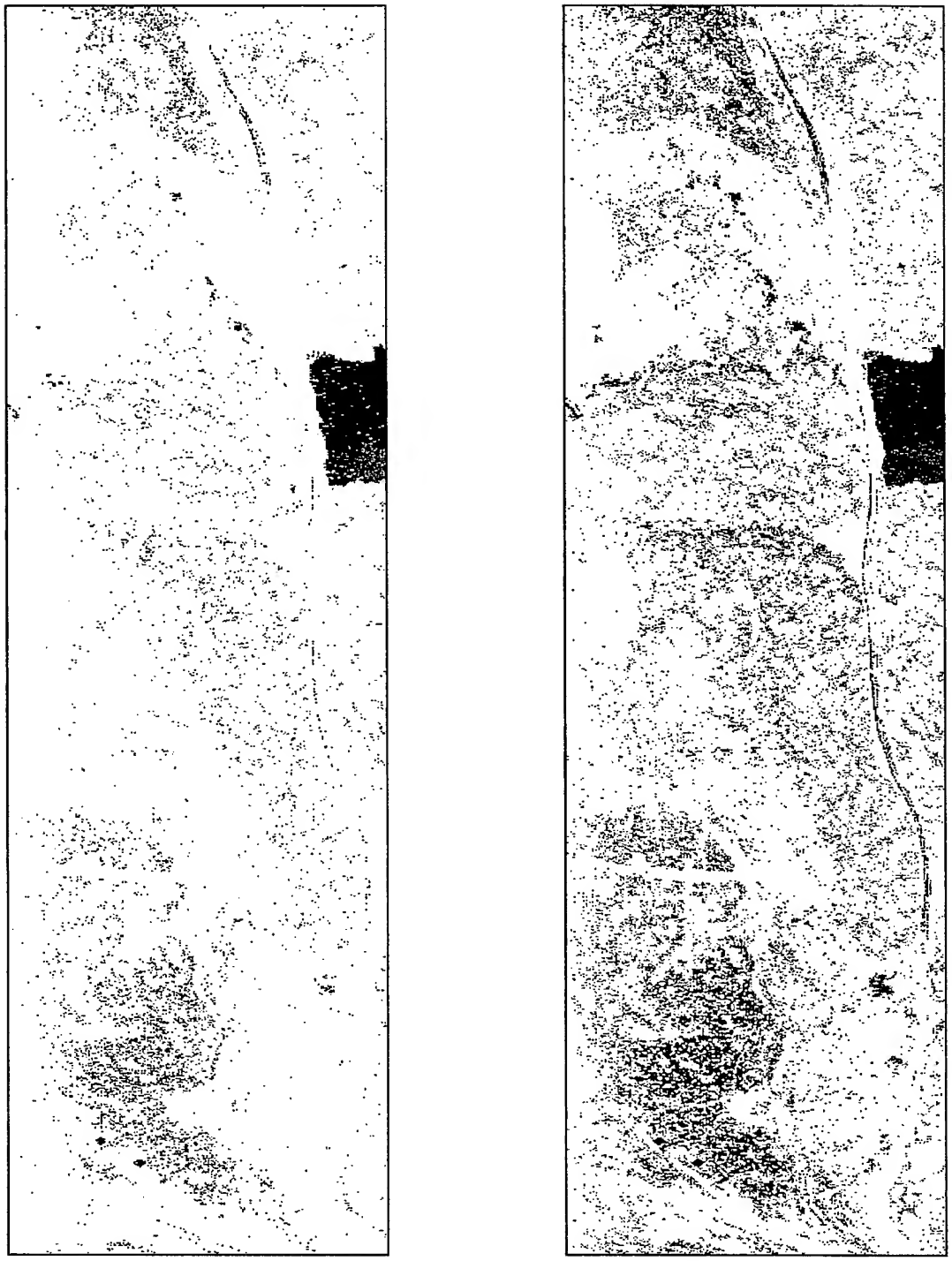

10 DN 20 DN

Fig. B.33 Mahalanobis Distance Mapping Output for 10 and 20 DN

25 DN

50 DN

Fig. B.34 Mahalanobis Distance Mapping Output for 25 and 50 DN

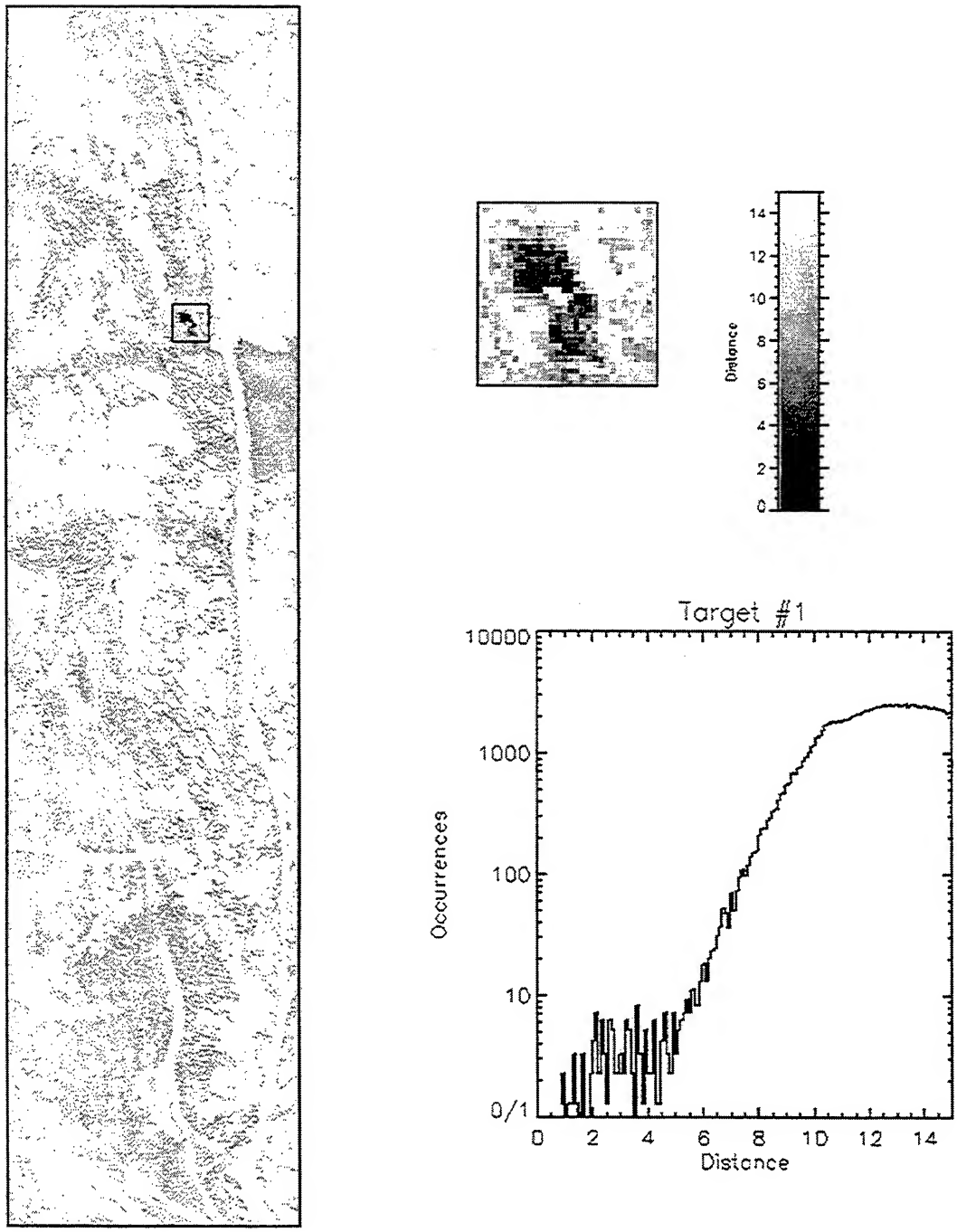

Fig. B.35 Mahalanobis Distance Rule Image for Target #1

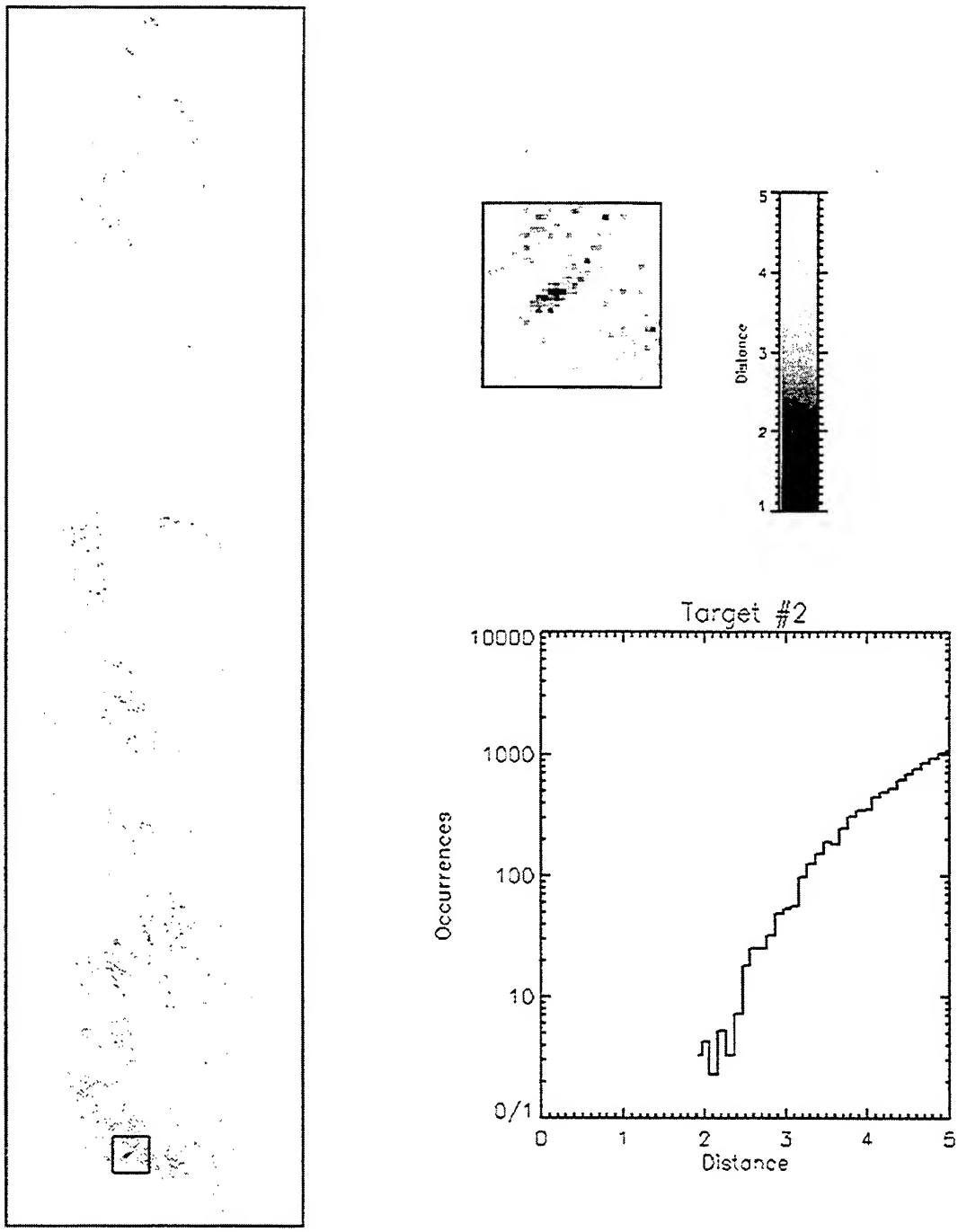

Fig. B.36 Mahalanobis Distance Rule Image for Target #2

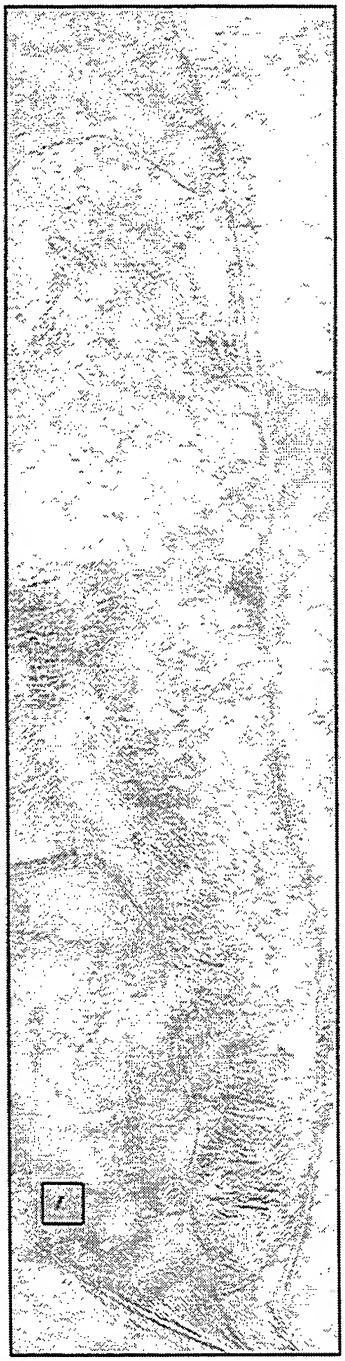

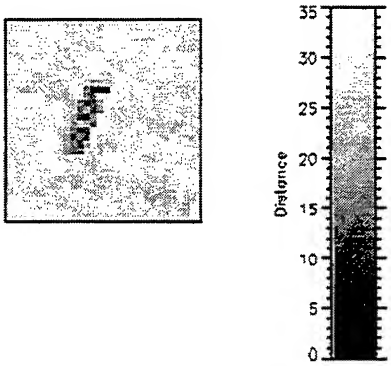

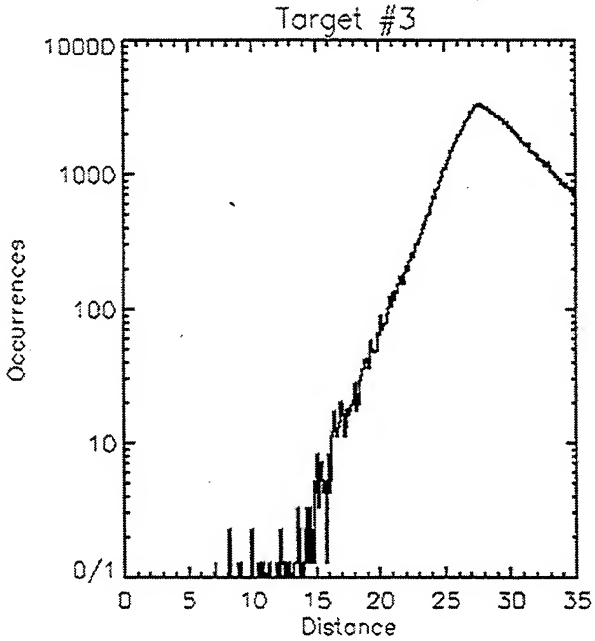

Fig. B.37 Mahalanobis Distance Rule Image for Target #3

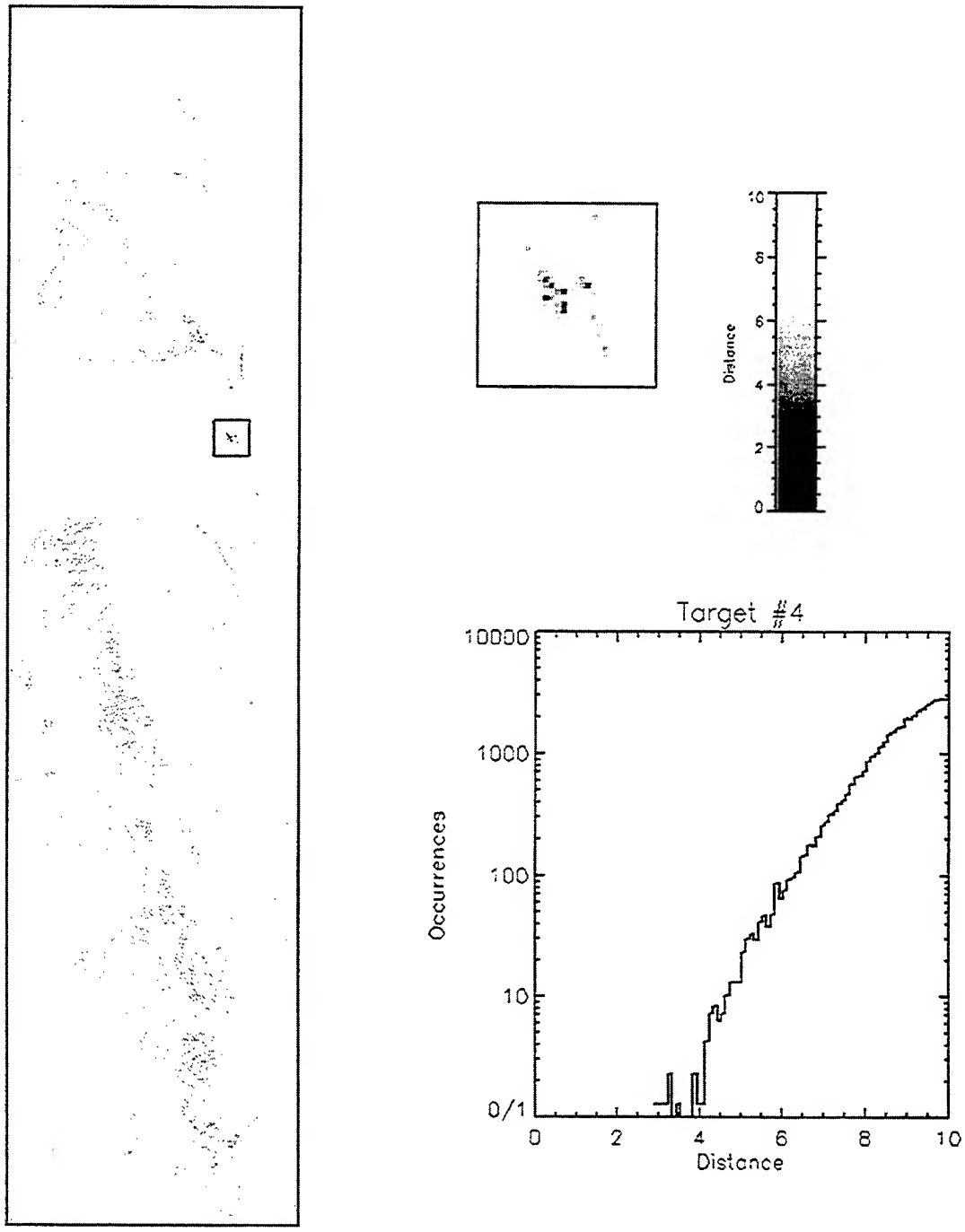

Fig. B.38 Mahalanobis Distance Rule Image for Target #4

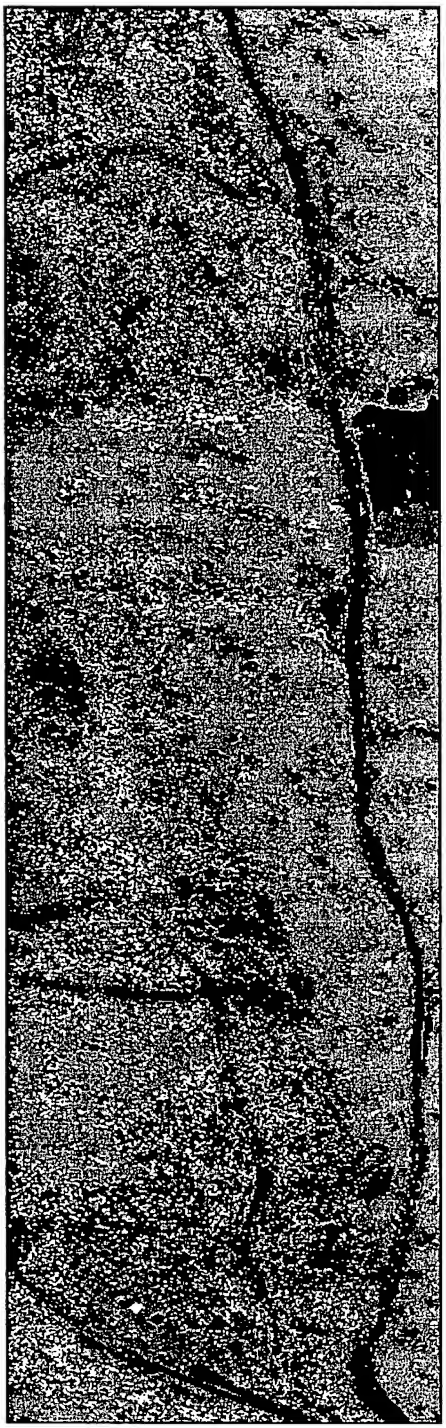

Full Image

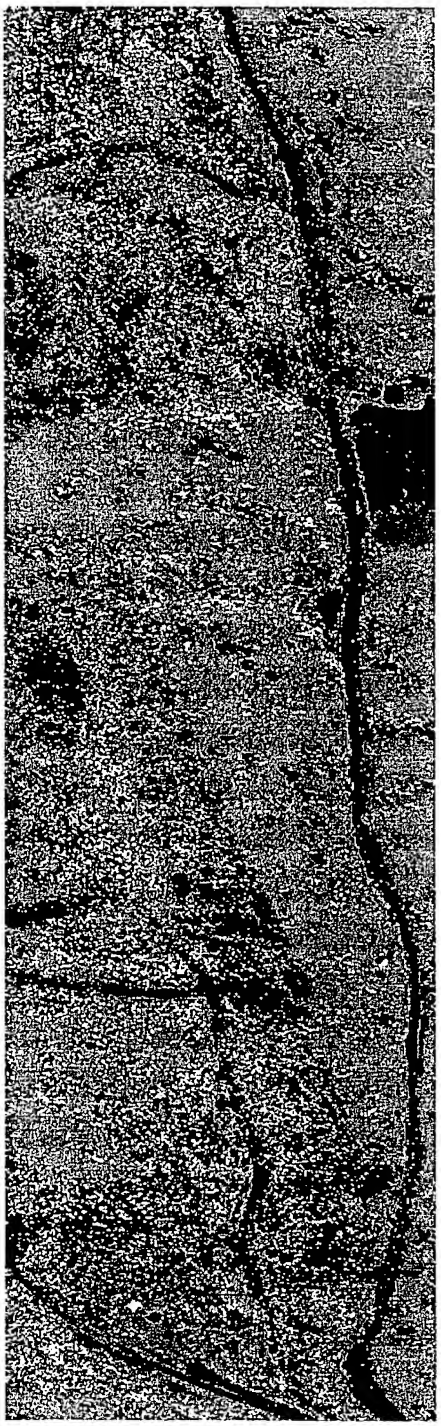

90%

Fig. B.39 Maximum Likelihood Mapping Output for Full Image and 90% Certainty

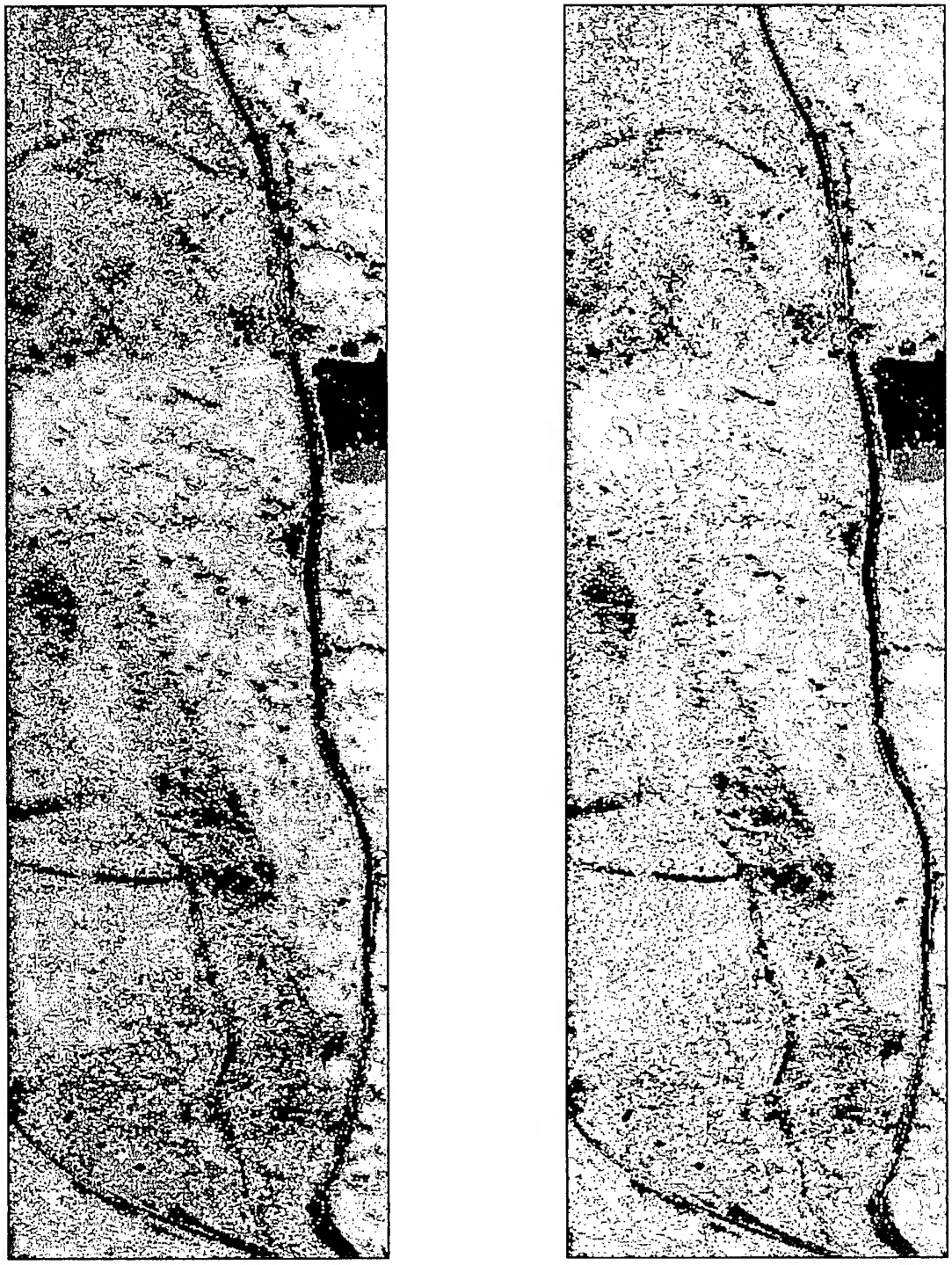

99% 99.99%

Fig. B.40 Maximum Likelihood Mapping Output for 99% and 99.99% Certainty

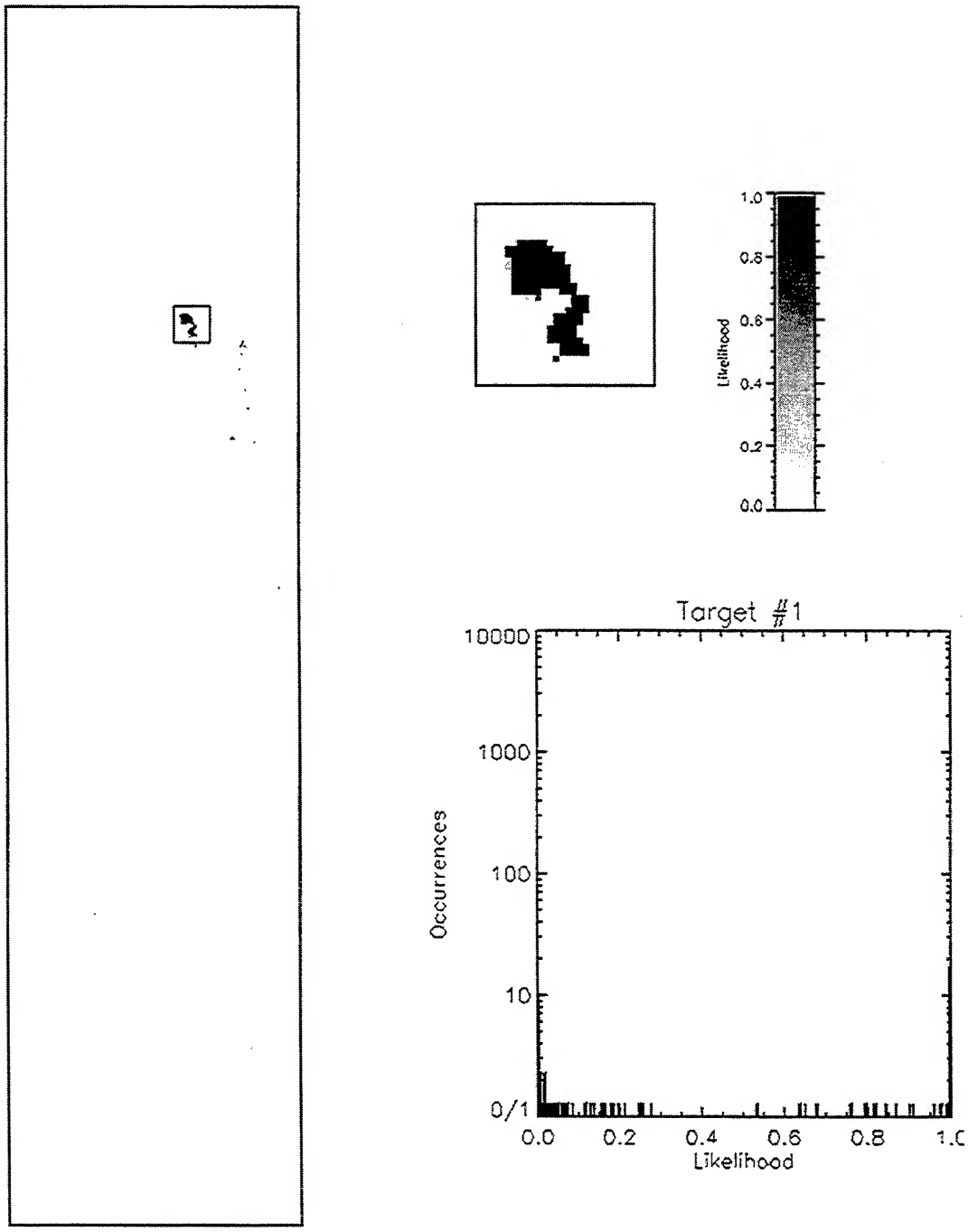

Fig. B.41 Maximum Likelihood Rule Image for Target #1

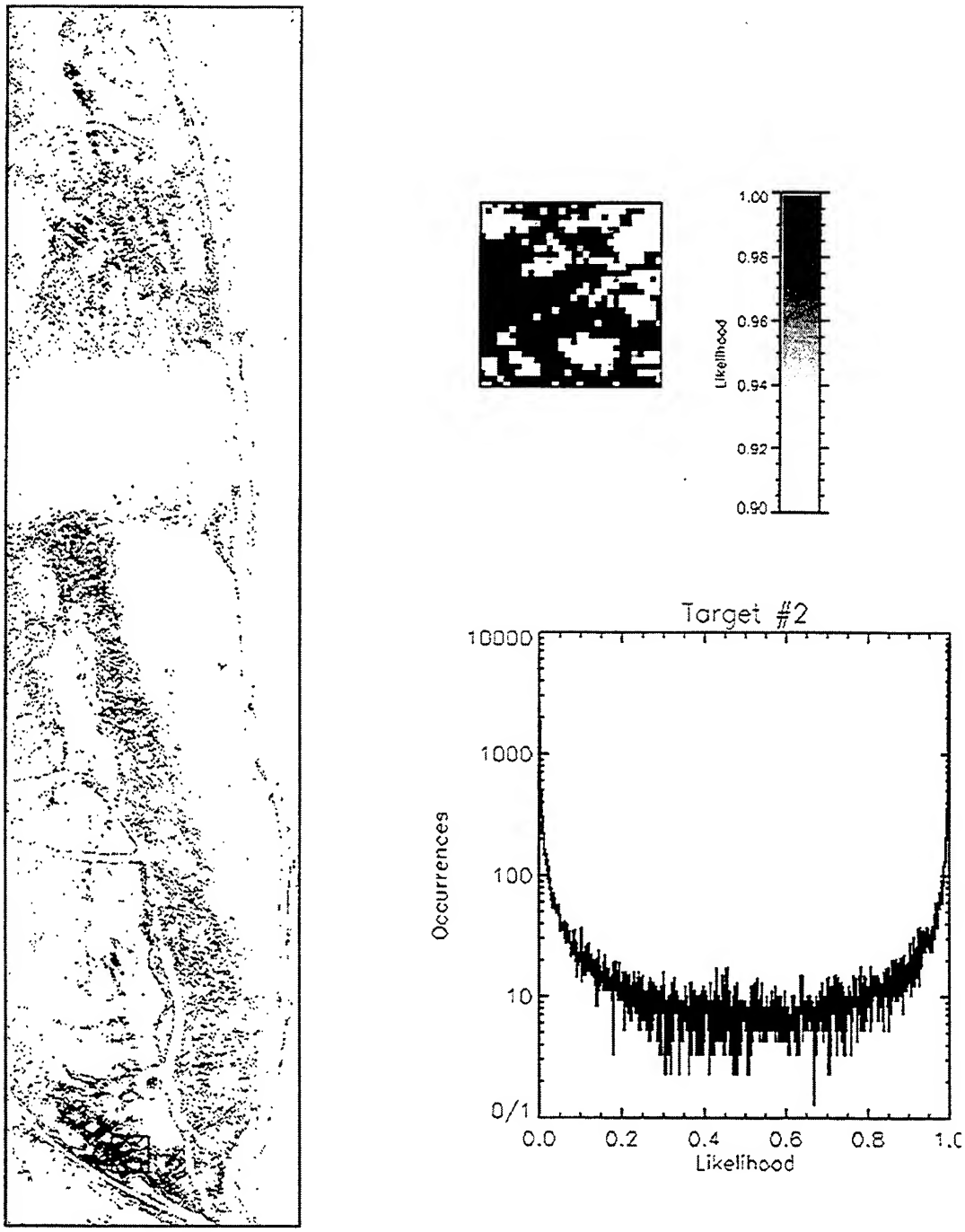

Fig. B.42 Maximum Likelihood Rule Image for Target #2

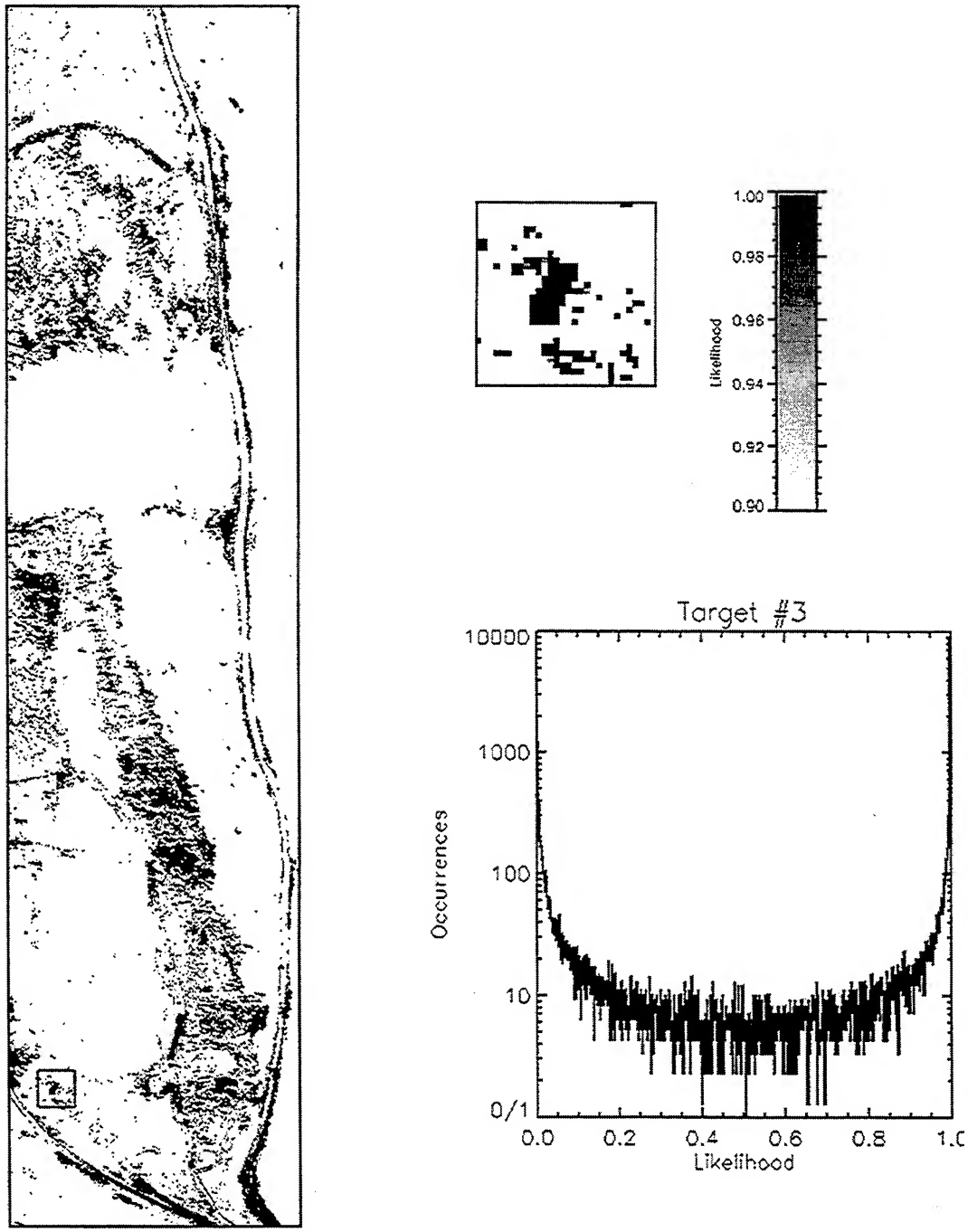

Fig. B.43 Maximum Likelihood Rule Image for Target #3

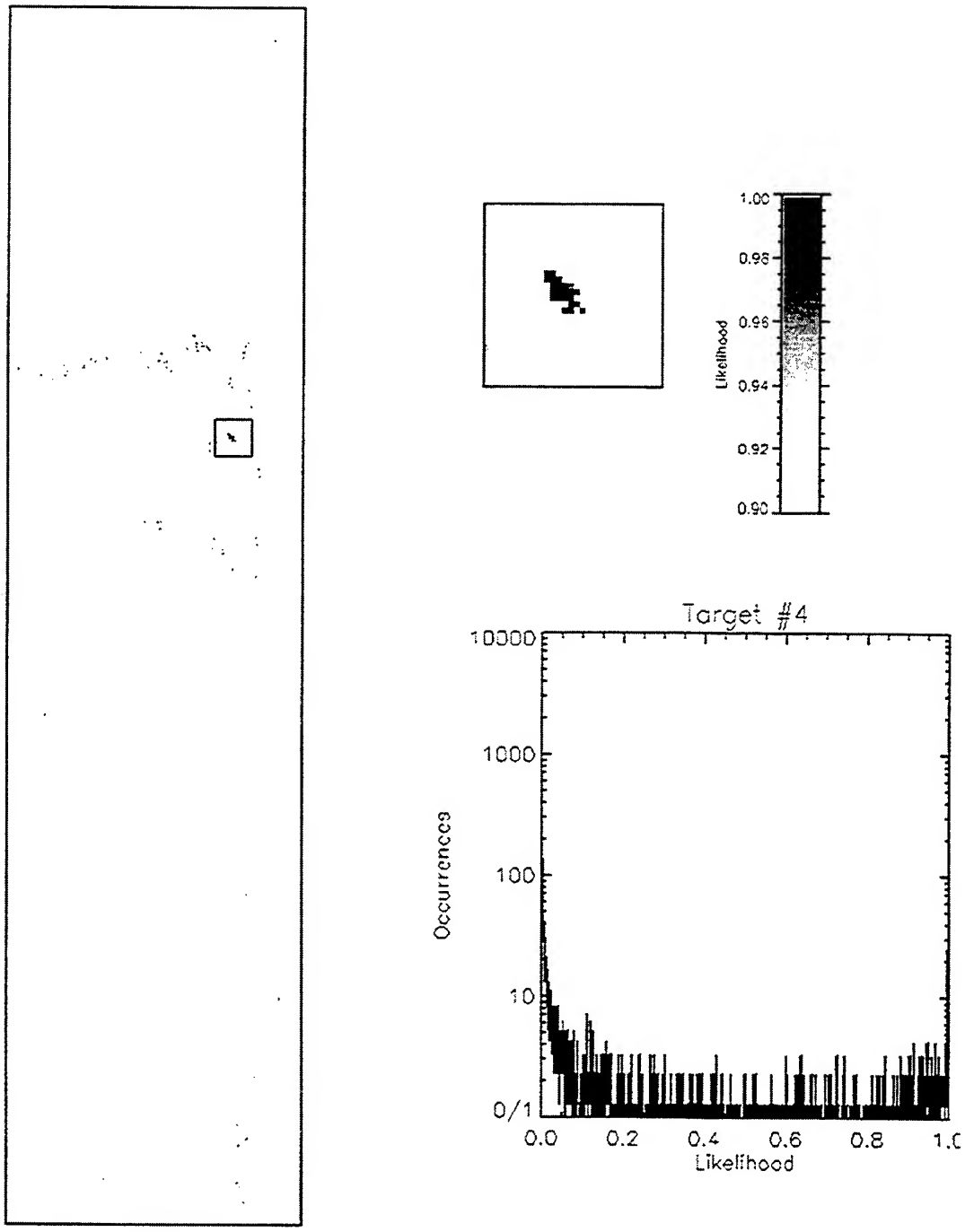

Fig. B.44 Maximum Likelihood Rule Image for Target #4

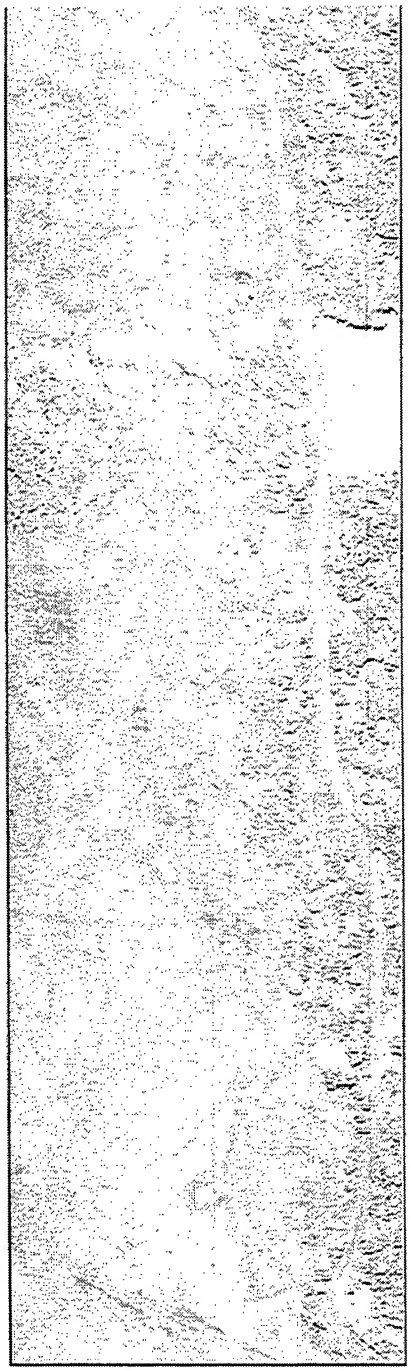

Fig. B.45 Linear Spectral Unmixing Error Output

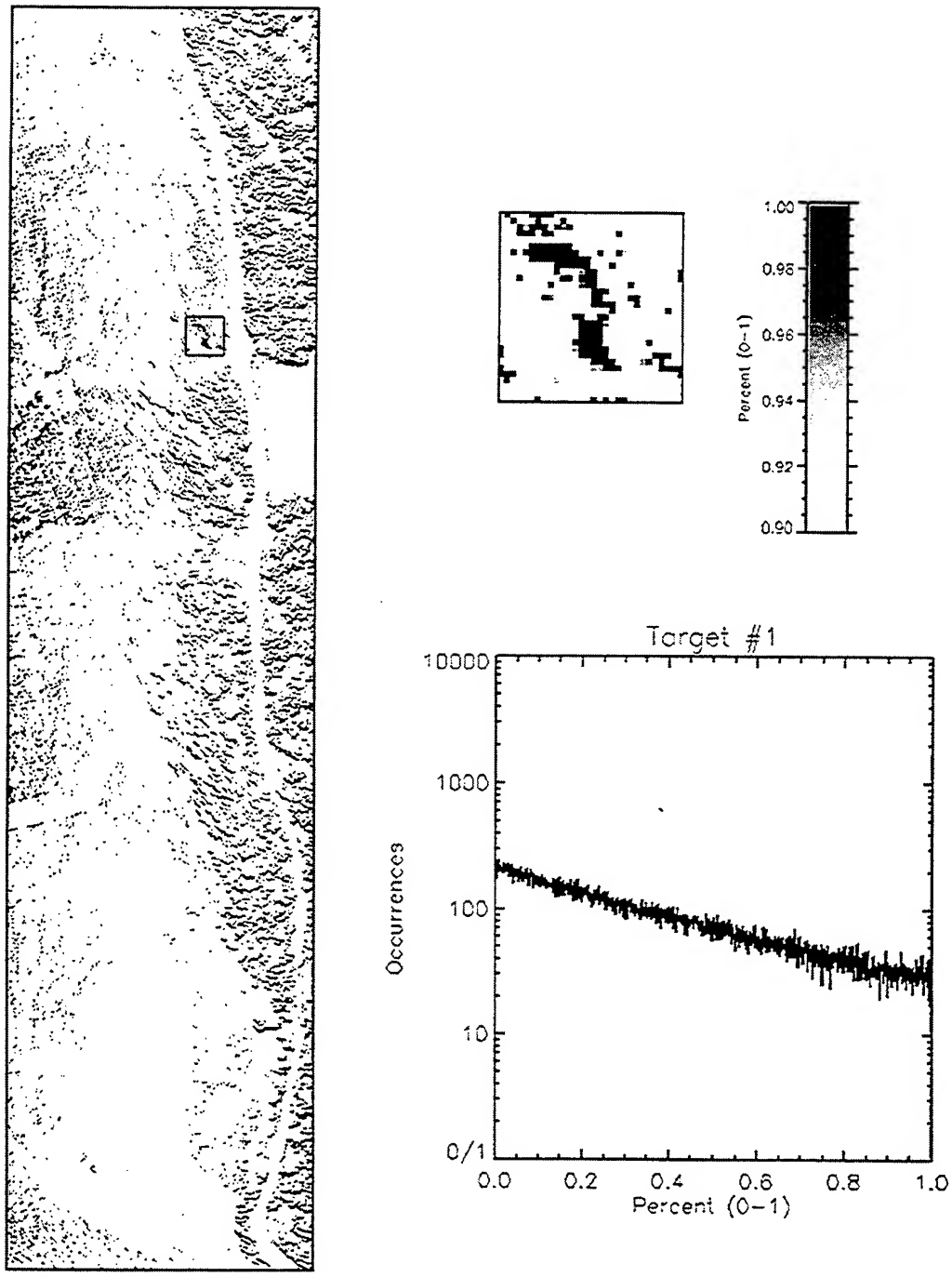

Fig. B.46 Linear Spectral Unmixing Rule Image for Target #1

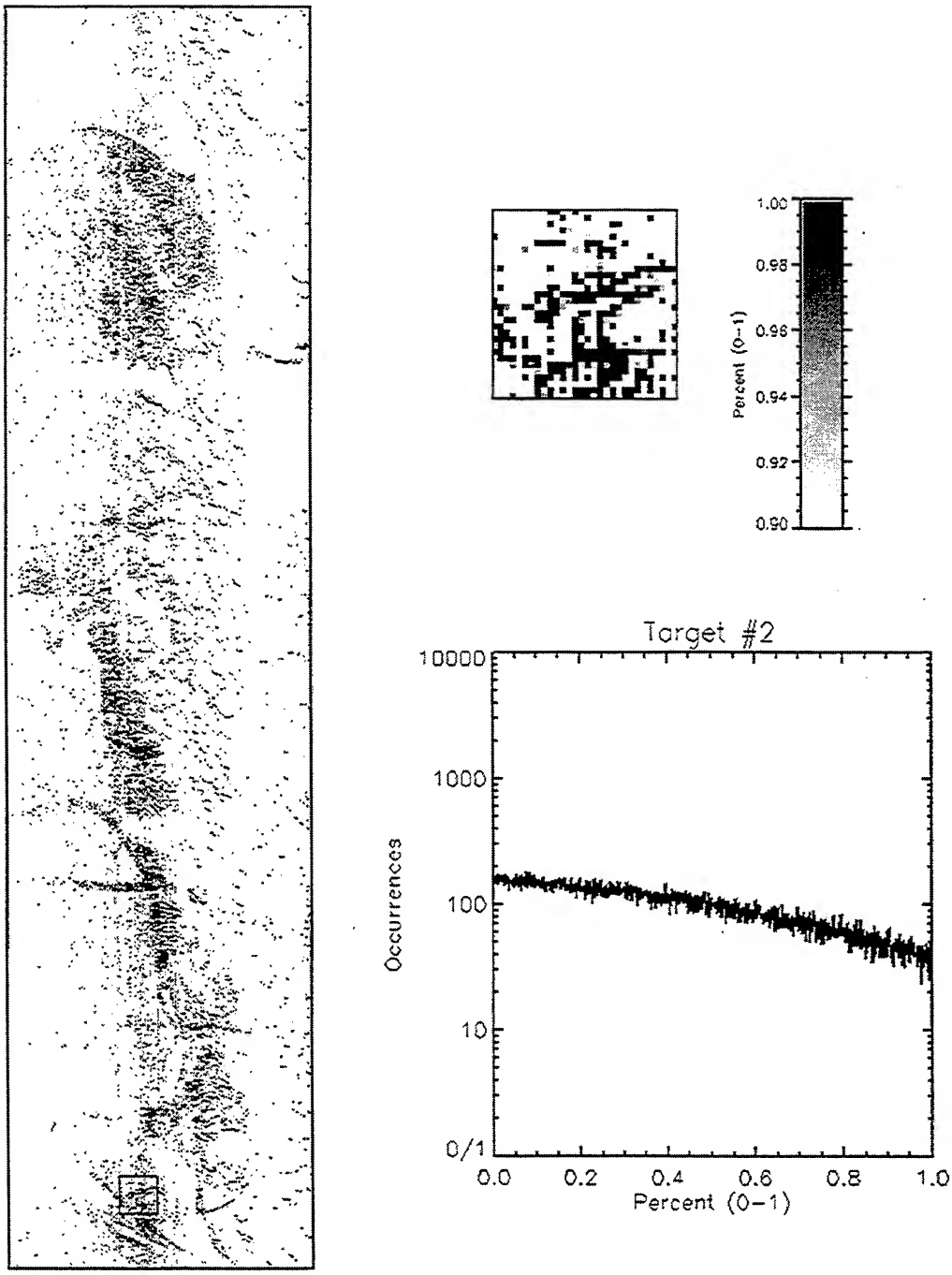

Fig. B.47 Linear Spectral Unmixing Rule Image for Target #2

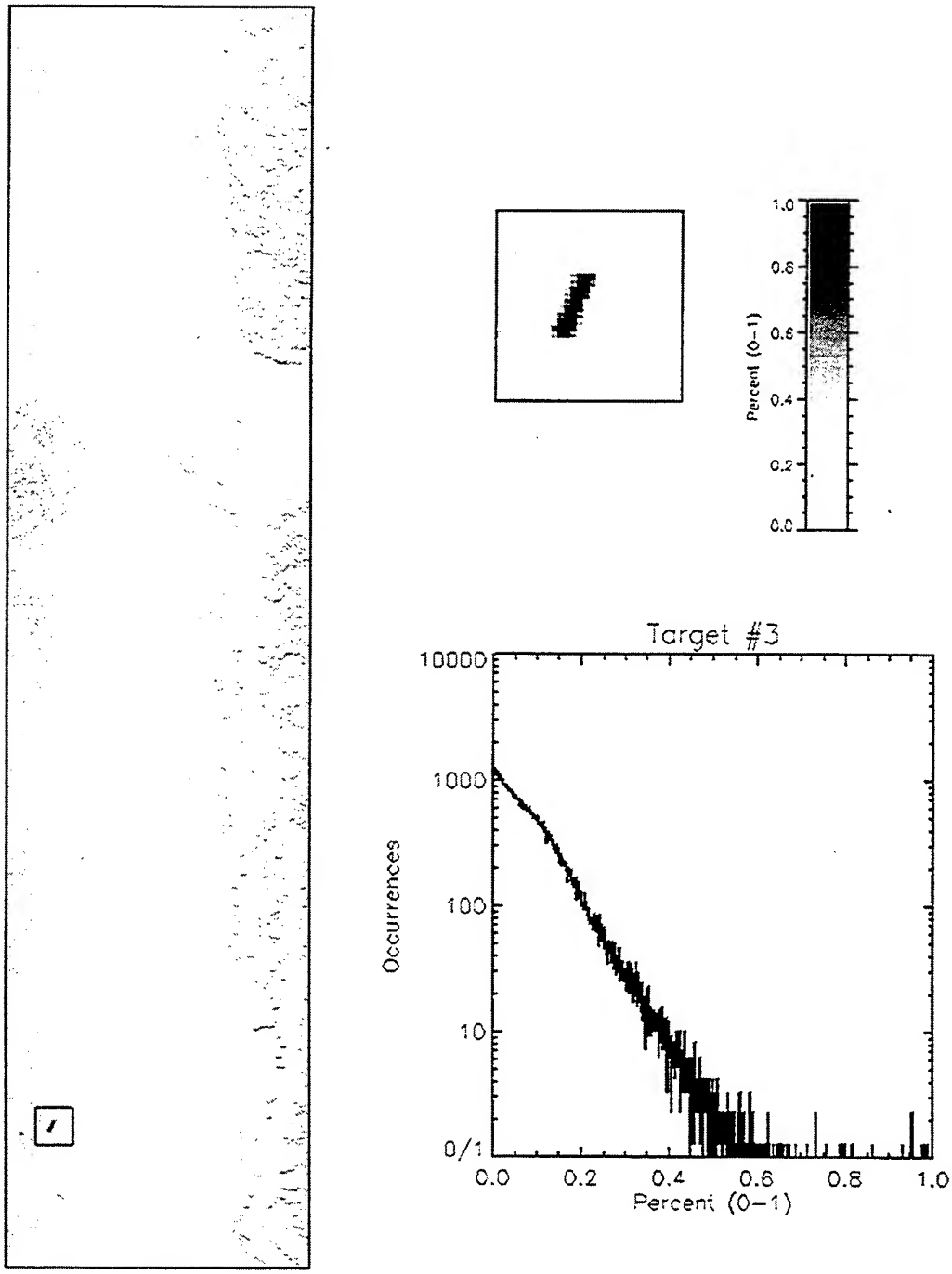

Fig. B.48 Linear Spectral Unmixing Rule Image for Target #3

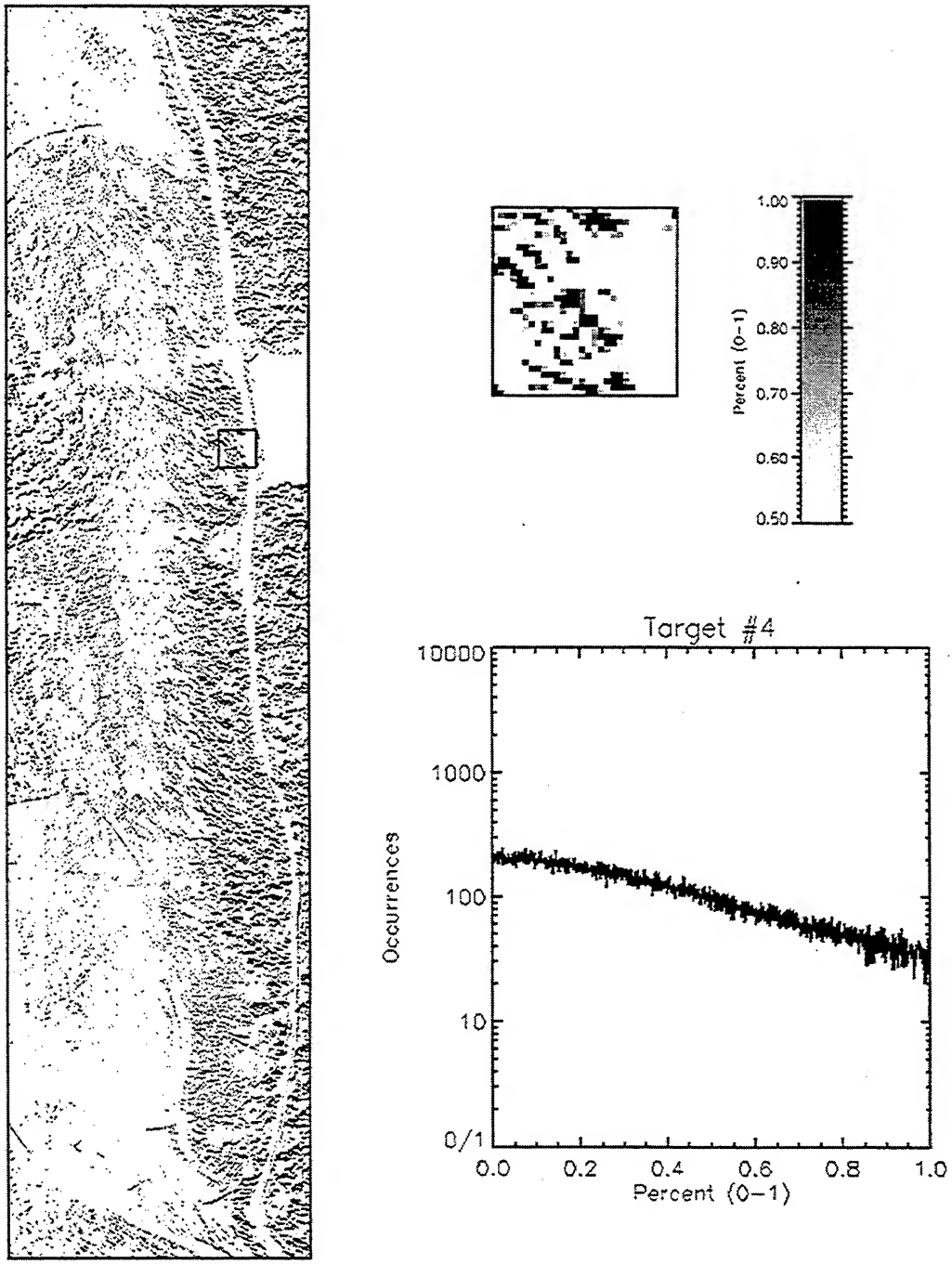

Fig. B.49 Linear Spectral Unmixing Rule Image for Target #4

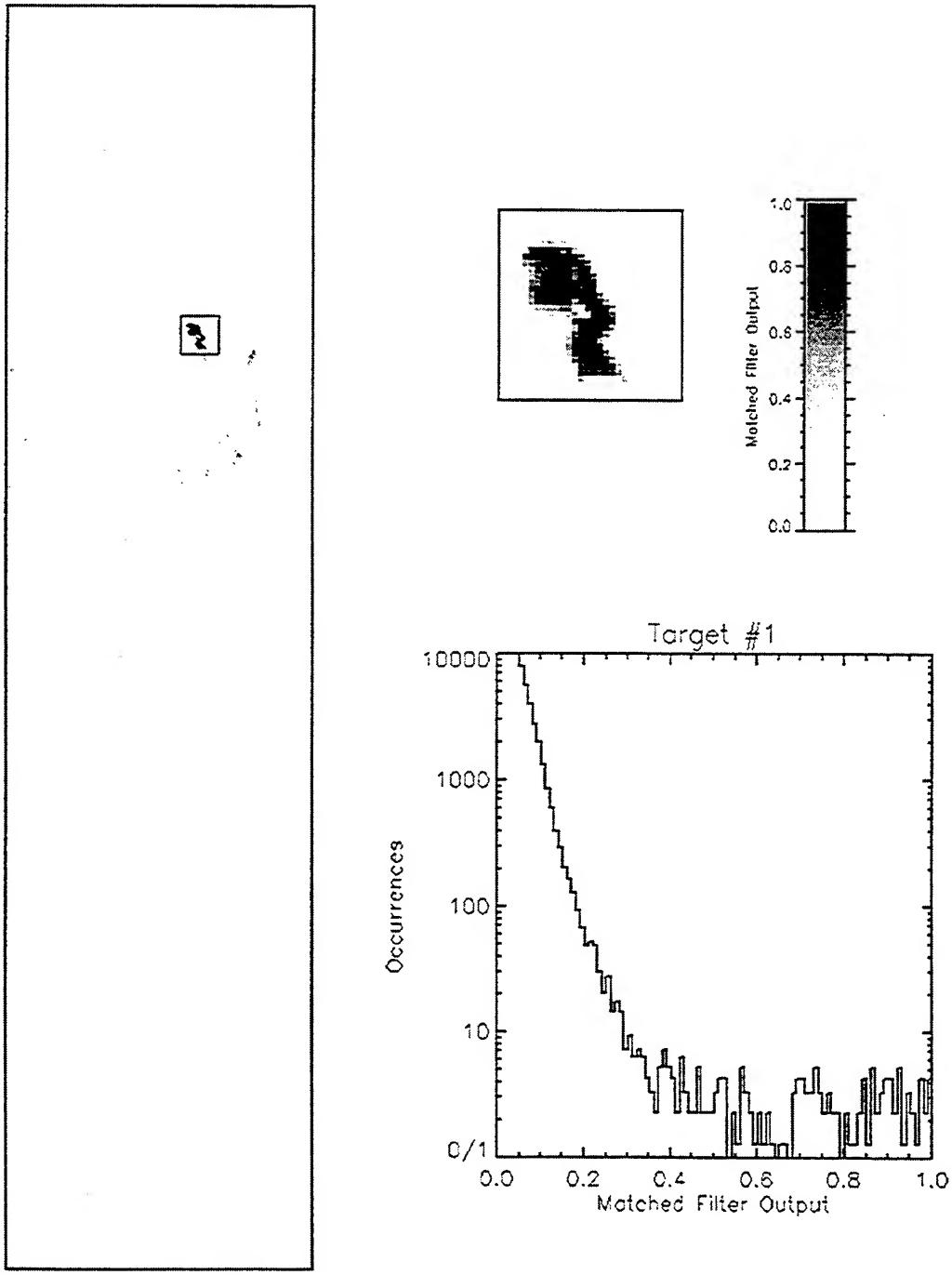

Fig. B.50 Matched Filter Rule Image for Target #1

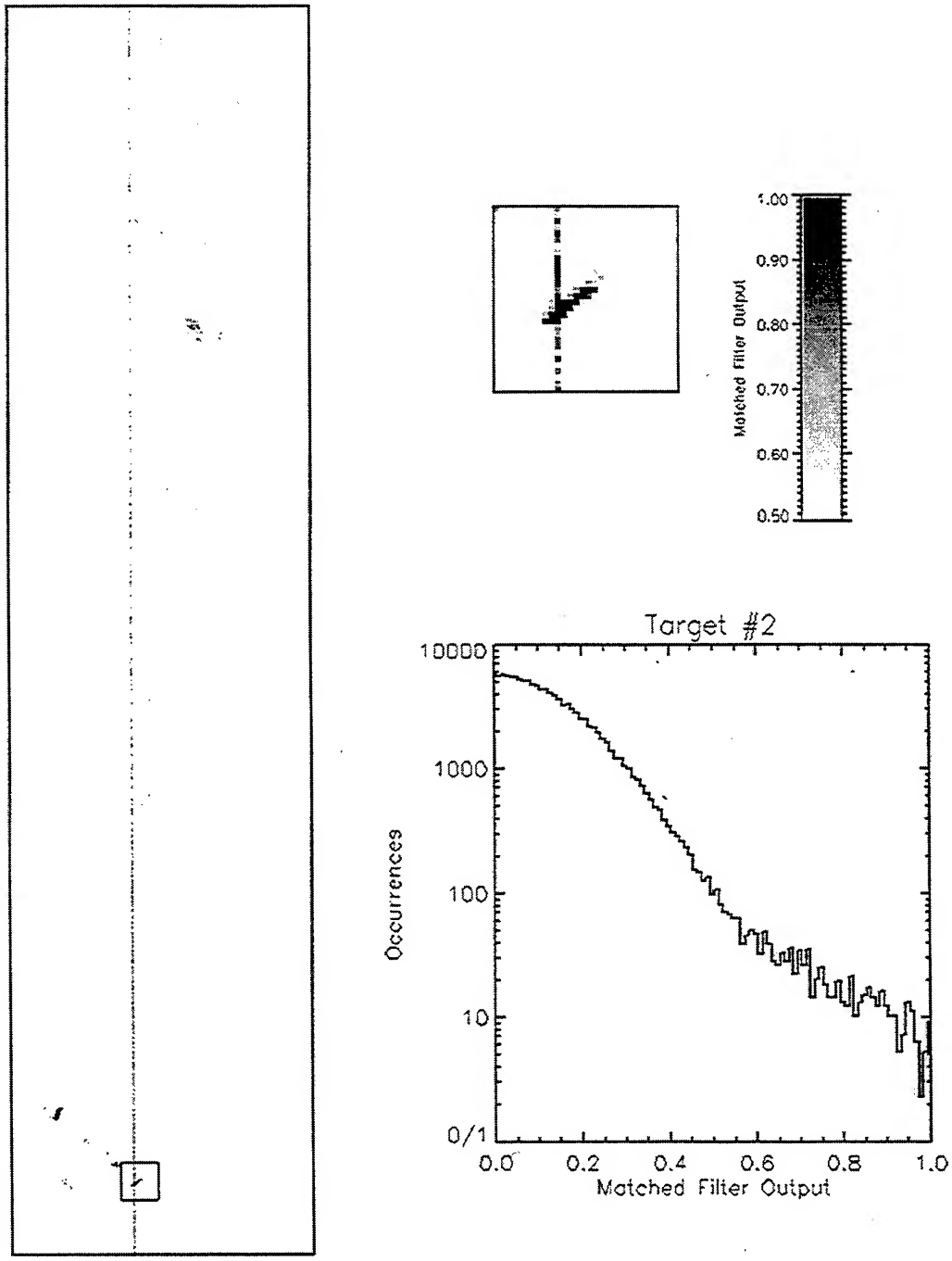

Fig. B.51 Matched Filter Rule Image for Target #2

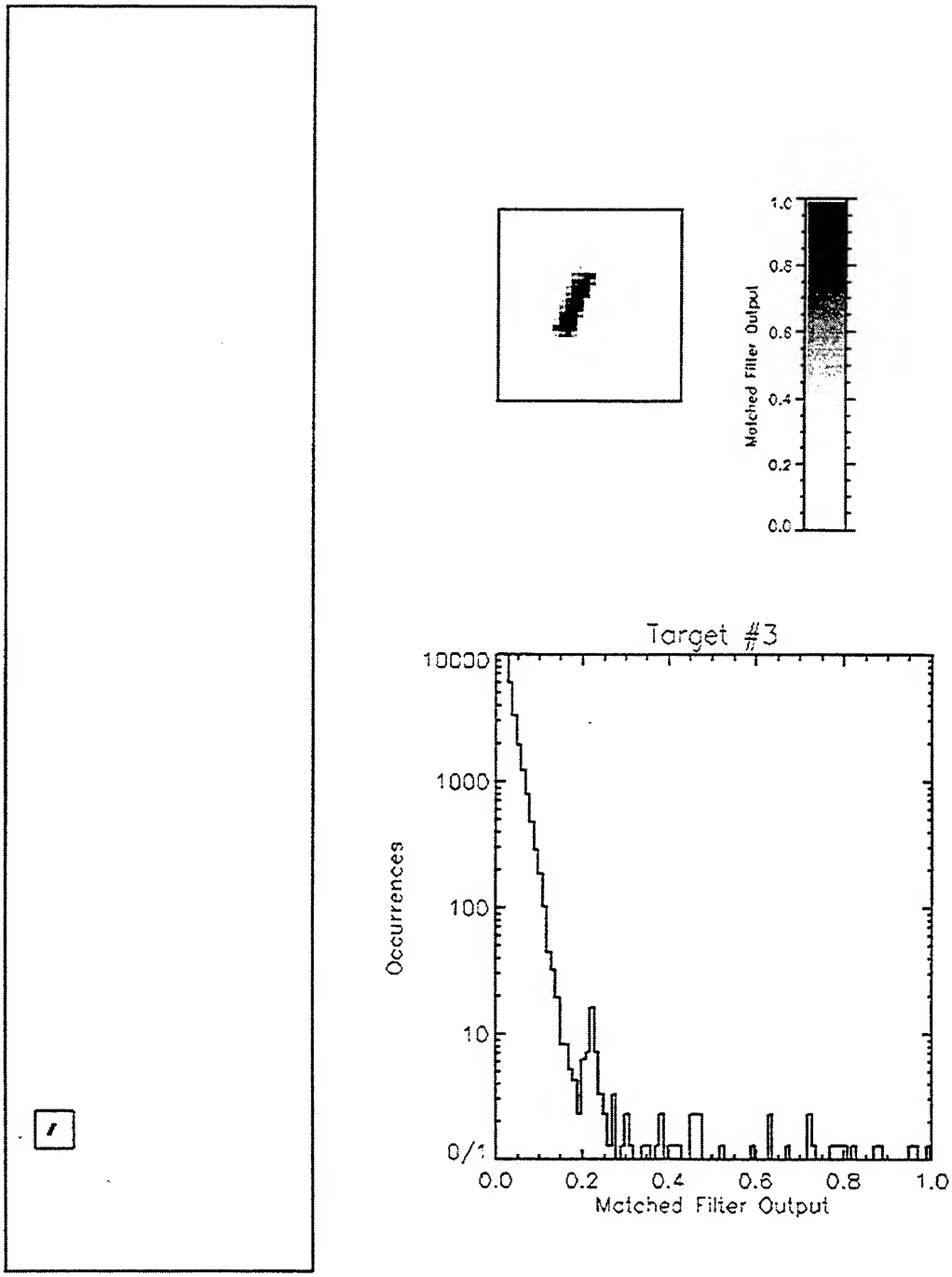

Fig. B.52 Matched Filter Rule Image for Target #3

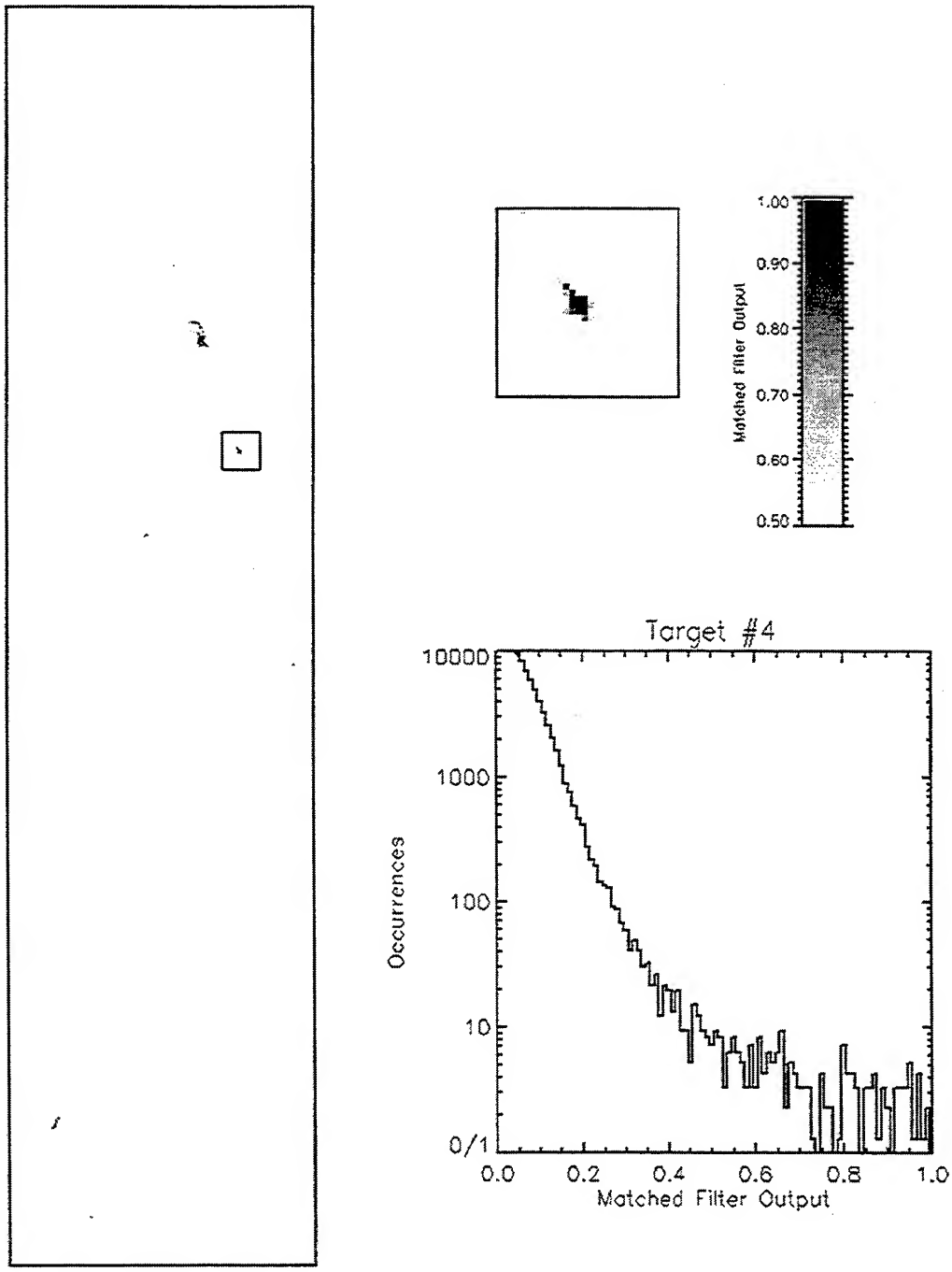

Fig. B.53 Matched Filter Rule Image for Target #4

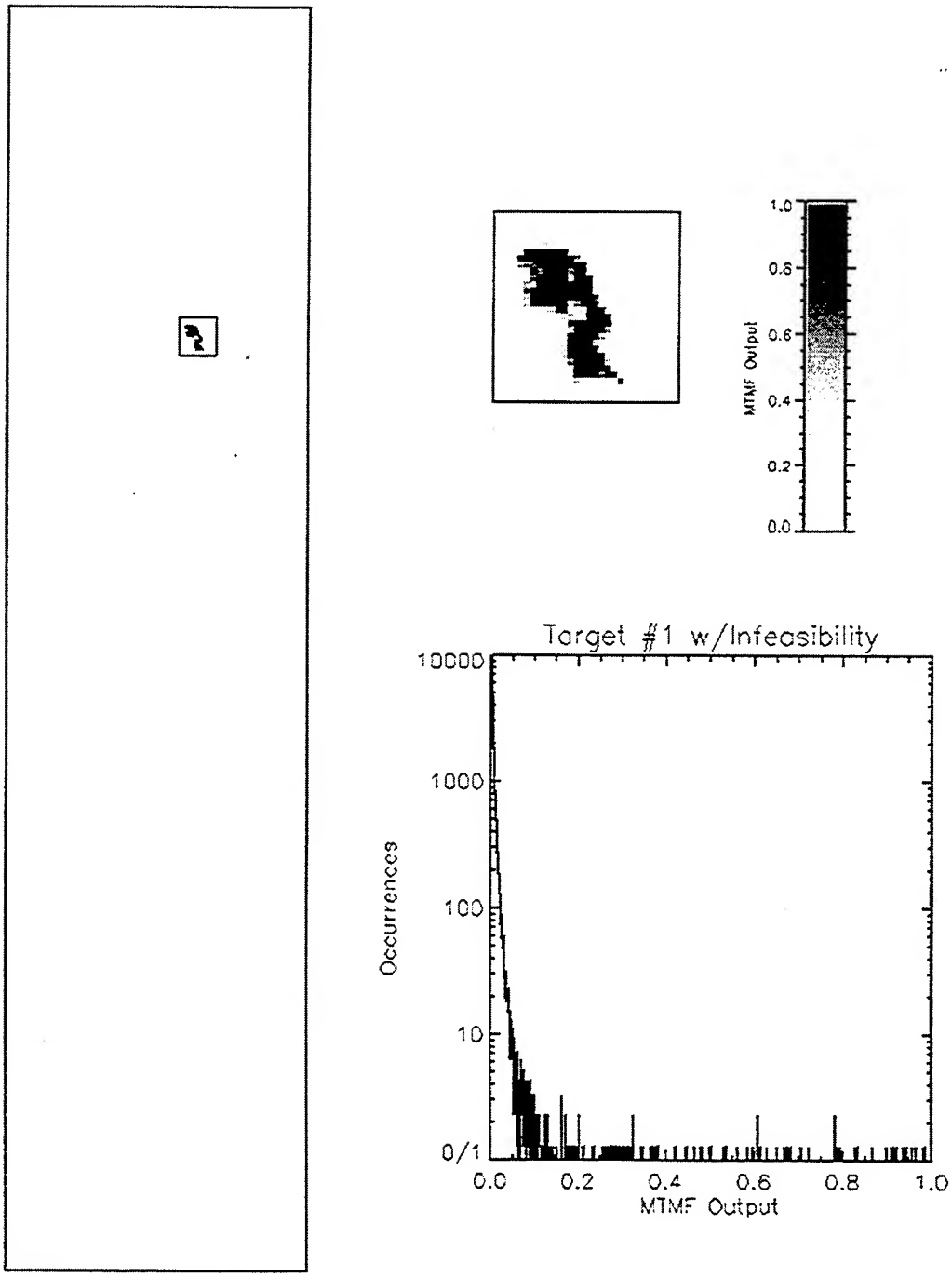

Fig. B.54 MTMF™ Rule Image for Target #1

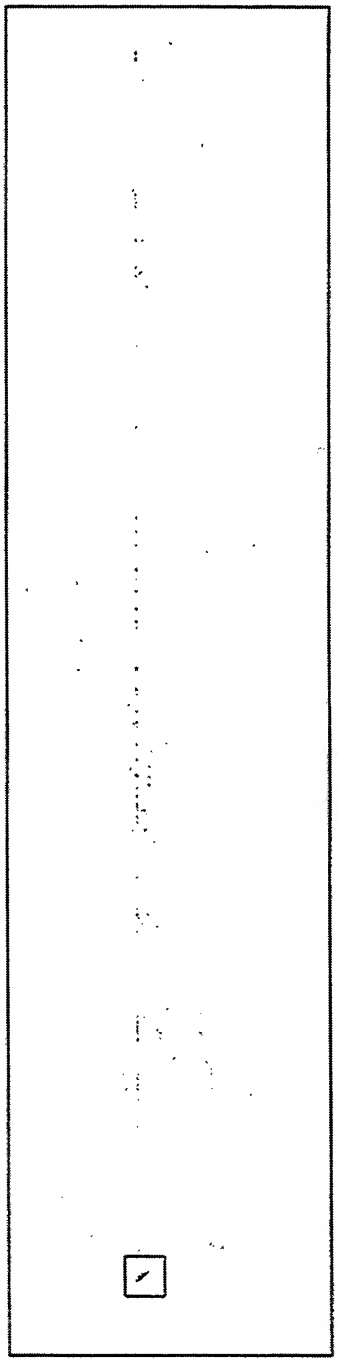

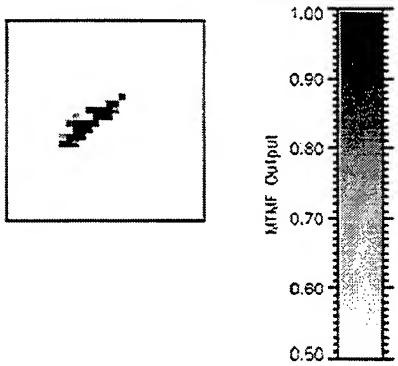

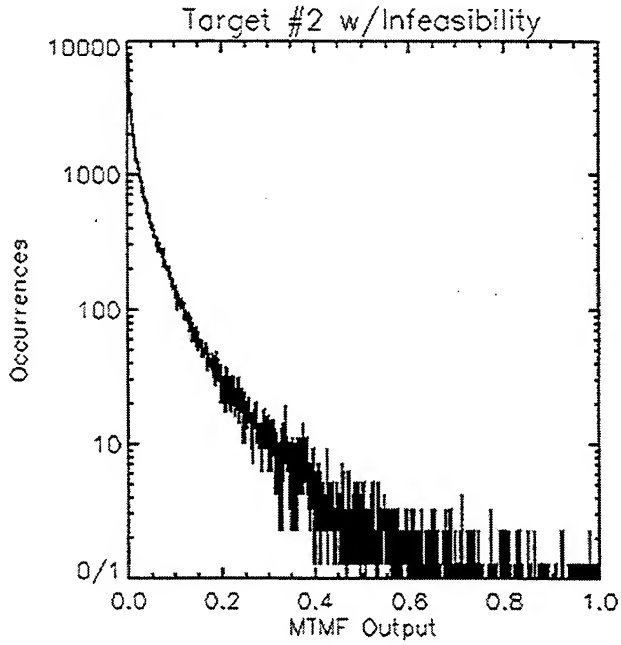

Fig. B.55 MTMF™ Rule Image for Target #2

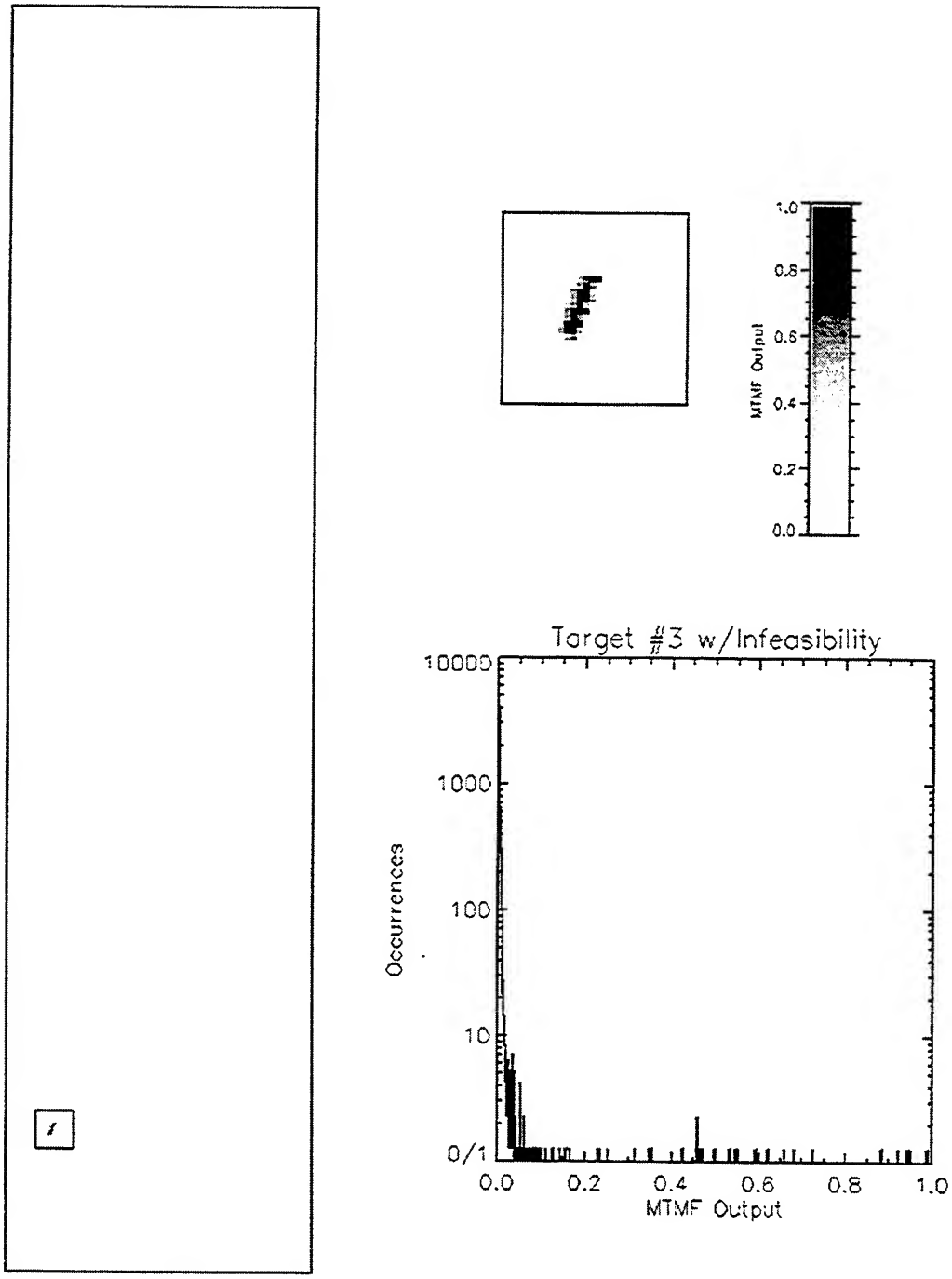

Fig. B.56 MTMF™ Rule Image for Target #3

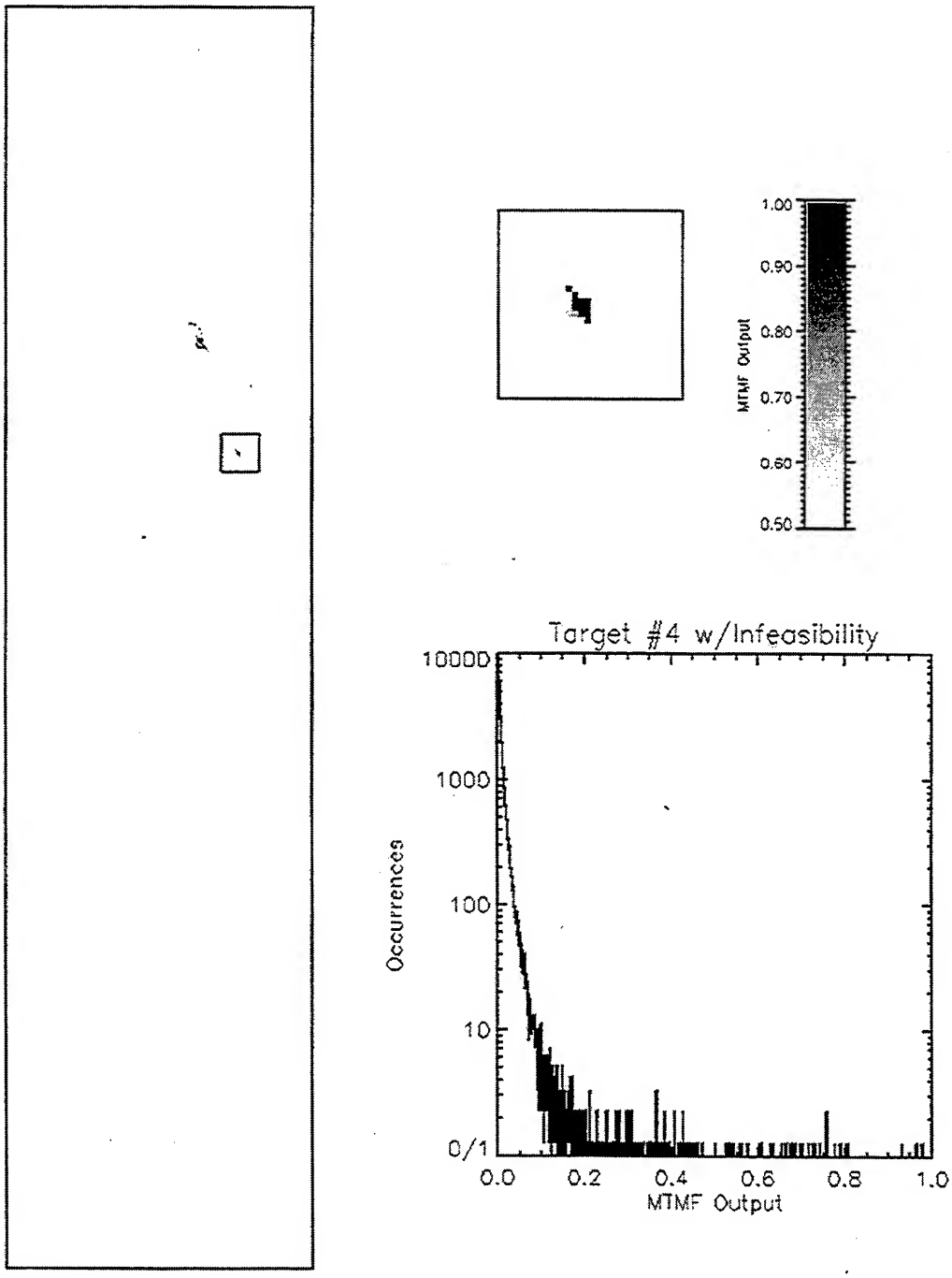

Fig. B.57 MTMF™ Rule Image for Target #4

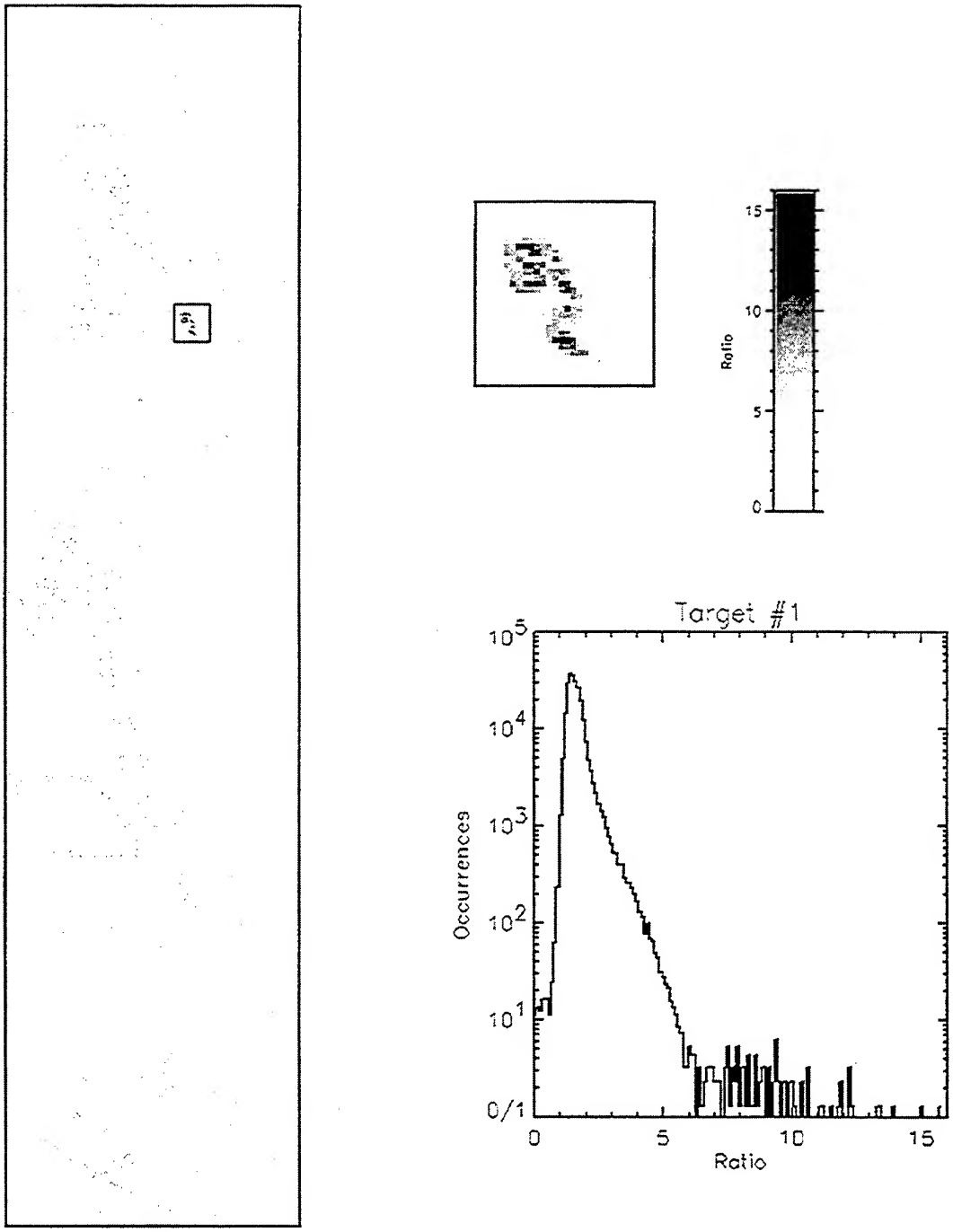

Fig. B.58 Spectral Feature Fitting Rule Image for Target #1

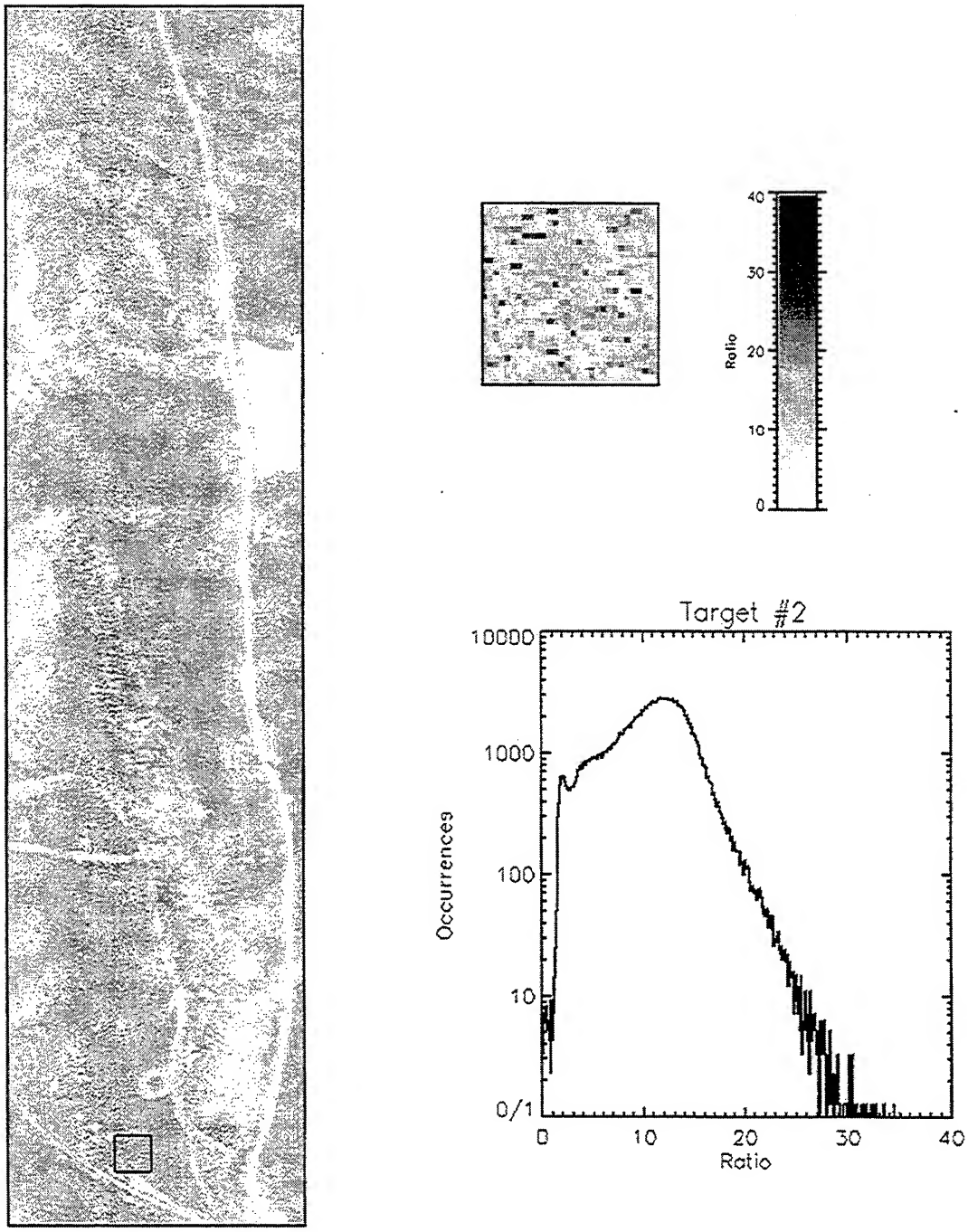

Fig. B.59 Spectral Feature Fitting Rule Image for Target #2

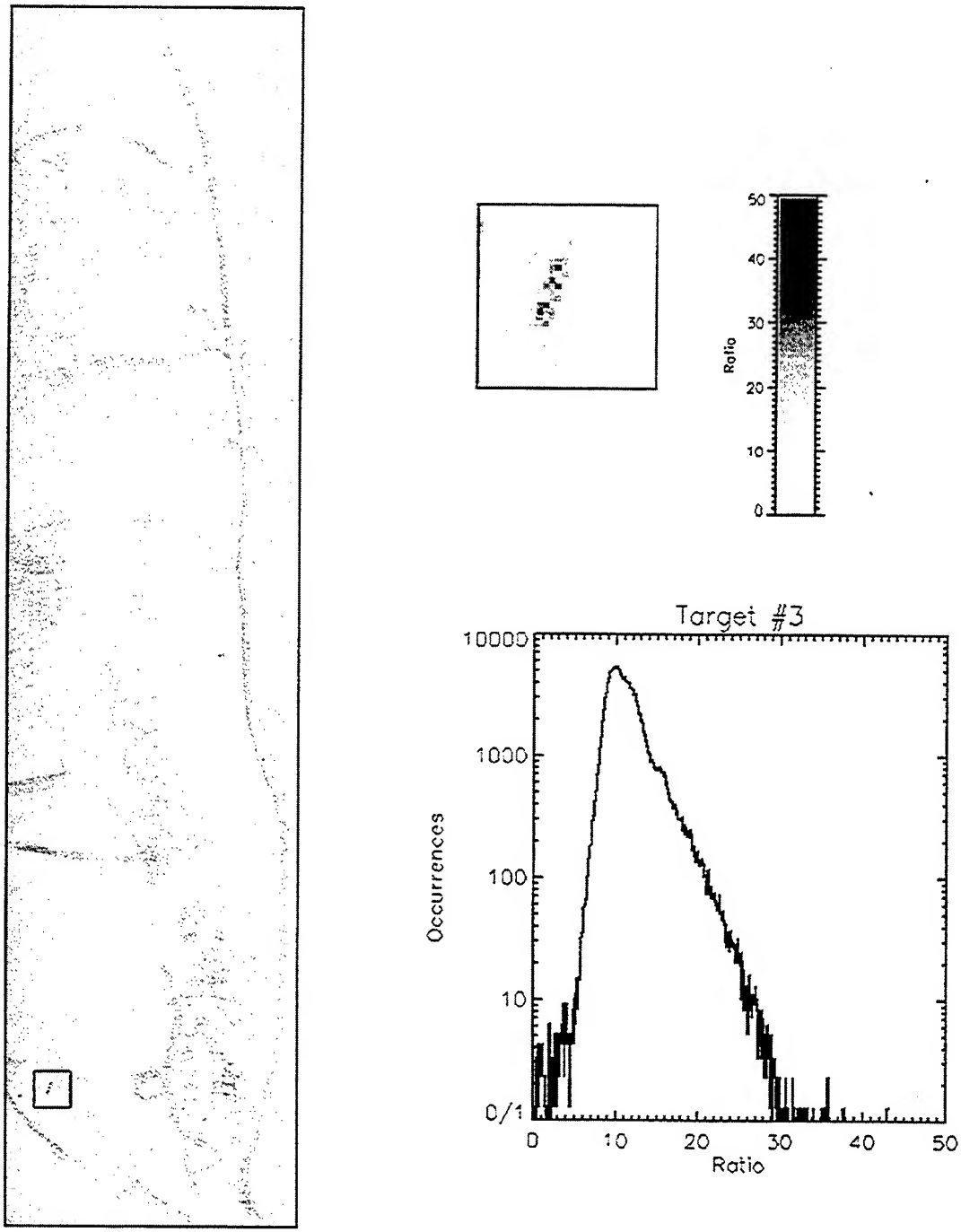

Fig. B.60 Spectral Feature Fitting Rule Image for Target #3

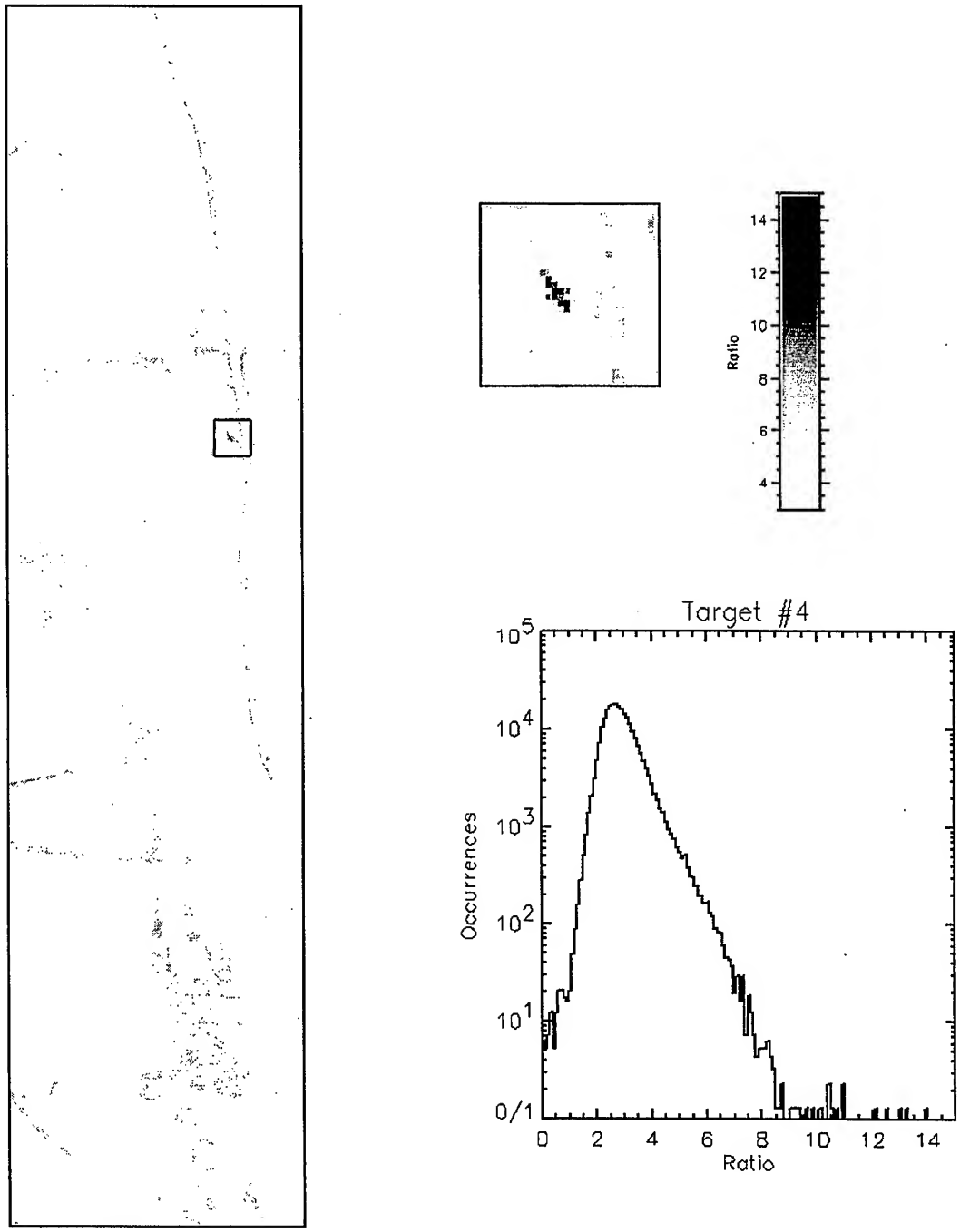

Fig. B.61 Spectral Feature Fitting Rule Image for Target #4

Fig. B.62 K Means Mapping Image for Five Endmembers

Fig. B.63 K Means Mapping Image for Ten Endmembers

Fig. B.64 K Means Mapping Image for Sixteen Endmembers

Fig. B.65 ISODATA Mapping Image for Five Endmembers

Fig. B.66 ISODATA Mapping Image for Ten Endmembers

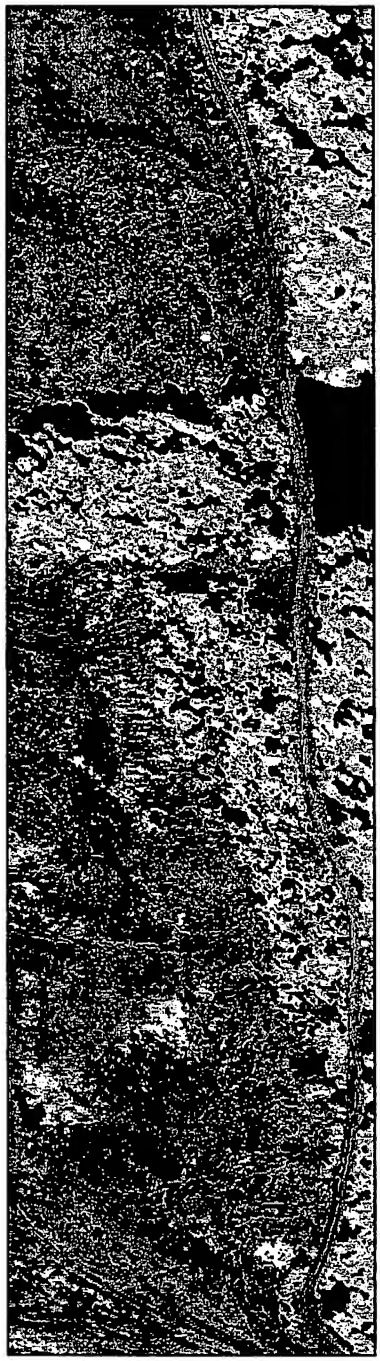

Fig. B.67 ISODATA Mapping Image for Sixteen Endmembers

THIS PAGE INTENTIONALLY LEFT BLANK

LIST OF REFERENCES

Asrar, Ghassem, Ed., Theory and Applications of Optical Remote Sensing, John Wiley and Sons, New York, 1989.

Atmosphere REMoval Program (ATREM) User's Guide, ver. 3.1, 1999.

Boardman, Joseph W., Geometric Mixture Analysis of Imaging Spectrometry Data, Center for the Study of earth from Space, Cooperative Institute for Research in Environmental Sciences, University of Colorado, 1994.

Boreman, Glenn D., Basic Electro-Optics for Electrical Engineers, SPIE Optical Engineering Press, Bellingham, Washington, 1998.

Campbell, James B., Introduction to Remote Sensing, Second Edition, The Guilford Press, New York, 1996.

Chai, Sek M., et al., Hyper-spectral Image Processing Applications on the SIMD Pixel Processor for the Digital Battlefield, *Computer Vision Beyond the Visible Spectrum: Methods and Applications, 1999, Proceedings. IEEE Workshop on*, pp.130-138, 1999.

Crowley, J.K., and Clark, R.N., AVIRIS study of Death Valley Evaporite Deposits Using Least-squares Band-fitting Methods, *Summaries of the Third Annual JPL Airborne Geoscience Workshop*, JPL Publication 92-14, v.1, pp.29-31, 1992.

Devore, Jay L., Probability and Statistics for Engineering and the Sciences, Fourth Edition, Duxbury Press, Pacific Grove, 1995.

Elachi, Charles, Introduction to the Physics and Techniques of Remote Sensing, John Wiley and Sons, New York, 1987.

Folkman, Mark A., DeLong, Raymond K., et al., TRWIS III: An Aircraft-Based Hyperspectral Imager, TRW Space & Electronics Group, March 1996.

Folkman, Mark A., Gleichauf, Darrell, et al., Performance Characterization and Calibration of the TRWIS III Hyperspectral Imager, TRW Space & Electronics Group, 1996.

Folkman, Mark A., Sandor, Stephanie, et al., Updated Results from Performance Characterization and Calibration of the TRWIS III Hyperspectral Imager, TRW Space & Electronics Group, 1997.

Harsanyi, Joseph C., and Chang, Chein-I, Hyperspectral Image Classification and Dimensionality Reduction: An Orthogonal Subspace Projection Approach, *IEEE Transactions on Geoscience and Remote Sensing,* v.32, no.4, 1994.

Hung, Chih-Cheng, and Kim, The Application of Agglomerative Clustering In Image Classification Systems, *Southeastcon '92, Proceedings, IEEE*, vol.1, pp.23-26, 1992

Kneizys, F.X., et al., Atmospheric Transmittance/Radiance: Computer Code LOWTRAN 6, Air Force Geophysics Laboratory, Hanscom Air Force Base, Massachusetts, 1983.

Kruse, F.A., et al., The Spectral Image Processing System (SIPS)—Interactive Visualization and Analysis of Imaging Spectrometer Data, *Remote Sensing of Environment,* v.44, pp.145-163, 1993.

Kruse, F.A., Taranik, Dan L., Mapping Hydrothermically Altered Rocks With the Airborne Imaging Spectrometer (AIS) and the Airborne Visible/Infrared Imaging Spectrometer, *Geoscience and Remote Sensing Symposium, 1989, 12th Canadian Symposium on Remote Sensing,* pp.952-956, 1989.

Lillesand, Thomas M., and Kiefer, Ralph W., Remote Sensing and Image Interpretation, Third Edition, John Wiley and Sons, New York, 1994.

Mazer, Alan S., et al., Image Processing Software for Imaging Spectrometry Data Analysis, *Remote Sensing of Environment,* v.24, pp.201-210, 1988.

MASINT HYPERSPECTRAL STUDY: *Interim Progress Report*, Office of Research and Development, 1995.

Mather, Paul M., Computer Processing of Remotely-Sensed Images: An Introduction, Second Edition, John Wiley and Sons, Chichester, 1999.

Multispectral Users Guide, Department of Defense, August 1995.

Richards, J. A., and Jia, Xiuping, Remote Sensing Digital Imagery Analysis: An Introduction, Third Edition, Springer-Verlag, Germany, 1999.

Sabins, Floyd F., Remote Sensing: Principles and Interpretation, W.H. Freeman and Company, San Francisco, California, 1978.

Simi, Christopher, et al., Night Vision Imaging Spectrometer (NVIS) Performance

Parameters and their impact on Various Detection Algorithms, 2000.

Slater, Phillip N., Remote Sensing: Optics and Optical Systems, Addison-Wesly Publishing Company, Reading, Massachusetts, 1980.

Tou, J.T., Gonzalez, R.C., Pattern Recognition Principles, Addison-Wesley Publishing Company, Reading Massachusetts, 1974.

THIS PAGE INTENTIONALLY LEFT BLANK

INITIAL DISTRIBUTION LIST

1. Defense Technical Information Center 2
   8725 John J. Kingman Road, Suite 0944
   Ft. Belvoir, VA 22060-6218

2. Dudley Knox Library 2
   Naval Postgraduate School
   411 Dyer Road
   Monterey, CA 93943-5101

3. Richard C. Olsen, Code PH/OS 10
   Department of Physics
   Naval Postgraduate School
   Monterey, CA 93943-5002

4. Chairman, Code SP 1
   Space Systems Academic Group
   Naval Postgraduate School
   Monterey, CA 93943-5002

5. Chris Simi 2
   US Army CECOM
   Night Vision and Electronic Sensors Directorate
   AMSEL-RD-NV-RPFS (Attn: C. Simi)
   10221 Burbeck Rd, Suite 430
   Ft. Belvoir, VA 22060

6. LT David R. Perry, USN 2
   211 County Rd. 492
   Carthage, TX 75633

7. MAJ E. R. Amman, USMC (ret.) 1
   6034 Cozzens St.
   San Diego, CA 92122

8. LCDR J. M. Perry Jr., USN (ret.) 1
   211 County Rd. 492
   Carthage, TX 75633

9. Diane Johnson 1
HQ/SWC/AET
730 Irwin Ave.
Suite 83
Schriver AFB, CO 80912-7383